NASA CR-159889
R78AEG612

National Aeronautics and
Space Administration

TF34 ENGINE COMPRESSION SYSTEM COMPUTER STUDY

by

W.M. Hosny
W.G. Steenken

GENERAL ELECTRIC COMPANY

(NASA-CR-159889) TF34 ENGINE COMPRESSION SYSTEM COMPUTER STUDY (General Electric Co.) 93 p HC A05/MF A01 CSCL 21E

N81-15005

Unclas
G3/07 29715

Prepared For

National Aeronautics and Space Administration

NASA Lewis Research Center
CONTRACT NAS3-20599

1 Report No NASA CR-159889	2. Government Accession No.	3. Recipient's Catalog No
4 Title and Subtitle TF34 ENGINE COMPRESSION SYSTEM COMPUTER STUDY		5. Report Date June, 1979 6 Performing Organization Code
7 Author(s) W. M. Hosny W. G. Steenken		8. Performing Organization Report No R78 AEG 612 10. Work Unit No
9 Performing Organization Name and Address General Electric Company Aircraft Engine Group Cincinnati, Ohio 45215		11. Contract or Grant No. NAS3-20599 13. Type of Report and Period Covered Contractor Report
12. Sponsoring Agency Name and Address National Aeronautics and Space Administration Washington, D.C. 20546		14. Sponsoring Agency Code

15 Supplementary Notes

Project Monitors: P.G. Batterton and E. J. Graber, Jr.
NASA-Lewis Research Center
Cleveland, Ohio 44135

16 Abstract

The objective of this program was to conduct a computer study of the stability of the TF34 compression system. The study was performed in two parts. During the first part, the stability of the fan and the compressor components was examined individually using linearized and time-dependent, one-dimensional stability analysis techniques. In the second part, the stability of the fan-core integrated compression system was investigated using a two-dimensional compression system model developed as part of this effort. The analytical equations on which this model was based satisfied the mass, axial momentum, radial momentum, and energy conservation equations for flow through a finite control volume.

The results of the present investigation gave an accurate simulation of the flow through the compression system. The speed lines of the components were reproduced; the points of instability were accurately predicted; the locations where the instability was initiated in the fan and the core were indicated; and the variation of the bypass ratio during flow throttling was calculated. The validity of the analytical techniques was then established by comparing these results with test data and with results obtained from the steady-state cycle deck.

17 Key Words (Suggested by Author(s)) Turbofan Compression System Stability Aerodynamic Stability Analytical Simulation Technique Fan Flow Radial Redistribution	18. Distribution Statement		
19 Security Class. (of this report) Unclassified	20. Security Classif. (of this page) Unclassified	21 No. of Pages	22 Price*

* For sale by the National Technical Information Service, Springfield Virginia 22161

FOREWORD

The program described in this report was conducted by the Aircraft Engine Group of the General Electric Company, Cincinnati, Ohio for the NASA Lewis Research Center, National Aeronautics and Space Administration under contract NAS3-20599.

The program was carried out under the technical cognizance of Mr. P. G. Batterton and Mr. E. J. Graber, Jr. of the NASA Lewis Research Center Turbine Engine Branch.

The contract effort was conducted at the Evendale Plant of the Aircraft Engine Group, Cincinnati, Ohio under the technical direction of Dr. W. G. Steenken with Dr. W. M. Hosny and Mr. W A. Tesch, formerly of General Electric, being the prime technical contributors. Support was provided by Mr. R. H. Moszee of the Evendale Plant in running some of the computer simulations, Mr. J. Isbell of the Lynn Plant in determining the compressor stage characteristics, Mr. D. Brahm of the Lynn Plant in providing cycle information for the dual spool cases, Mrs. L. Radcliffe, Miss J. Mullikin, and Mrs. J. Brooke of the Evendale Plant in preparing this manuscript.

TABLE OF CONTENTS

LIST OF ILLUSTRATIONS

LIST OF ILLUSTRATIONS (Continued)

LIST OF ILLUSTRATIONS (Concluded)

NOMENCLATURE

A	-	Area
C	-	Absolute Velocity
C_r	-	Radial Velocity
C_u	-	Absolute Tangential Velocity
C_z	-	Axial Velocity
F_z	-	Axial Blade Force
g_o	-	Gravitational Constant
L	-	Volume Length
N	-	Rotor Speed
P	-	Static Pressure
P_M	-	Mean Static Pressure Acted on Control Volume Annular Surfaces
r	-	Radius
$\bar{r}$	-	Mean Radius of Control Volume
S	-	Entropy
S_F	-	Entropy Production Term
T	-	Temperature
t	-	Time
V	-	Volume
W	-	Flow Rate
δ	-	Ratio of Fan or Compressor Entry Total Pressure to Standard Day, Sea-Level - Static Pressure
Θ	-	Angular Extent of Control Volume
θ	-	Angular Coordinate; Ratio of Fan or Compressor Entry Total Pressure to Standard Day, Sea-Level - Static Pressure
ρ	-	Density

SUBSCRIPTS

1	-	Fan Entrance; Left Hand Side Face of the Elemental Volume shown in Figure 17.a
2	-	Right Hand Side Face of the Elemental Volume shown in Figure 17.a
25	-	Compressor Entrance
c	-	Compressor
f	-	Fan
r	-	Radial Direction
s	-	Static
z	-	Axial Direction
θ	-	Tangential Direction

SUPERSCRIPTS

$\bar{}$	-	Volume Averaged Property
i	-	Volume Axial Face
j	-	Volume Tangential Face
k	-	Volume Radial Face

1.0 SUMMARY

The objective of the work discussed in this report was to develop a dynamic digital model for use in conducting stability studies of compression systems associated with turbofan (dual-spool) engines. This objective was accomplished through modification of the existing General Electric Dynamic Digital Blade Row Compression Component Stability Model. The modifications included the addition of compression system dual path geometry, the implementation of the matching requirements between the two spools, and the considerations for radial redistribution of the flow ahead of the fan bypass splitter.

The analytical equations on which the fan-core integrated model was based were first derived in a volume-averaged form for a three-dimensional flow. Then, they were reduced to a two-dimensional form for axisymmetric flow. The final equations satisfied the mass, axial momentum, radial momentum, and energy conservation equations for flow through a finite control volume. Use of the radial momentum equation in the model assured the radial equilibrium between the flows in the fan hub and tip regions.

The relative total-pressure loss coefficient and deviation angle blade characteristics data for the fan hub, fan tip and core compressor blade rows were calculated from TF34 fan and core performance test data. Verification of the calculated blade characteristics was conducted by reproducing 100%, 95%, 90%, and 80% clean inlet corrected speed lines for the fan hub and the fan tip; and 104.3%, 99.8%, and 94.6% clean inlet corrected speed lines for the core compressor. Validity of the compression component models was demonstrated by comparing the component results with the test data for the point of instability and the location of the stage where instability is initiated.

The fan and the core were then coupled together and the integrated system was run to instability by separately throttling the fan at 99.1% and 88.3% corrected speeds, and the core along its 104.3% and 99.8% corrected speed lines. The integrated model was then verified by comparing the model bypass ratio with that predicted by the steady-state cycle deck, and by comparing the points predicted of instability with those obtained during test program. The fan speed/core speed relationship that was needed during this program was determined from steady-state cycle deck predictions for the TF34 turbofan engine.

2.0 INTRODUCTION

One of the most significant parameters in the aerodynamic design and operation of gas turbine engines is surge margin. Aircraft engine designers are continually striving to provide adequate surge margin to ensure successful steady and transient engine operation. Operating experience has shown that the surge margin of a compressor or engine can be degraded by a variety of factors. One of the significant factors is inlet distortion in both its steady-state and time-varying forms.

Since it is not feasible to experimentally evaluate a compressor or engine for all possible distortion combinations, the need for a stability (surge) prediction technique has evolved whereby the loss of surge margin or performance can be determined analytically. Heretofore, the majority of techniques have been empirical correlations of past engine and compressor experience. However, in the recent past, GE has identified an analytical technique which is currently under development for analyzing the response of a compression component to either spatial or time-varying distortions. The GE technique is basically a one-dimensional explicit time-marching technique applied to a blade row-to-blade row model, utilizing the conservation of mass, momentum, and energy relations.

Under NASA Contract NAS3-18526, "J85 Digital Dynamic Distorted Compressor Model" (References 1 and 2), the General Electric Dynamic Digital Blade Row Compression Component Stability Model was expanded to provide a parallel-compressor analysis of circumferential total-pressure, total-temperature, and combined total-pressure/total-temperature distortions, and includes circumferential redistribution of distorted flows in blade-free volumes. The model has demonstrated the ability to accurately represent the performance of the individual blade rows when quasi-steady-state throttling is performed along a speed line. Accurate prediction of instability at the experimentally determined surge line is shown by the growth of internally generated unsteady disturbances. As part of the effort under NASA Contract NAS3-19854, "Digital Surge Prediction Analysis" (Reference 3), it was shown that these disturbances represent aerodynamic instabilities rather than numerical instabilities since a linearized stability analysis demonstrated that the real part of some of the eigenvalues of the Jacobian matrix of the system of equations changes sign from negative to positive at the point of aerodynamic instability. This change of sign is indicative of disturbances being amplified rather than attenuated. Under USAF-APL Contract F33615-75-C-2029, "Digital Model Analysis of Planar Pressure Pulse Generator (P^3G) and Two-Stage Fan Test Data" (Reference 4), the response of a fan to planar waves was predicted and compared with existing test results. Analysis of the comparisons showed that the model

accurately reproduced the wave shape, amplitude, and phase-angle responses up to a reduced frequency of 0.2. Accurate levels of planar-wave distortion transfer coefficient were predicted, and the proper trends of sensitivity to surge with frequency were predicted.

However, to date all efforts have been directed towards modelling only turbojet compression systems or the compression components of turbofan engines. Turbofan, multi-spool engines are characterized by one or two compression components on each spool. NASA-Lewis Research Center, in recognition of the need to develop stability models of more advanced technology compression systems such as turbofan engines, initiated the effort discussed in this report. The objective of this program was to obtain a dynamic digital blade row model of the TF34 compression system. This compression system is composed of a single-stage fan without inlet guide vanes (IGV) on the low speed spool, and a fourteen-stage compressor on the high speed spool. The IGV and the first five stages of compressor are variable and are scheduled as functions of corrected speed. The primary development item in this effort was to develop a method for properly handling the matching of the two spools. This was accomplished by allowing for radial redistribution of the flow in the blade free volumes ahead of the leading edge of the splitter and upstream of the fan.

The existing General Electric Dynamic Digital Blade Row Compression Component Stability Model, now known as the Dynamic Analysis Program (DYNAP), was modified to permit simulation of the TF34 compression system. This was accomplished by modelling the flow path geometry of the TF34 fan, compressor, and combustor and making an allowance to operate with two spools. The fan speed and core speed relationship was defined using the results from cycle deck studies. This relationship was used to assure that the proper speed match was maintained between spools as either the core or the fan bypass was throttled up a speed line.

The single-stage fan hub, tip and mass-averaged maps were analyzed to produce steady-state blade row characteristics (relative total-pressure loss coefficients and deviation angles) which are representative of the hub and tip regions and the mass-averaged performance of the fan for corrected speeds of 80, 90, 95, and 100 percent. The core engine interstage data was stacked for the fourteen stages and analyzed to produce pitch-line blade row characteristics (loss coefficient and deviation angle) for the compressor at corrected speeds of approximately 95, 100, and 105 percent.

The above described modifications to the computer model were verified by throttling the fan hub, the fan tip, and the core compressor components up their respective set of clean inlet speed lines to demonstrate speed line

and surge point replication. The stage initiating instability in the compressor was identified and compared with interstage data results. The components were then coupled together and the system was run to instability by separately throttling the fan and the core to their component surge lines. The bypass ratio migration compared favorably with the results of cycle deck studies.

3.0 TF34 ENGINE COMPRESSION COMPONENT ANALYSIS

Preparatory to developing a TF34 Compression System Model, the TF34 fan and compressor were individually modelled, the stability characteristics of each were determined, and the results were compared with test data. These efforts are documented in this section of the report.

3.1 FAN COMPONENT

The TF34-GE-100 fan which is a single stage fan composed of a rotor and an outlet guide vane (OGV) was tested as a full scale component in the General Electric Large Fan Test Facility located in Lynn, Massachusetts. The splitter/gooseneck and the fan bypass flow duct were simulated. The bypass ratio was controlled through the use of both the main discharge valve and the bypass discharge valve.

The fan was throttled at constant corrected speed to obtain the speed lines and surge points. The results of these throttlings are shown in Figures 1, 2, and 3 as the overall, tip, and hub maps, respectively for 80%, 90%, 95%, and 100% corrected speeds.

There are two items which should be noted with respect to these figures. The first is that the tip map is based upon the flow entering the bypass duct and the hub map is based upon the flow entering the core. The overall performance map is then obtained by mass weighting the hub and tip performance parameters. The second is that the so called surge line is defined by a stress boundary below approximately 102% corrected speed and by aerodynamic instability (surge or rotating stall) above this speed.

The fan was modelled using thirteen volumes (see Figure 4) as follows:

5 inlet volumes
1 rotor volume
1 interaxial gap volume
1 stator volume
5 discharge volumes

This representation and the methods used for the analyses conducted during this study are similar if not identical to those reported in Reference 1 and 3. The length of the volumes was set so as not to exceed the length of the longest blade row, the rotor. The blade characteristics in terms of rotor relative total-pressure loss coefficient and deviation angle were determined for the four corrected speeds of interest using the fan performance infor-

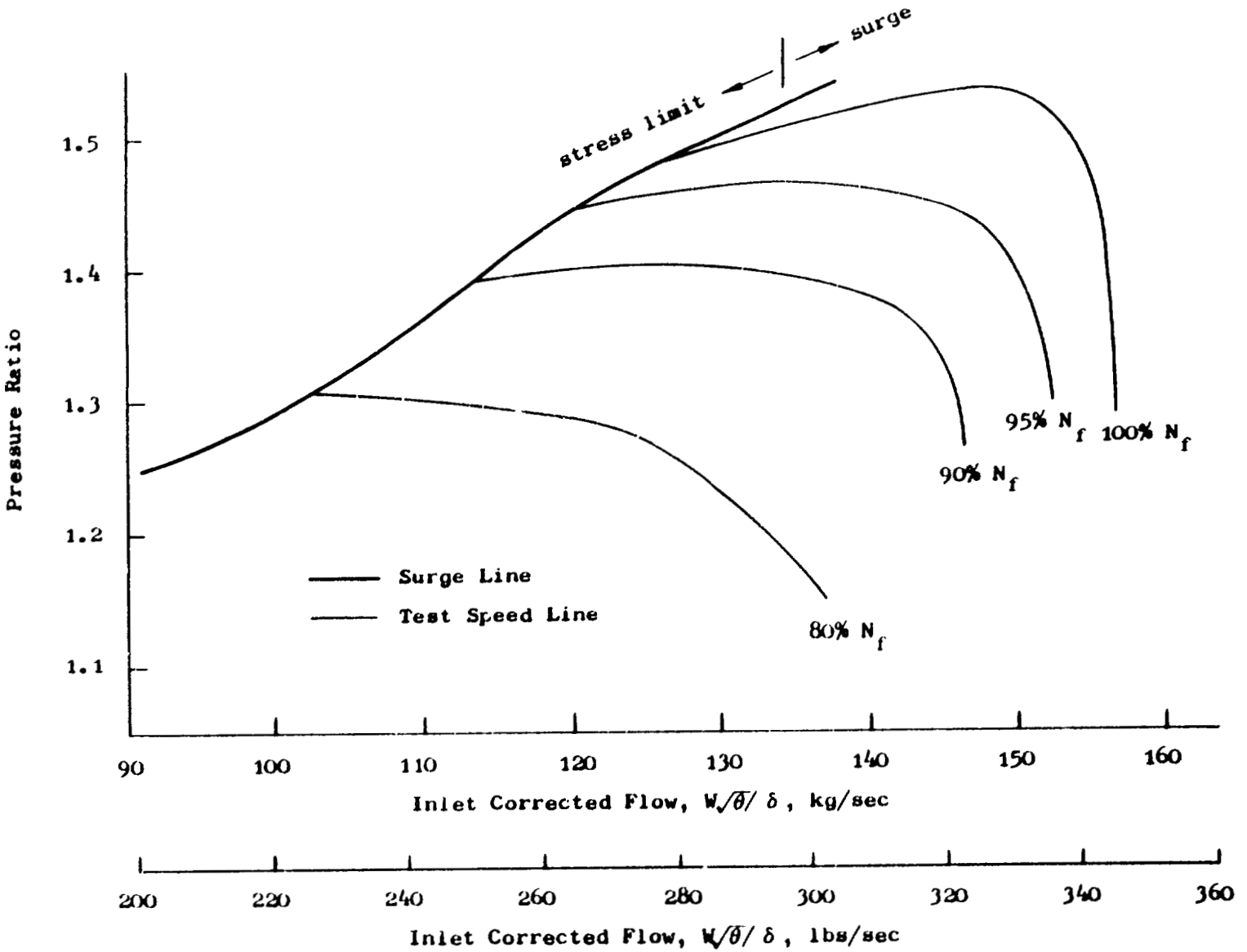

Figure 1. TF34 Fan Overall Performance

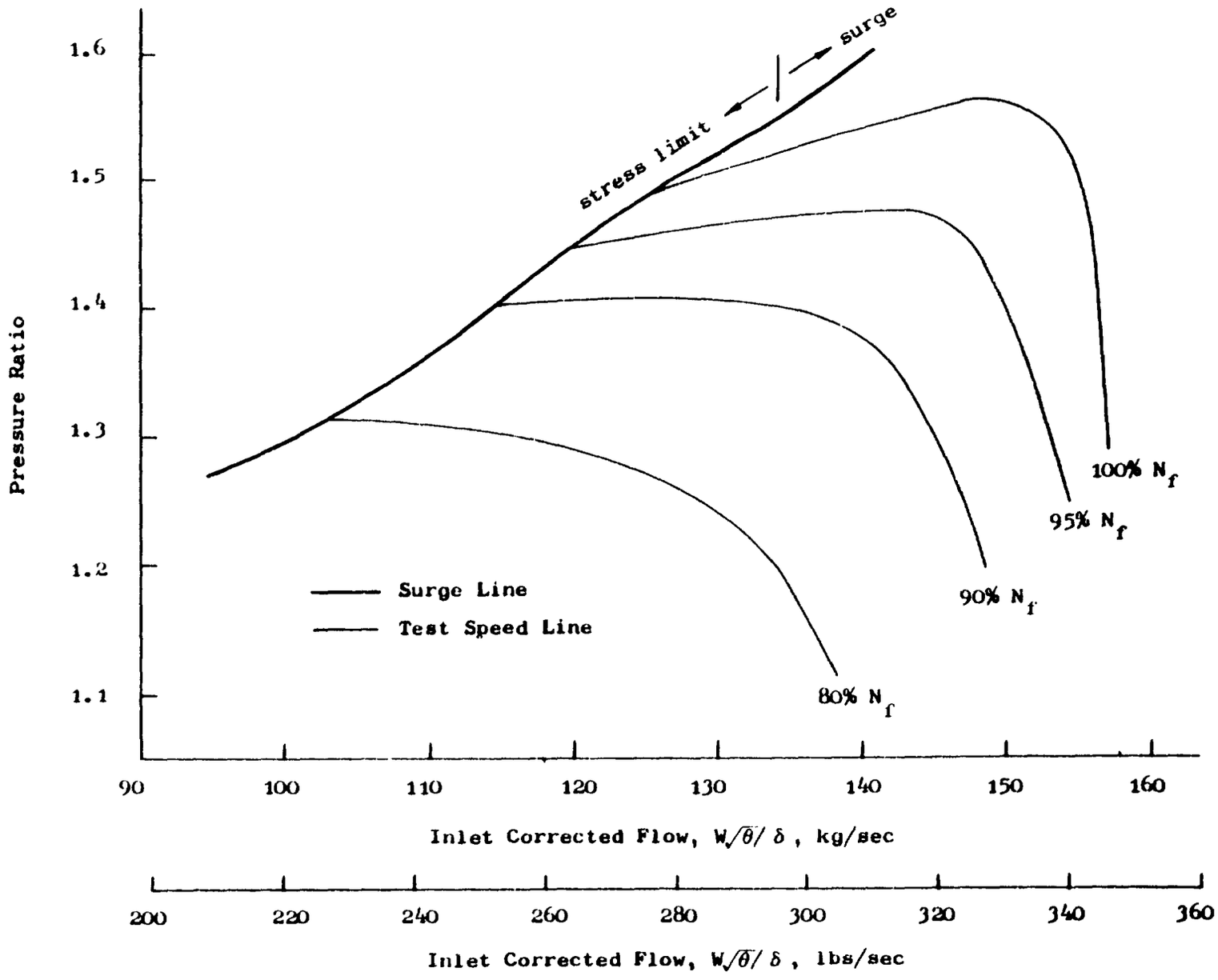

Figure 2. TF34 Fan Tip Performance

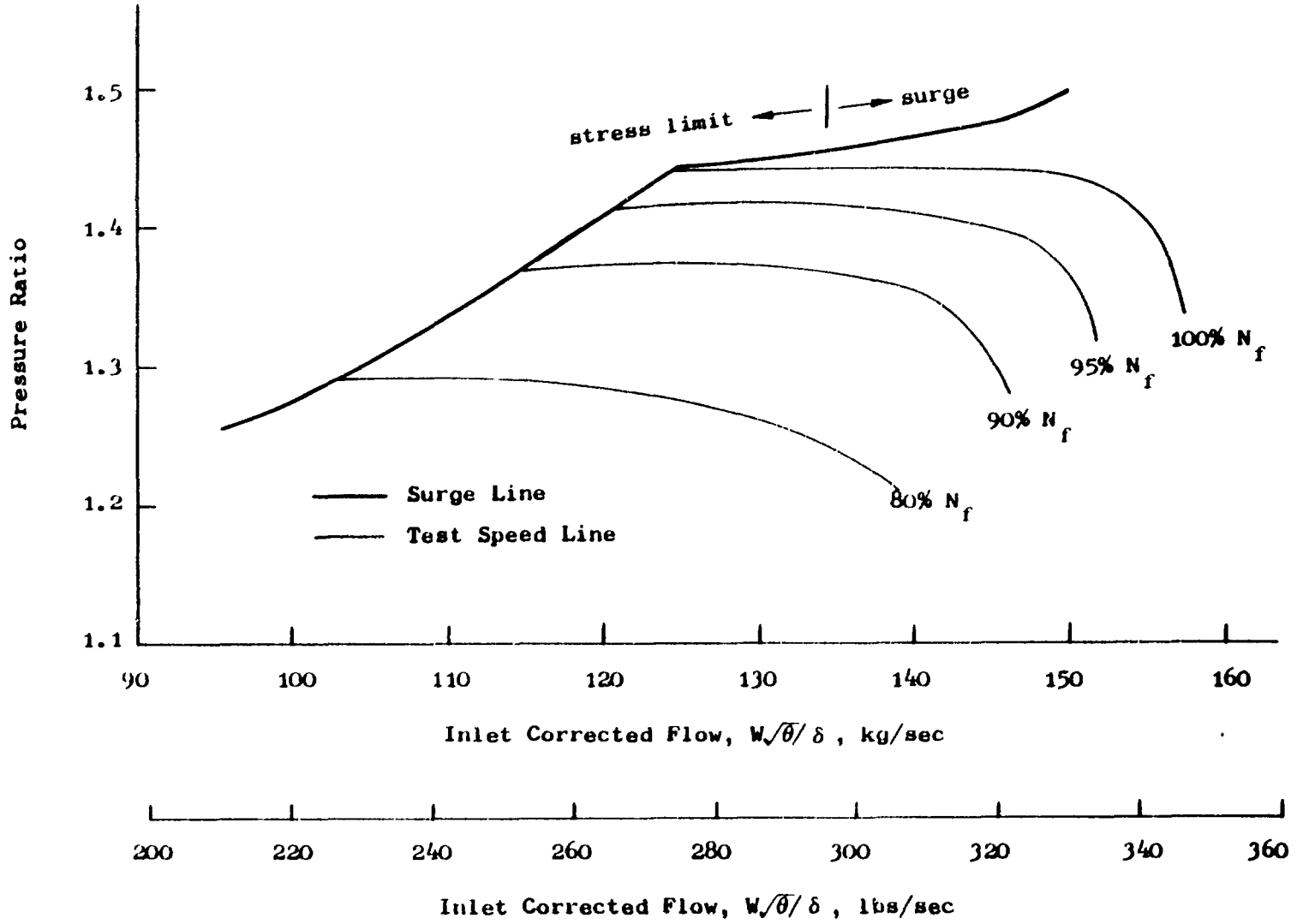

Figure 3. TF34 Fan Hub Performance

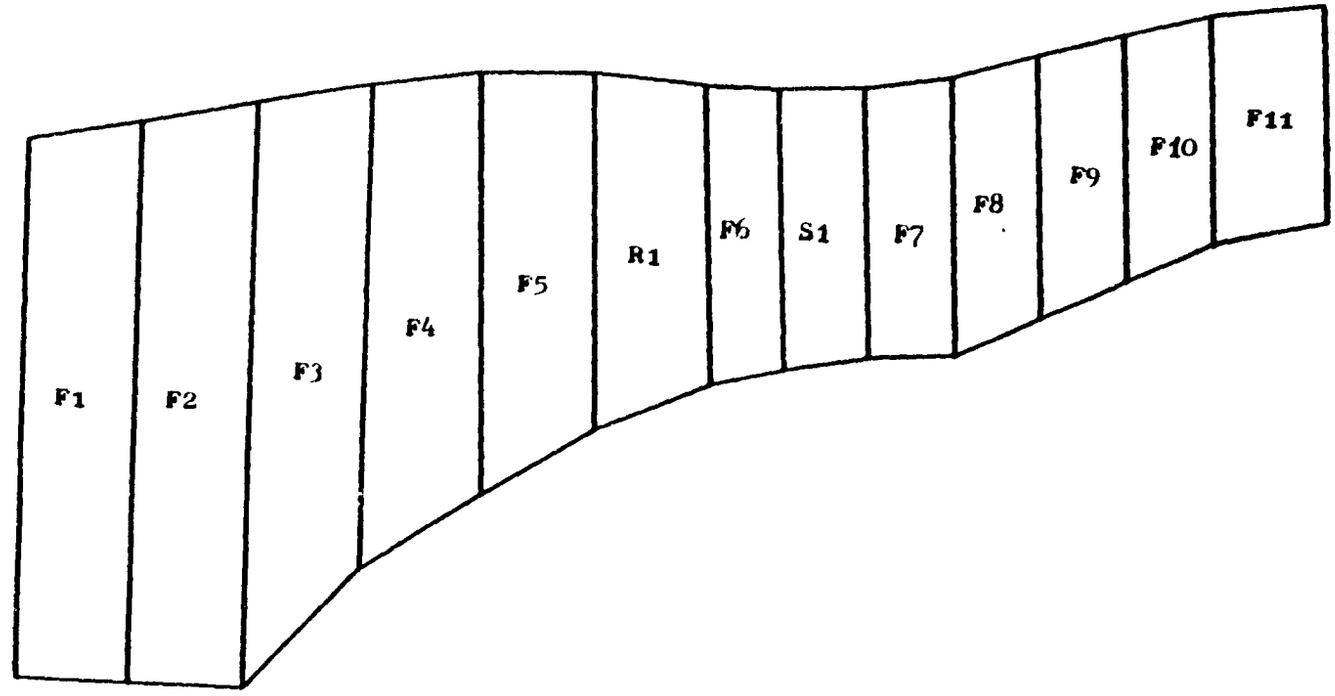

Figure 4. Schematic of the Fan Model Volumes.

mation in conjunction with the fan geometry. In the absence of test data, the stator was assumed to be lossless. The model representations of the speed lines are shown in Figures 5, 6, and 7 as the dashed lines for the overall, tip, and hub performances, respectively. The agreement between the test and model speed lines is excellent especially in the low flow regions of the speed lines (near surge) with some small deviations noted in the high flow regions of the speed line.

Stability predictions were made using the techniques of Reference 3 and the results are shown also on Figures 5, 6, and 7 by the open and solid circles. The open circles denote the region of aerodynamic stability (all roots of the characteristic equation of the Jacobian matrix have negative real parts) while the solid circles denote a region of aerodynamic instability (one or more roots of the characteristic equation of the Jacobian matrix have a positive real part). The stability predictions based upon the overall performance characteristics appear to match the test data quite well (Figure 5) near to where aerodynamic surge was observed. As expected in the region where the surge line is set by stress limitations, the erodynamic instability occurs at a lower flow. Examination of Figures 6 and 7, the tip and hub characteristics respectively, shows that the fan stability limits are set by the tip characteristics. That is, as the fan is throttled to surge, fan surge (stall) will originate at the tip of the fan. This finding agrees with test experience which indicates that the fan is tip sensitive.

3.2 COMPRESSOR COMPONENT

The TF34-GE-100 core was tested in the General Electric Multipurpose Test Facility located in Evendale. The test assembly included an exit flow duct to simulate the combustor flow path and an inlet duct faired into the gooseneck to simulate the core inlet flow path. The core compressor is a 14 stage axial compressor with variable IGV and stators 1 to 5. The IGV and stators are ganged and controlled as a function of corrected speed with a $T_{t_{25}}$ bias. Although the TF34-GE-100 core compressor has stage 7 and 10 bleeds, the test was performed with the bleed ports blanked off. Clean inlet compressor performance and stall mapping tests were conducted to obtain the 94.6%, 99.8%, and 104.3% corrected speed lines which are shown in Figure 8.

The compressor model consists of forty-one volumes. There are 29 volumes consisting of the IGV, rotors 1-14, and stators 1-14; and 12 free volumes consisting of two volumes ahead of the IGV and 10 volumes ahead of the turbine diaphram. The axial lengths of the free volumes are chosen not to exceed the length of the longest blade axial chord. Figure 9 shows the schematic configuration of the model.

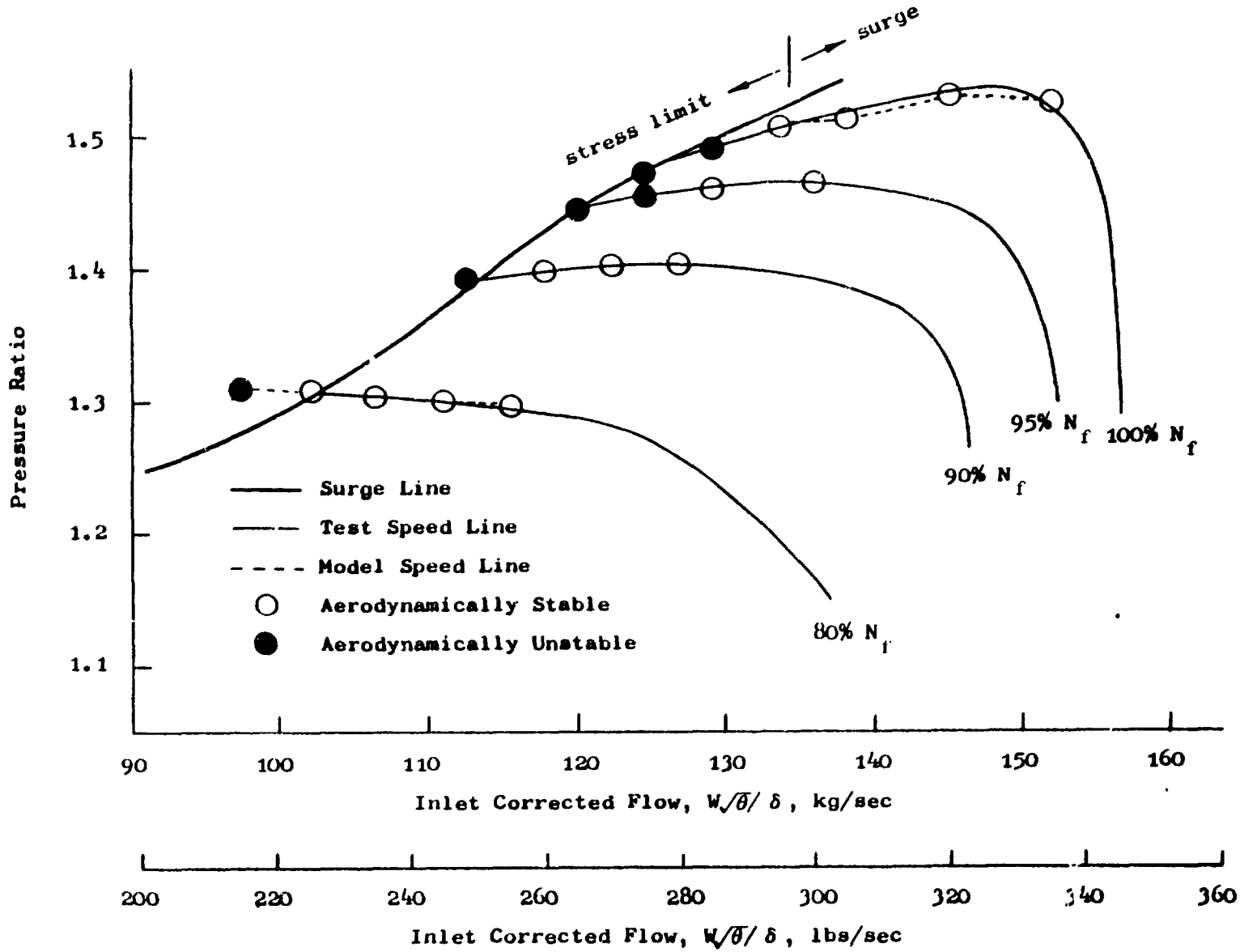

Figure 5. Model Representation of TF34 Fan Overall Performance

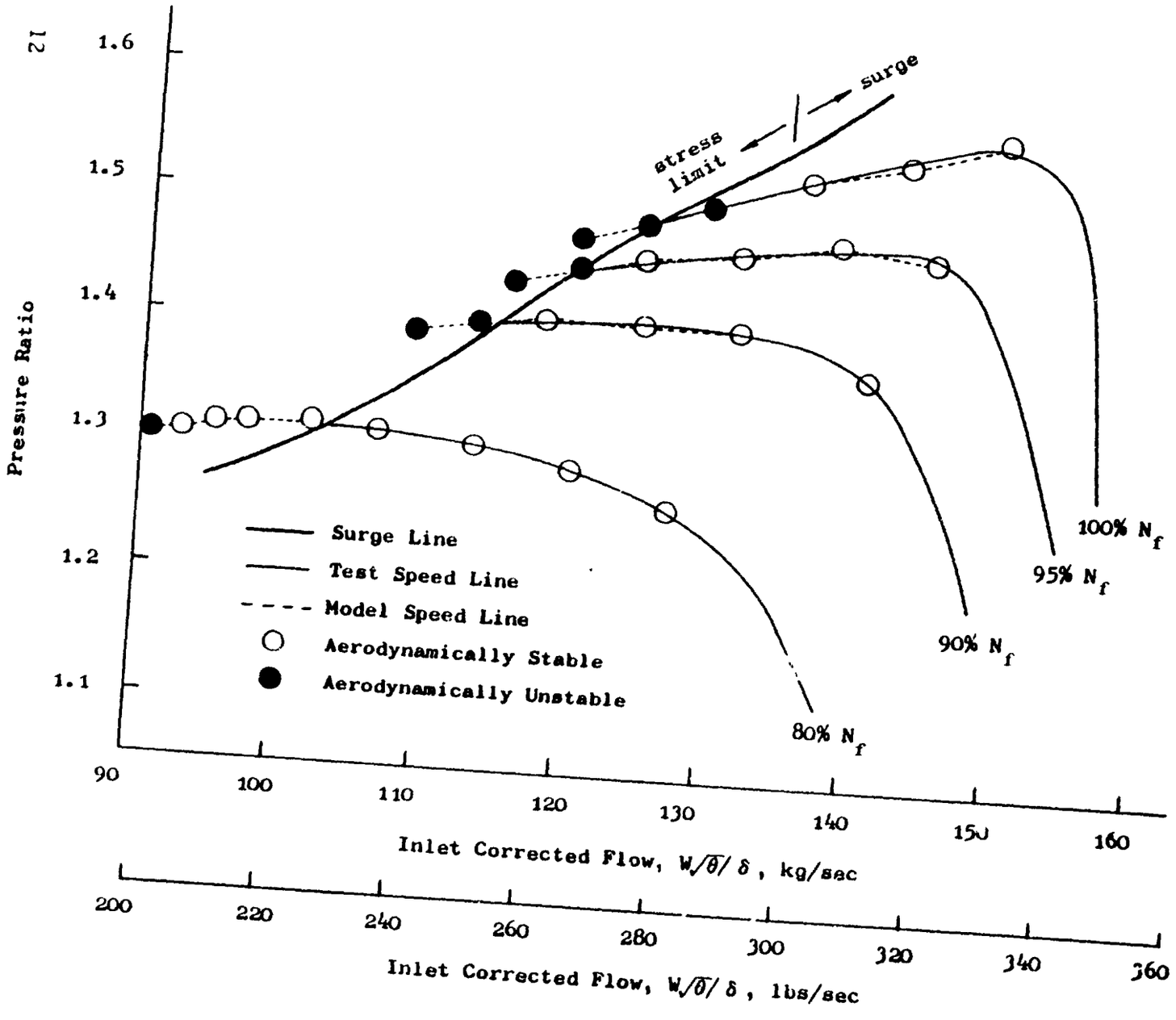

Figure 6. Model Representation of TF34 Fan Tip Performance

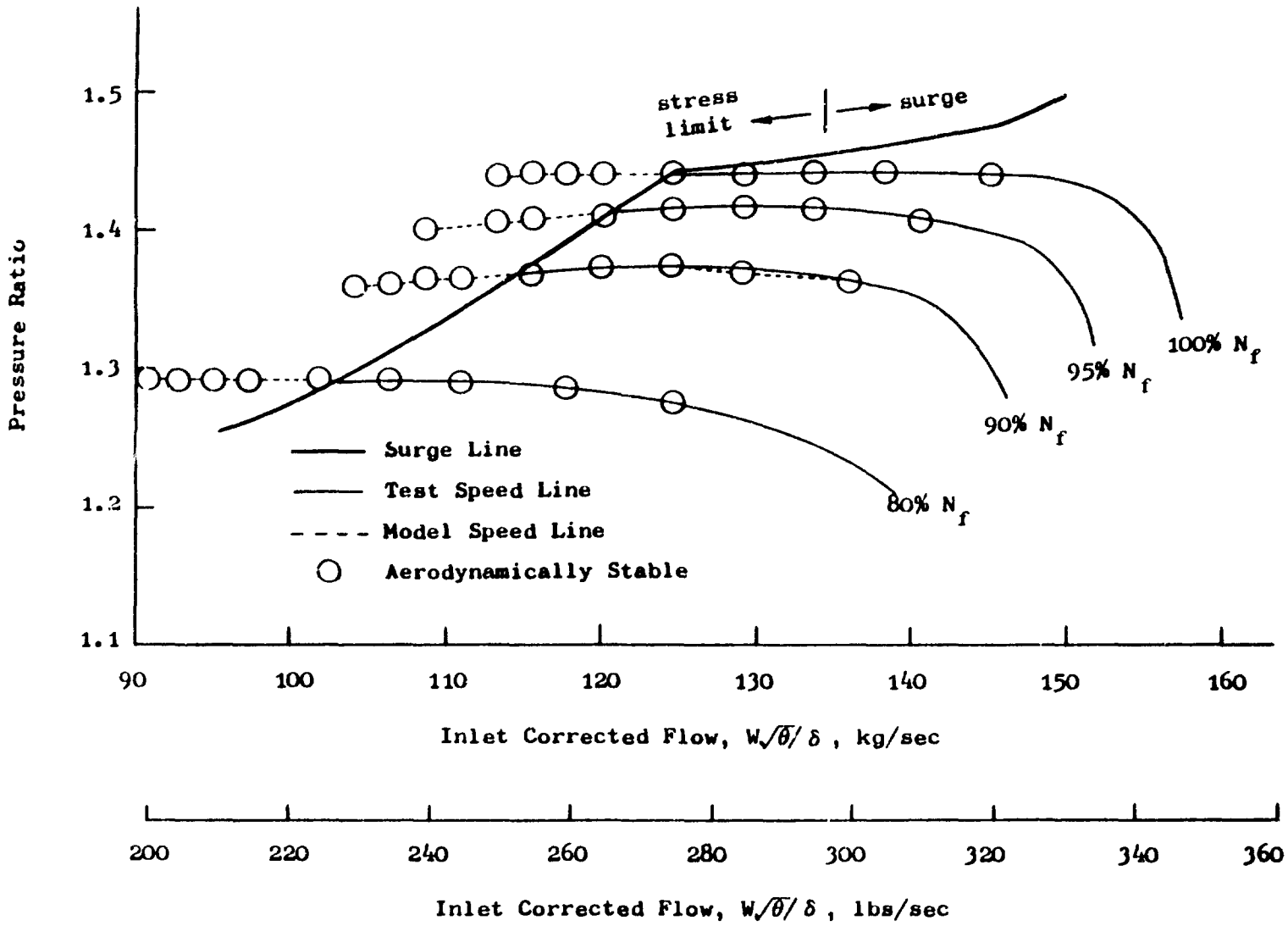

Figure 7. Model Representation of TF34 Fan Hub Performance

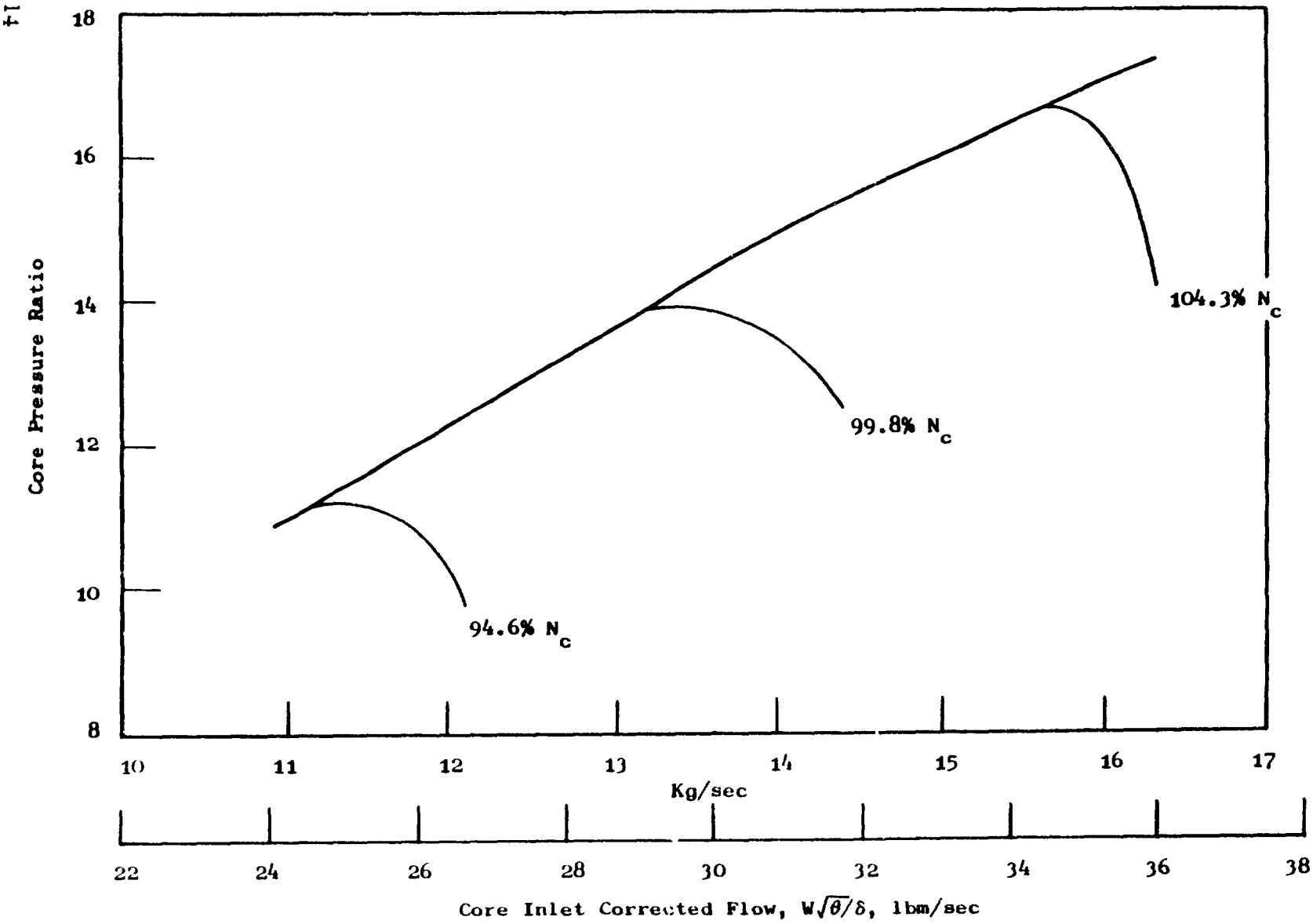

Figure 8. TF34 Core Compressor Performance Map.

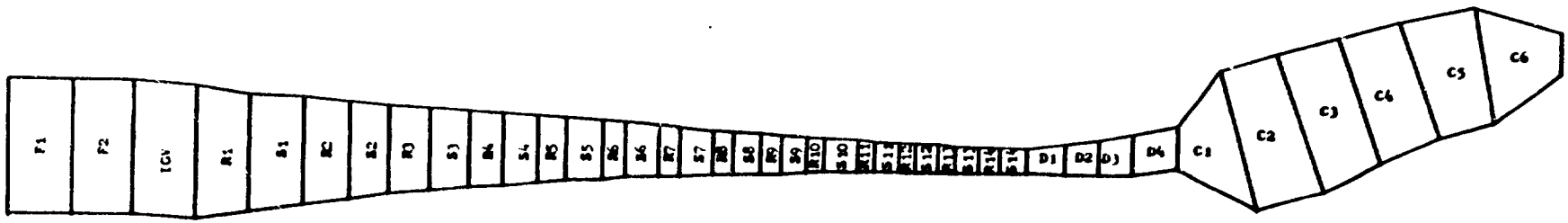

Figure 9. Schematic of the Core Model Volumes.

The blade characteristics, relative total pressure loss coefficient and deviation angle, were determined from the stage characteristics, work and pressure coefficients, provided by the Lynn Compressor Design personnel. Figure 10 illustrates the performance of the compressor as calculated using the derived blade characteristics in polynomial form. Excellent comparison with the demonstrated performance is observed at the 94.6%, 99.8%, and 104.3% corrected speeds.

Stability analyses were performed using the linearized stability technique of Reference 3. The results shown in Figure 11 indicate very good agreement between the demonstrated and predicted stability points for 94.6% and 104.3% corrected speeds. The predicted stability point at 99.6% corrected speed is 0.2 Kg/sec (0.5 lbm/sec) high in flow as compared to the experimental point. It is also interesting to note that the predicted stability point at 94.6% corrected speed does not occur at the peak pressure ratio, but rather on the positive slope portion of the speed line.

A time-dependent model of the compressor was constructed using DYNAP for the purpose of conducting throttling-to-surge simulations. The compressor was represented in exactly the same manner as it was for the linearized analyses. The objective of these simulations was to determine what correlation, if any, existed between model observed surge line instabilities and test observed instabilities. The results are given in Table 1.

Table 1. Instability Initiating Stage

Corrected Speed	Model Results	Test Results	
		Surge	Rotating Stall
94.6	10 and 1 Simultaneously	9-10	2
99.8	10	11	-
104.3	1 and 2 followed by 11	13-14	4

Examination of the throttling to surge simulations showed the anticipated instabilities (based upon the amplification function of Reference 1) developing in the back end of the compressor. Test data obtained from a TF34 core engine test using two high-response wall-static pressure transducers mounted approximately 150° apart and aligned axially showed the surge pulse to develop in the back end of the compressor. The surprising result obtained from the simulations was the near simultaneous occurrence of instabilities in the front end of the compressor. Reexamination of the test results showed that rotating stall cells in the forward stages occurred at approximately the same time as the rear developing surge pulses.

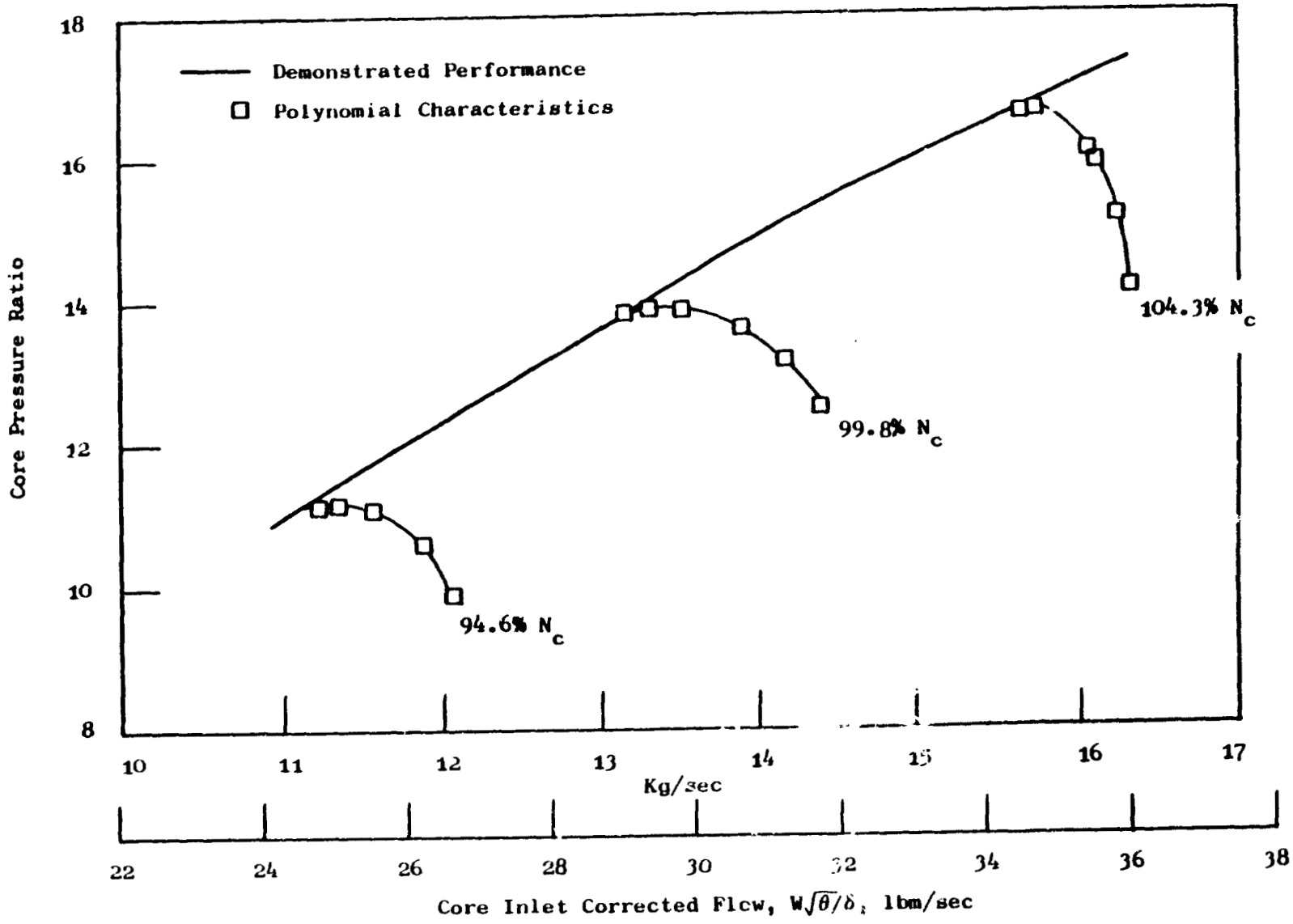

Figure 10. Comparison of TF34 Core Compressor Performance Demonstrated and Calculated.

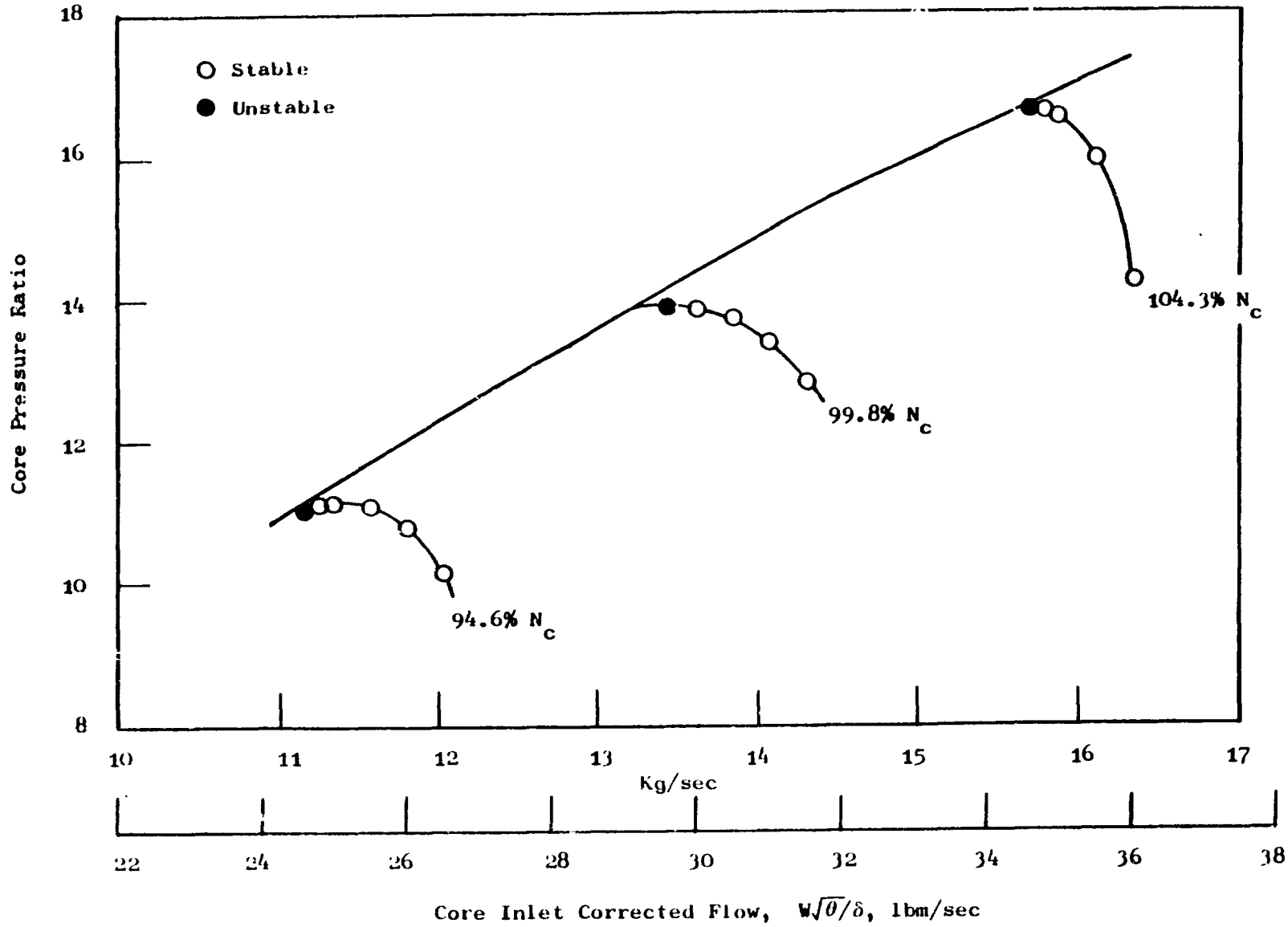

Figure 11. TF34 Core Compressor Stability Check.

These results are further verification of the capabilities of the General Electric Dynamic Analysis Program (DYNAP) especially its ability to predict the regions in the compressor where instabilities will develop during throttling. However, since DYNAP is a quasi one-dimensional model it does not give the nature of the instability, that is, surge or rotating stall. This determination is left to obtaining and examining test data or developing and obtaining results from multi-dimensional models.

4.0 TF34 ENGINE COMPRESSION SYSTEM ANALYSIS

In this section of the report, the analytical model for the computations of TF34 compression system flow dynamic behavior is discussed. The model is capable of simulating the interaction between the fan and the core compressor. Radial exchange between the fan hub and tip regions of the flow was considered to allow for the variation in the bypass flow ratio. This objective was accomplished by extending the one-dimensional time-dependent model, reported in Reference 1 to allow for radial flow redistribution.

A brief description of the fan-compressor integrated compression system will be given in this section and will be followed by a generalized three-dimensional macroscropic balance flow analysis. The equations will then be reduced to describe a two-dimensional axisymmetric flow.

4.1 COMPRESSION SYSTEM MODEL DESCRIPTION

The TF34 compression system has a single stage fan without an inlet guide vanes, and a fourteen-stage compressor. The IGV and the first five stages of the core compressor are variable and are scheduled as functions of the corrected speed. In addition to the fan and compressor, the model geometry, as shown in Figure 12, includes the fan inlet duct, the bypass duct, the gooseneck, and the combustor. The purpose of including these duct volumes is to assure that realistic propagation paths for unsteady disturbances are simulated.

The compression system was divided in sixty volumes, as shown in Figure 13. The fan inlet duct is represented by four volumes; the fan including the interaxial gap between the rotor and the stator, and the fan exit ducting to the bypass splitter by eight volumes; the bypass duct by four volumes; the gooseneck by five volumes; the compressor by twenty-nine volumes; the compressor discharge diffuser by four volumes; and the combustor by six volumes. All volumes ahead of the bypass splitter, including the fan rotor and stator, were divided into tip and hub volumes with a split stream-surface as shown in Figure 13. The split stream-surface extends from the bypass splitter to the fan inlet and divides the entering flow into tip and hub flow rates in a ratio approximating the flow averaged bypass ratio.

4.2 DEVELOPMENT OF QUASI-THREE DIMENSIONAL DYNAMIC MODEL

The concepts used in the one-dimensional model of Reference 1 are extended to include the compression system associated with a turbofan engine. The difficulties dealing with such systems do not only arise from having

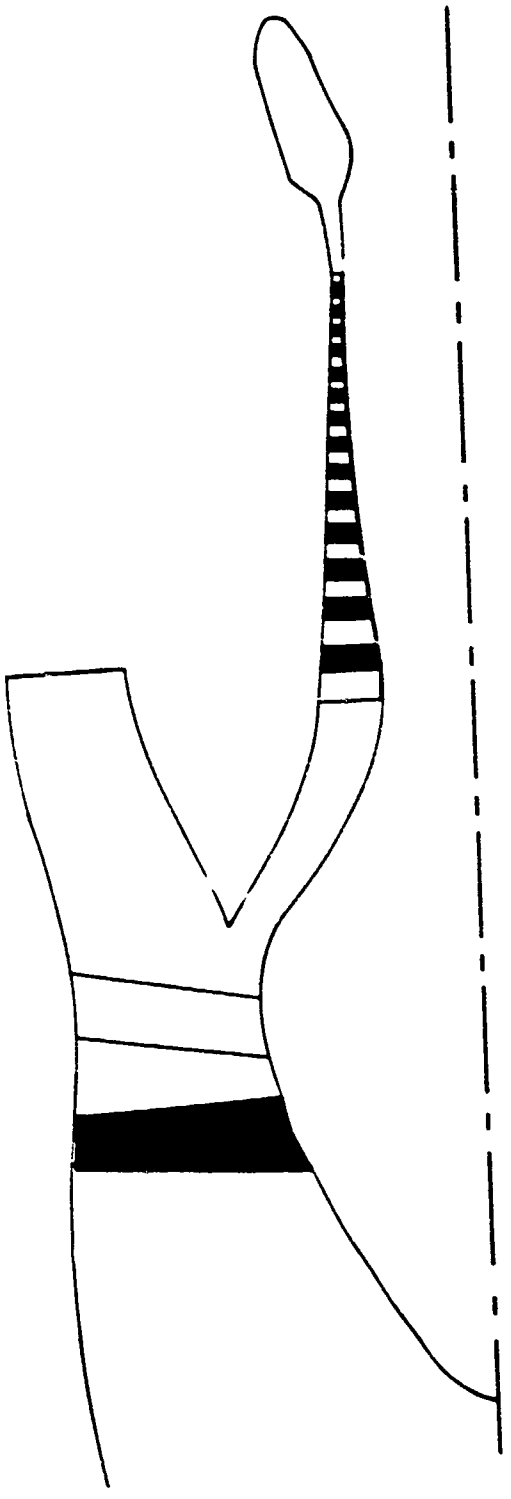

Figure 12. Sectional View of TF-34 Compression System.

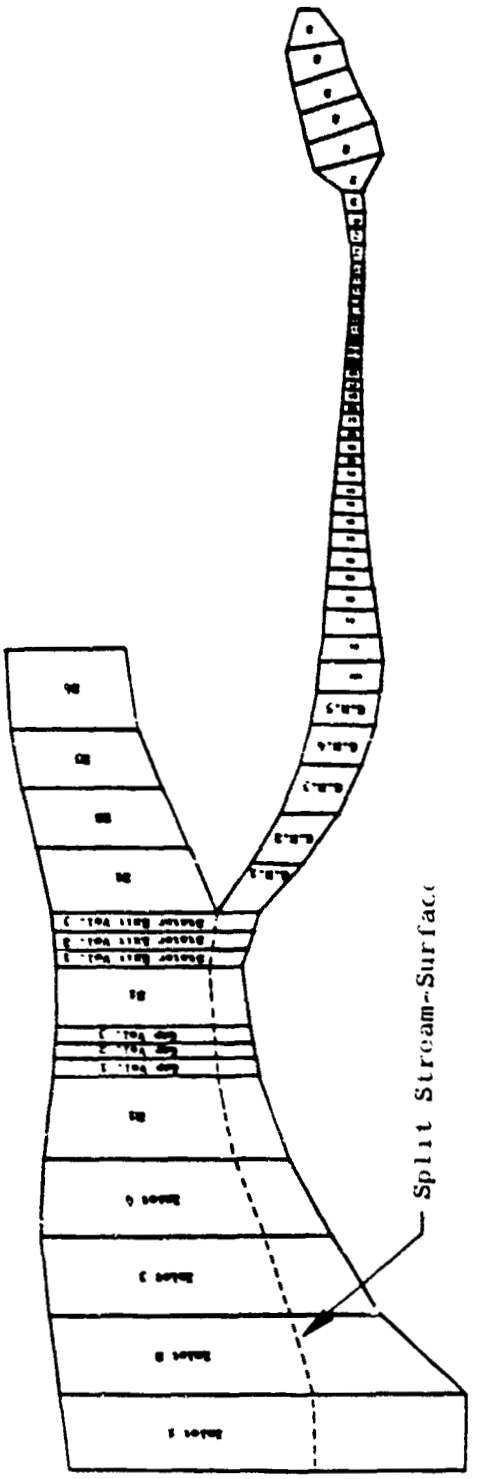

Figure 13. Schematic of Model Volumes.

dual compression units, but also from handling different bypass ratios. With different bypass ratios, the annulus stream surface separating core and fan bypass flows will migrate radially. Instead of dealing with variable surface boundary, a fixed split stream-surface is considered and radial flow is allowed to cross this artifical boundary. In the following paragraphs, the integral equations of motion will be written in general form and then will be simplified to a degree suitable for our present model.

4.2.1 Governing Equations

The equations of motion are derived for a general control volume, V, covering a segment of a concentric ring. Figures 14a and 14b show the notation used to identify the location of the control volume and the geometrical characteristics used in the equations. Variables with superscript, "i", "j", or "k" will denote the variables at axial, circumferential or radial faces of the control volume, respectively.

Flow rates and velocities used in the equations of motion are depicted in Figures 15a to 15c. Figure 15a illustrates the flows entering and leaving the control volume surfaces, while flow velocities normal and tangential to the control surfaces are shown in Figures 15b and 15c, respectively. In the following derivations, the bar above variables indicates control-volume-averaged properties.

Mass Conversation

The integral equation representing the conservation of mass can be written as follows:

$$\begin{bmatrix}\text{Rate of}\\ \text{Mass}\\ \text{Accumulation}\end{bmatrix} = \begin{bmatrix}\text{Rate of}\\ \text{Mass}\\ \text{In}\end{bmatrix} - \begin{bmatrix}\text{Rate of}\\ \text{Mass}\\ \text{Out}\end{bmatrix} \qquad (1)$$

or

$$\frac{\partial}{\partial t}\int \rho \, dV = (W_z^i - W_z^{i+1}) + \{W_\theta^j - W_\theta^{j+1}\} + \{W_r^k - W_r^{k+1}\} \qquad (2)$$

Where W_z^i, W_θ^j, W_r^k, are the mass flows into the axially-facing, tangentially-facing and radially-facing surfaces, respectively.

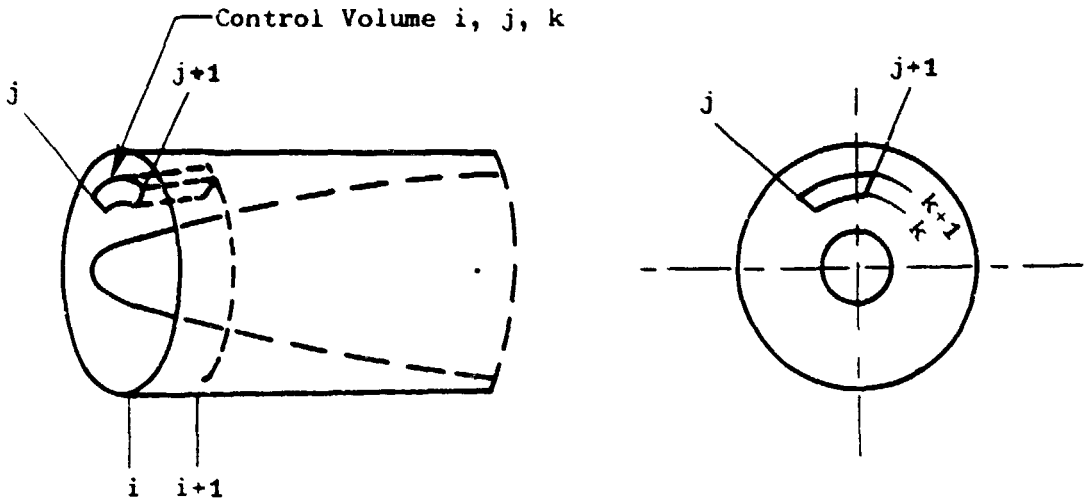

a. Control Volumes Arrangement

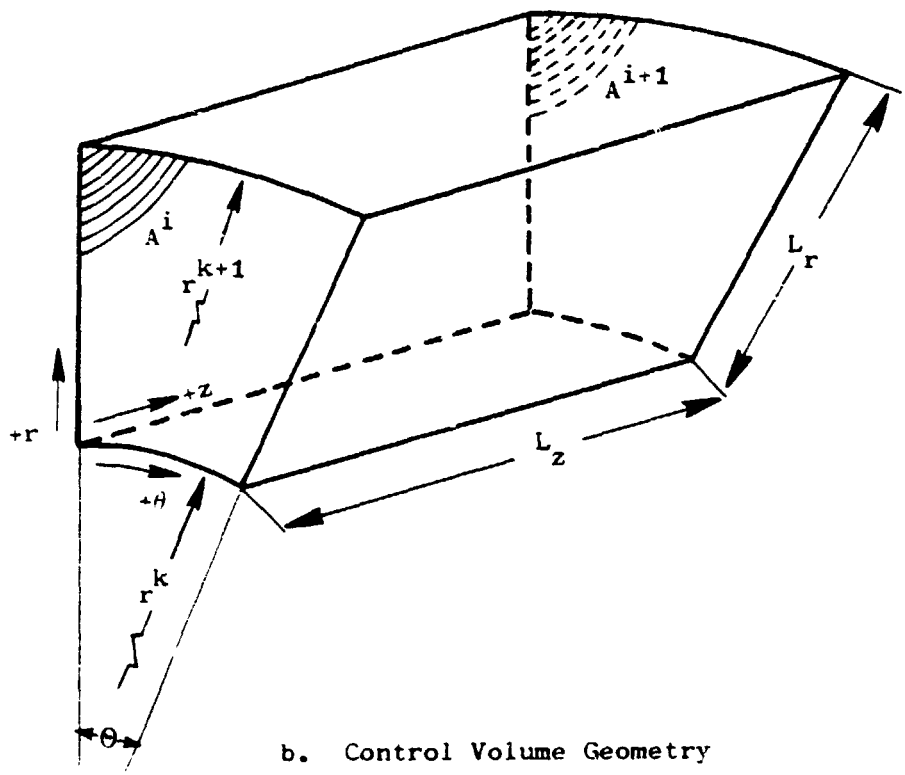

b. Control Volume Geometry

Figure 14. Control Volume.

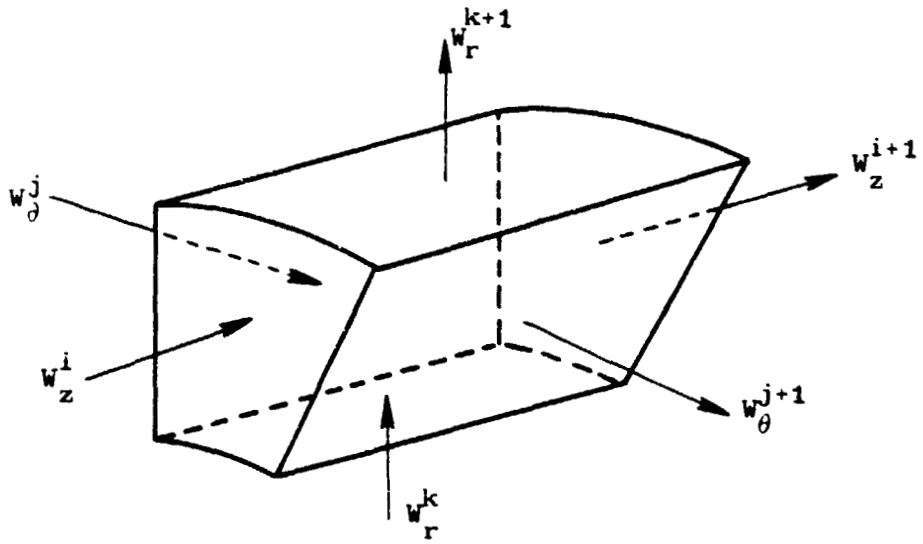

a. Flow Rates

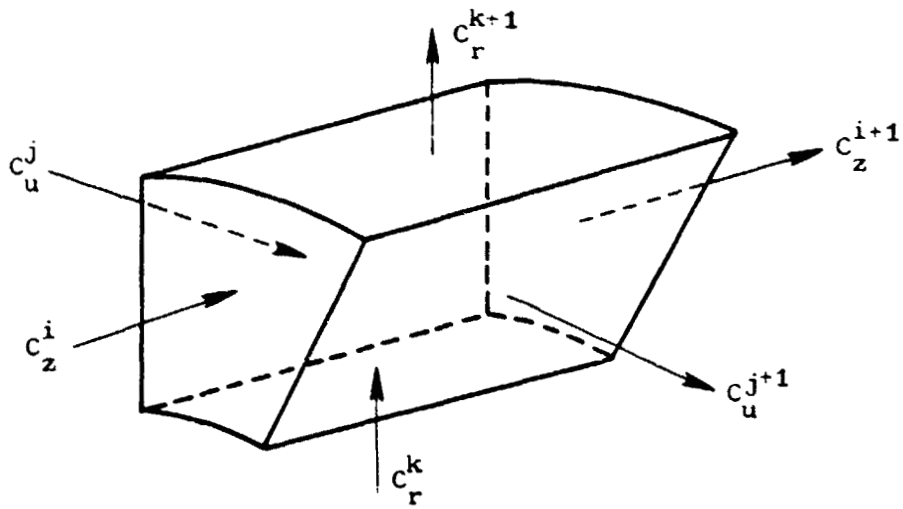

b. Normal Velocity Components

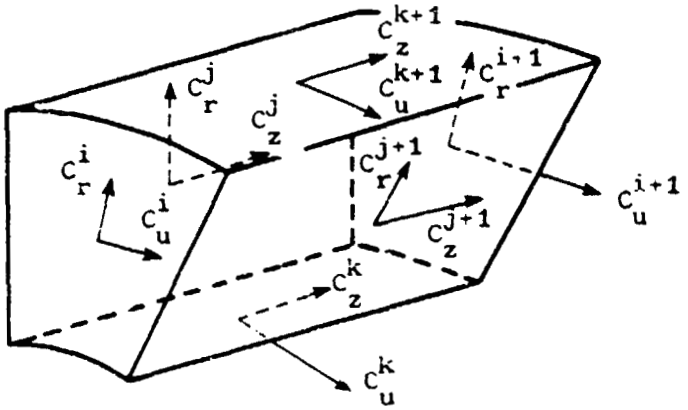

c. Tangential Velocity Components

Figure 15. Control Volume Flow Rates and Velocities.

Let $\bar{\rho}$ represent the spatially averaged density over the control volume V.

$$\text{i.e.} \quad \bar{\rho} = \frac{\int \rho \, dV}{\int dV} = \frac{1}{V} \int \rho \, dV \tag{3}$$

Application of this definition to the mass conservation equation results in

$$\frac{\partial \bar{\rho}}{\partial t} = \frac{1}{V} \left[(W_z^i - W_z^{i+1}) + \{ W_\theta^j - W_\theta^{j+1} \} + \{ W_r^k - W_r^{k+1} \} \right] \tag{4}$$

Momentum Conservation

The integral equation representing the conservation of momentum in a given direction can be written as:

$$\begin{bmatrix} \text{Rate of} \\ \text{Momentum} \\ \text{Accumulation} \end{bmatrix} = \begin{bmatrix} \text{Rate of} \\ \text{Momentum} \\ \text{In} \end{bmatrix} - \begin{bmatrix} \text{Rate} \\ \text{Momentum} \\ \text{Out} \end{bmatrix} + \begin{bmatrix} \text{Sum of} \\ \text{Forces Acting} \\ \text{On Control Volume} \end{bmatrix} \tag{5}$$

Application of Equation 5 to the axial direction and use of Figure 16a result in the following axial momentum equation.

$$\frac{1}{g_o} \frac{\partial}{\partial t} \int (\rho C_z dV) = \left(\frac{W_z^i C_z^i}{g_o} - \frac{W_z^{i+1} C_z^{i+1}}{g_o} \right) + \left\{ \frac{W_\theta^j C_z^j}{g_o} - \frac{W_\theta^{j+1} C_z^{j+1}}{g_o} \right\}$$

$$+ \left\{ \frac{W_r^k C_z^k}{g_o} - \frac{W_r^{k+1} C_z^{k+1}}{g_o} \right\} + (P^i A^i - P^{i+1} A^{i+1})$$

$$- P_M (A^i - A^{i+1}) + F_z \tag{6}$$

The axial momentum of the fluid inside the control volume can be written as

$$\int \rho C_z dV = \overline{\rho C_z} V = \overline{\rho C_z} A_z L_z = \bar{W}_z L_z \tag{7}$$

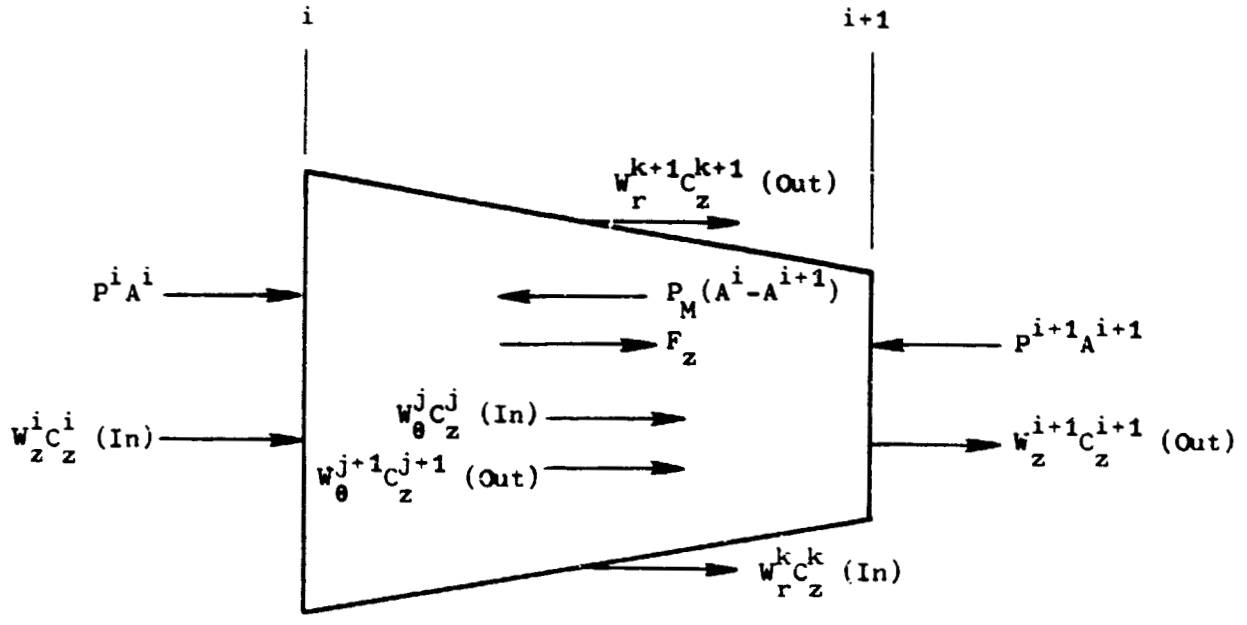

a. Axial Momentum Balance

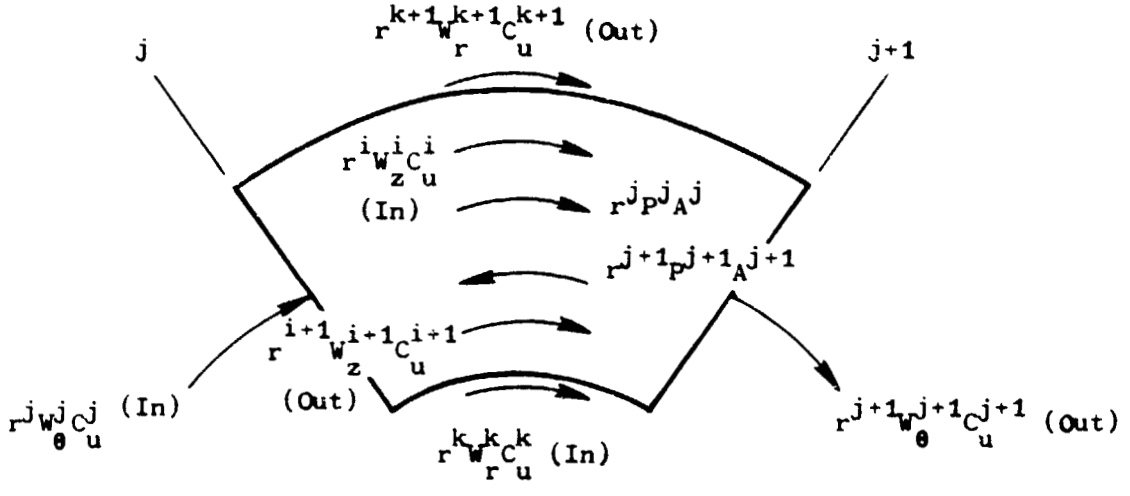

b. Angular Momentum Balance

Figure 16. Axial and Angular Momentum Balance.

where the bar indicates volume averaged quantities and L_z is the control volume length in the axial direction. Therefore, the axial momentum equation can be written in the following form:

$$\frac{\partial \bar{W}_z}{\partial t} = \frac{g_o}{L_z}\left[\frac{W_z^i C_z^i}{g_o} - \frac{W_z^{i+1} C_z^{i+1}}{g_o} + \left\{\frac{W_\theta^j C_z^j}{g_o} - \frac{W_\theta^{j+1} C_z^{j+1}}{g_o}\right\}\right.$$

$$\left. + \left\{\frac{W_r^k C_z^k}{g_o} - \frac{W_r^{k+1} C_z^{k+1}}{g_o}\right\} + (P^i A^i - P^{i+1} A^{i+1}) - P_M(A^i - A^{i+1}) + F_z\right] \quad (8)$$

The principle of conservation of angular momentum is similar to the principle of the conservation of linear momentum. Application of Equation 5 to the blade-free control volume shown in Figure 16b and manipulation of the different terms result in the following equation:

$$\frac{\partial \bar{W}_\theta}{\partial t} = \frac{g_o}{\bar{r} L_\theta}\left[\frac{r^i W_z^i C_u^i}{g_o} - \frac{r^{i+1} W_z^{i+1} C_u^{i+1}}{g_o} + \frac{r^j W_\theta^j C_u^j}{g_o} - \frac{r^{j+1} W_\theta^{j+1} C_u^{j+1}}{g_o}\right.$$

$$\left. + \frac{r^k W_r^k C_u^k}{g_o} - \frac{r^{k+1} W_r^{k+1} C_u^{k+1}}{g_o} - r^j P^j A^j - r^{j+1} P^{j+1} A^{j+1}\right] \quad (9)$$

It should be noted that this equation is only valid for blade-free volumes since the tangential blade force is not included.

Upon writing the momentum balance based upon Equation 5 in the radial direction for the blade-free elemental volume shown in Figure 17 and upon integrating over the control volume, the following radial momentum equation is obtained (see Appendix A):

$$\frac{\partial \bar{W}_r}{\partial t} = \frac{g_o}{L_r}\left[\frac{W_r^k C_r^k}{g_o} - \frac{W_r^{k+1} C_r^{k+1}}{g_o} + \frac{W_z^i C_r^i}{g_o} - \frac{W_z^{i+1} C_r^{i+1}}{g_o} + \frac{W_\theta^j C_r^j}{g_o}\right.$$

$$\left. - \frac{W_\theta^{j+1} C_r^{j+1}}{g_o} + \frac{\Theta \bar{W}_\theta \bar{C}_u}{g_o} + \frac{1}{2}(P^k - P^{k+1})(r^k + r^{k+1}) L_z \Theta\right] \quad (10)$$

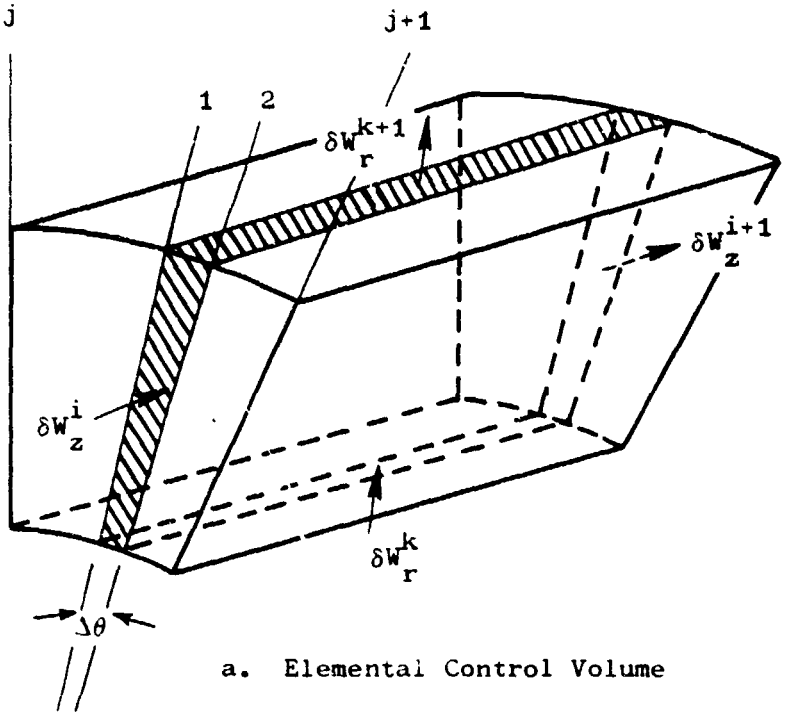

a. Elemental Control Volume

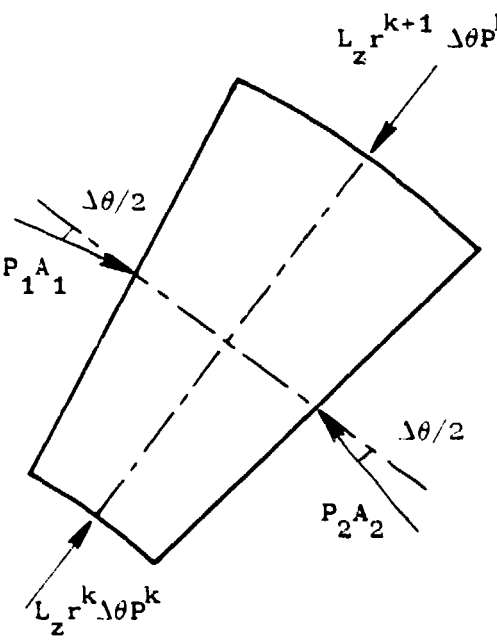

b. Pressure Forces

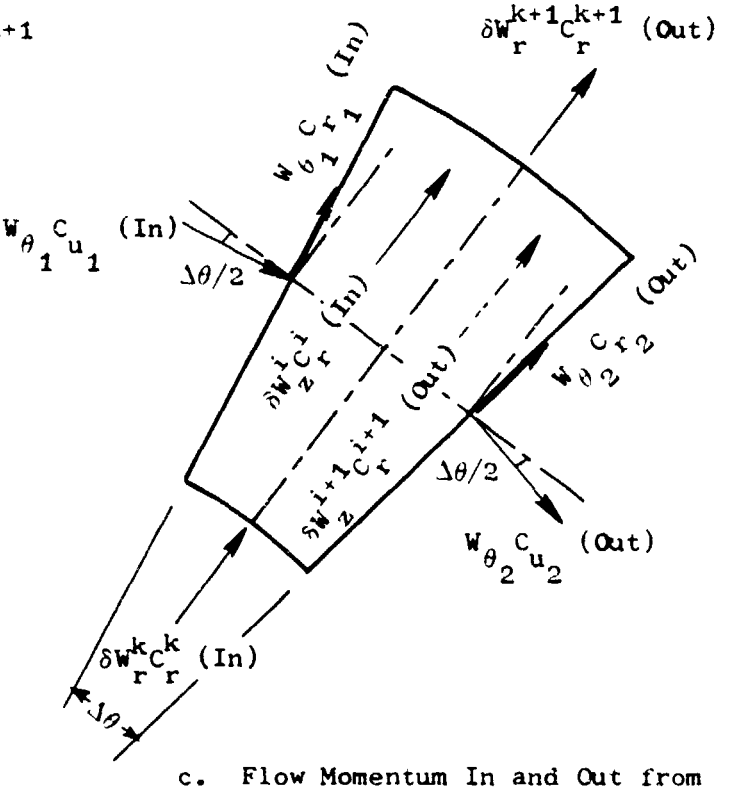

c. Flow Momentum In and Out from the Elemental Control Volume

Figure 17. Radial Momentum Balance

where Θ is the angular extent of the control volume and bars indicate volume averaged quantities. For a complete annulus control volume, Θ is equal to 2π. The two last terms represent respectively the centrifugal and the pressure forces acting on the flow passing through the control volume.

For a bladed control volume, this radial momentum equation is valid if the radial blade forces are negligible.

Energy Conservation

Energy conservation may be obtained in the same manner as the mass and momentum balances. With thermodynamic relationships it can be written in terms of an entropy balance. For a control volume with zero heat transfer to or from the fluid, the entropy balance is given by:

$$\begin{bmatrix}\text{Rate of}\\ \text{Entropy}\\ \text{Accumulation}\end{bmatrix} = \begin{bmatrix}\text{Rate of}\\ \text{Entropy}\\ \text{In}\end{bmatrix} - \begin{bmatrix}\text{Rate of}\\ \text{Entropy}\\ \text{Out}\end{bmatrix} + \begin{bmatrix}\text{Rate of}\\ \text{Entropy}\\ \text{Production}\end{bmatrix} \qquad (11)$$

Here the entropy is produced inside a control volume by any irreversible process, for example, flow undergoing total-pressure losses. Application of Equation 11 to a flow passing through the control volume shown in Figure 15 permits the following equation to be obtained.

$$\frac{\partial \overline{\rho S}}{\partial t} = \frac{1}{V}\left[W_z^i S^i - W_z^{i+1} S^{i+1} + \left\{ W_\theta^j S^j - W_\theta^{j+1} S^{j+1} \right\} + \left\{ W_r^k S^k - W_r^{k+1} S^{k+1} \right\} + S_F \right] \qquad (12)$$

Here S_F is the total entropy generated within the control volume.

The terms enclosed by braces, $\{\ \}$ in Equations 4, 8, and 12 are additions to the one-dimensional forms of the continuity, axial momentum, and energy equations given in Reference 1

4.2.2 Force, Pressure, and Entropy Production Terms

This set of equations (other than being applicable to three-dimensional flows without heat transfer), describes the state of a fluid in motion. To solve these equations, it is necessary to supply the caloric and thermal equations of state and expressions for F_Z, P_M, and S_F. F_Z of Equation 8 represents the blade force acting upon the fluid and includes contribution from the energy-producing torque term and the drag force term. P_M from Equation 8 represents the mean pressure over k and k+1 radial facing surfaces of the control volume and is calculated from a linear combination of the volume entrance and exit axial static pressures. S_F of Equation 12 is the term which represents the total rate of irreversible conversion of mechanical to internal energy and, in the case of the model, represents the entropy production due to blade row losses. Details of the derivations of these three terms may be found in Reference 1.

4.2.3 Radial Equilibrium - Two Dimensional Dynamic Model

The primary objective of the present effort is to establish a dynamic model capable of physically modelling the dynamic interactions between the fan and the compressor in a turbofan compression system. To allow for the varying bypass flow in the splitter region, radial redistribution has to be considered. A two-dimensional version of the previously derived equations can be used to dynamically analyze a turbofan compressor system, assuming that there is no circumferential redistribution of the flow. The two-dimensional governing equations with radial equilibrium are summarized below:

$$\frac{\partial \bar{\rho}}{\partial t} = \frac{1}{V}\left[(W_z^i - W_z^{i+1}) + \{ W_r^k - W_r^{k+1} \} \right] \tag{13}$$

$$\frac{\partial \bar{W}_z}{\partial t} = \frac{g_o}{L_z}\left[\frac{W_z^i C_z^i}{g_o} - \frac{W_z^{i+1} C_z^{i+1}}{g_o} + \left(\frac{W_r^k C_z^k}{g_o} - \frac{W_r^{k+1} C_z^{k+1}}{g_o} \right) + (P^i A^i - P^{i+1} A^{i+1}) - P_M (A^i - A^{i+1}) + F_z \right] \tag{14}$$

$$\frac{\partial \bar{W}_r}{\partial t} = \frac{g_o}{L_r}\left[\frac{W_r^k C_r^k}{g_o} - \frac{W_r^{k+1} C_r^{k+1}}{g_o} + \frac{W_z^i C_r^i}{g_o} - \frac{W_z^{i+1} C_r^{i+1}}{g_o} + \frac{2\pi \bar{W}_\theta \bar{C}_u}{g_o} + \pi (P^k - P^{k+1})(r^k + r^{k+1}) L_z \right] \tag{15}$$

and

$$\frac{\partial \overline{\rho S}}{\partial t} = \frac{1}{V}\left[W_z^i S^i - W_z^{i+1} S^{i+1} + \left\{ W_r^k S^k - W_r^{k+1} S^{k+1} \right\} + S_F \right] \qquad (16)$$

where $\overline{W}_\theta$ can be evaluated from

$$\overline{W}_\theta = \overline{\rho}\, \overline{C}_u L_z L_r$$

The flow in the fan duct ahead of the splitter is treated as a two-dimensional flow and is obtained by solving the above set of equations. However, core and bypass duct flows are assumed one-dimensional flows and are treated using the same set of equations after eliminating the terms enclosed by the braces { }.

Flow inside a fan rotor passage is in general a three-dimensional flow and is usually complicated by the presence of blade twist and the existence of secondary flows. Since the rotor radial blade force is not negligible and since it is difficult to consider the secondary flow effect, the model will not include radial redistribution in the rotor volume. Thus, the rotor is considered not to alter the radial distribution of the flow passing through the rotor control volume. In general, this approach is suitable and commensurate with the approach used in deriving the fan tip and hub blade characteristics where one-dimensional flow analysis is assumed.

In contrast, radial flow redistribution will be considered in the fan stator. However, it will be handled in a simplified manner. It will be assumed that only the centrifugal and the radial pressure forces acting on the flow will affect the radial distribution of the flow in the stator volume.

4.2.4 Boundary Conditions

Four boundary conditions are necessary and sufficient to obtain the solution of the set of first order equations given by Equations 13 through 16. Three of these conditions will define three flow properties at the inlet station, while the last condition will define a property or a relation of properties at the exit station.

At the compression system inlet, the air flows axially and therefore at the inlet the radial velocity component is zero. Inlet total pressure and total temperature are specified and held constant. With these inlet conditions and together with the density value, obtained from the first volume averaged density, all the other inlet flow properties can be calculated.

In a turbofan compression system, the flow entering the system branches into two flows, a core flow and a bypass flow. Hence, exit boundary conditions have to be specified for each flow. At each exit, one boundary condition is necessary and sufficient. Usually, it is either the exit static pressure (P_s) or the exit flow function ($W\sqrt{T_s}/P_s$). The choice depends on whether the flow exits to a uniform static pressure such as through a fan bypass flow duct nozzle or to a choked flow such as a turbine nozzle. In the latter case specification of the exit flow function is a good simulation.

4.3 CALCULATION TECHNIQUE

The following subsections will outline the method of solution adopted to solve the governing equations, the computational steps performed to obtain the flow variables of the entire compression system and finally the process followed to obtain the initial, the time relaxed steady-state, and the time dependent solutions.

4.3.1 Method of Solution

The explicit second order time marching technique developed in Reference 1, is used to solve Equations 13 through 16. The technique is based on a Taylor series expansion of the volume averaged flow properties at time "t" to predict the flow properties at time "$t + \Delta t$". If $\bar{X}$ represents a volume averaged flow property, then the second order Taylor series can be written as.

$$\bar{X}\ (t+\Delta t) = \bar{X}\ (t) + \frac{\partial \bar{X}\ (t)}{\partial t}\ \Delta t + \frac{\partial \bar{X}(t)}{\partial t^2}\ \frac{\Delta t^2}{2} \qquad (17)$$

This equation indicates that both first and second time derivatives of the flow properties are needed. First derivatives are evaluated directly from Equations 13 through 16; however, the second order derivatives are evaluated by differentiating the same set of equations with respect to time.

4.3.2 Computational Procedure

The present model of radial redistribution was developed as an extension of and is quite similar to the Dynamic Digital Blade-Row Compression Component Stability Model discussed in Reference 1. Figure 18 illustrates the computational procedure in a block diagram format.

Block 1 is a statement of the required dependent variable information, that is, volume-averaged density, axial flow, radial flow, and entropy which

are available from either an initial guess, a steady-state solution, or the solution known from a previous time step of a time dependent analysis. From the volume averaged axial and radial flows, and with the proper interpolation scheme for station flow values of W_r and W_z, the time derivative of the volume averaged density can be obtained for all the volumes, as indicated in Block II.

In order to calculate the first time derivatives of the other variables, station values of all the variables have to be known. Block III of Figure 18 illustrates the interpolation between the volume-averaged properties in order to obtain station-value properties.

In the case of blade-free volumes, where no blade forces or entropy production takes place, it is only necessary to calculate station velocity components in order to evaluate the equations of change. As shown in the lower branch of Block IV, the assumption of constant absolute flow angle across the volume is made. Total pressure, total temperature, and other desirable parameters are also calculated as this point. A special case of the blade free-volume calculations is the imposition of the boundary conditions. At the model inlet, zero radial flow, constant total pressure and total temperature as well as constant entropy are maintained. At the exit of a model of a turbofan compression system, either a specified flow function or a specified static pressure boundary condition is imposed. Change of the core flow function or the bypass duct exit static pressure with respect to time will in fact represent a simulation of the compressor or the fan throttling process, respectively.

As indicated in the upper branch of Block IV, the presence of a bladed volume requires the net axial blade force, entropy production, and station velocity components to be calculated. Calculation of the net axial force and entropy production terms require knowledge of the loss coefficient and deviation angle. This information is available as polynomial representations which are functions of incidence angle. Stationary blade rows are assumed to be lossless with constant deviation angle.

Once the flow conditions at the stations are completely described, various quantities of interest can be calculated such as stage coefficients, diffusion factors, etc. With all the necessary quantities on the right-hand side of the macrobalances available, the first-time derivatives of the volume averaged properties can be calculated as indicated in Block V.

After the procedure in Blocks III, IV, and V is carried out for the tip and hub volumes, as indicated by Block VI, the second time derivatives of the properties can be calculated (Block VII). Expressions for the second time derivatives of the volume averaged quantities are obtained from

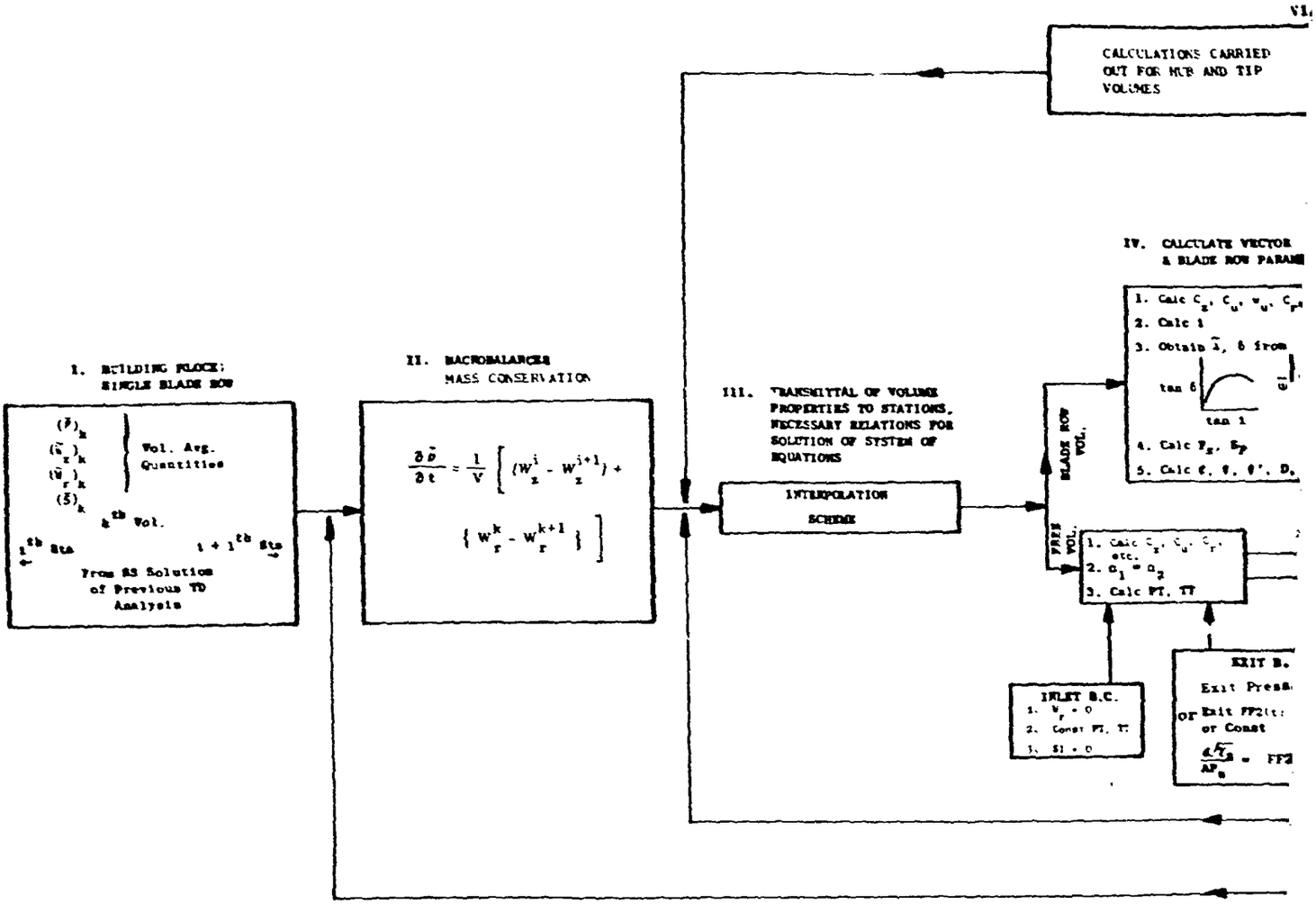

FOLDOUT FRAME

Figure 18. Dynamic Model B

PRECEDING PAGE BLANK NOT FILMED

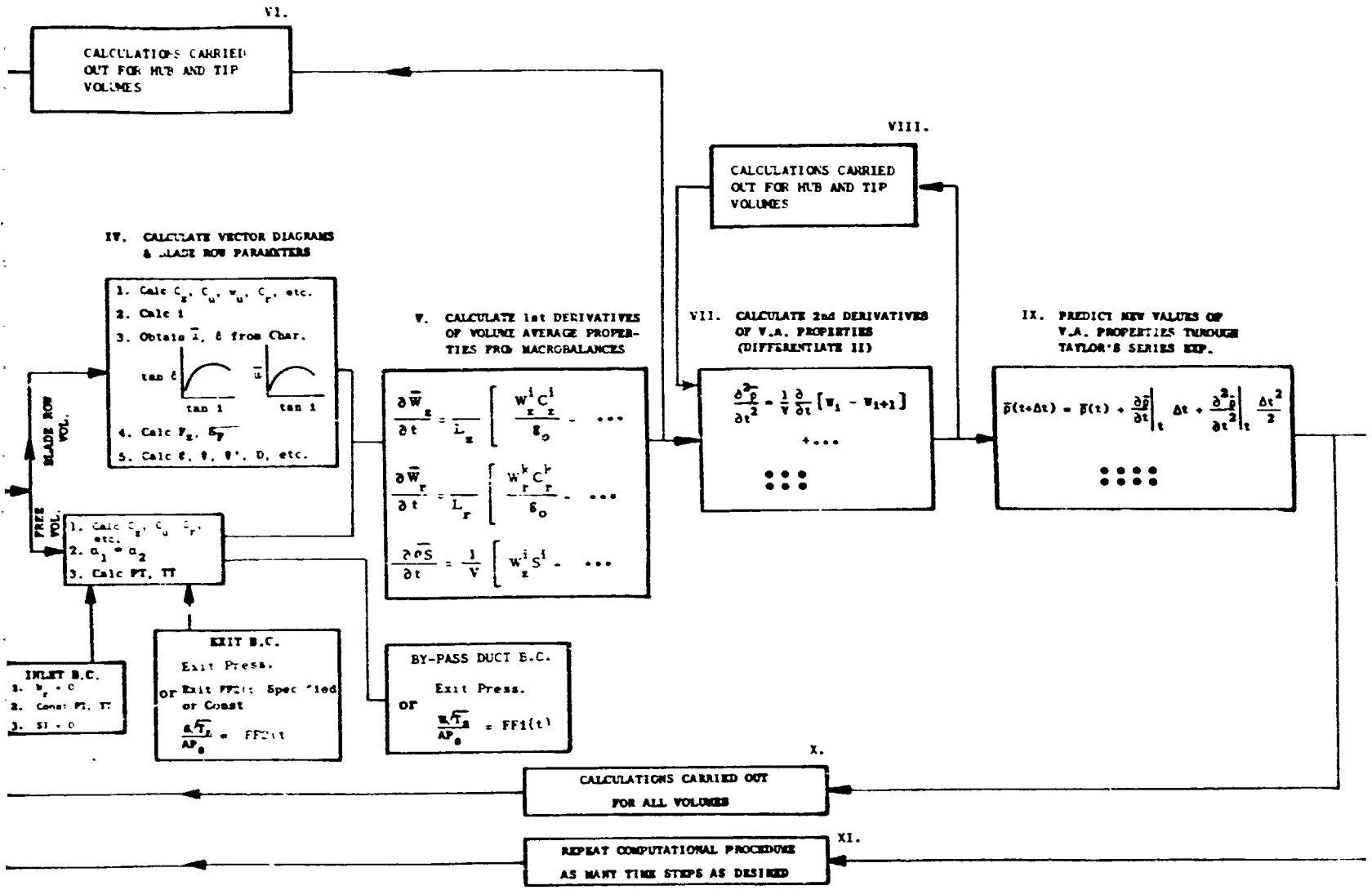

FOLDOUT FRAME

8. Dynamic Model Block Diagram.

differentiating the macrobalances with respect to time. Analytical expressions for the time derivatives of the station properties can be evaluated by interpolating between volumes and through use of the macrobalances. The same calculations are carried out for both hub and tip volumes (Block VIII).

The procedure for calculating station properties and evaluating first and second time derivatives of the volume-averaged properties can be carried out for any number and types of volumes (Block X) and is not dependent on the particular geometry being modelled. Once these calculations are carried out for all the volumes, the solution can be advanced to the next time step through use of the second-order Taylor's series approximation, Block IX. As specified in Block XI, the technique can be repeated for as many time steps as required by the event being simulated.

4.3.3 Initial, Steady-State, and Time Dependent Dynamic Solutions

A prime interest of this study is to determine the turbofan compression system operation under both steady-state and time varying conditions. The solution procedure adopted to achieve this goal and outlined in the previous section requires the knowledge of an initial distribution of the flow properties along the compression system. This distribution can be obtained by solving the one-dimensional version of governing equations (Equations 13, 14, and 16) with the left-hand-side time derivative set to zero, and with an assumed value of the bypass ratio. During these calculations radial flow across the splitting surface is not permitted. The use of the same governing equations to develop initial conditions to the system is adopted to assure consistency between the initial conditions and the subsequent calculations. The initialization is achieved in a separate subroutine that was added to the main computer program.

Since the assumed splitting stream surface ahead of the bypass splitter does not represent in reality the actual stagnation stream surface which separates the core and the bypass flows, the initial steady-state solution obtained in the first phase of the calculations does not represent the actual steady-state solution of the flow in the compression system. A time relaxation technique is followed to obtain the actual steady-state solution. The initial solution is relaxed in time while keeping the inlet and exit boundary conditions constant and allowing radial flow exchange between flows in the hub and tip regions of the fan duct. The equations used in this phase of the calculations are the two-dimensional time-dependent governing equations (Equations 13 through 16). The solution is assumed to have converged to the steady-state solution when the change in the axial flow rate at any volume from one time step to the next is less than 0.0001 percent.

Time-dependent solutions of dynamic operations are obtained by perturbing the system from the steady-state operation case. Again, the two-dimensional time-dependent equations are solved using the calculation procedures of the previous section. Time-varying inlet or exit boundary conditions are included during this phase of calculations. The response of the system as a function of time can be achieved from the results of these calculations. It should be kept in mind that the bypass-ratio is never specified, but results from the radial redistribution that occurs at any moment.

The throttling process of a compression system is a typical dynamic operation where the flow through the system changes through variation of the exit area. If the rate of throttling along a speed line is extremely slow, the system will follow very closely the steady-state speed lines.

4.4 Clean Inlet Flow Steady-State and Throttling Simulations

The two-dimensional time-dependent model established in Sections 4.2 and 4.3 was used to determine the clean inlet steady-state flow and the clean inlet flow stability limit of the compression system of the TF34 turbofan engine. The steady-state solution, satisfying the radial equilibrium of the flow in the fan duct, was obtained using the time relaxation method. Throttling simulation was then conducted by throttling the fan bypass duct along two different fan speed lines and the core along two different core speed lines. Fan tip, fan hub, and compressor blade characteristics used for these computations are the same as those used for the component stability predictions of Section 3.

The core/fan speed relationship used in this study was obtained from the steady-state performance cycle deck data. This relationship is presented in Figure 19. The relation implies that the fan corrected speed is dependent only on the core corrected speed; however, the data obtained from the cycle deck indicated a slight variation in the fan speed with the fan bypass exit area. This variation is less than $\pm$ 1% and thus, is neglected in the present model.

The size of the time step has to be determined prior to the numerical solution of the time-dependent equations. A time step of 10^{-5} seconds was chosen for the present computations. This value satisfied the CFL (Courant, Friedrichs, and Lewy) stability condition and, therefore, it assures the numerical stability of the present explicit scheme. Also, it was found that this time step size is small enough to assure quasi-steady throttling during the system stability studies.

From the model computations, the bypass ratio that satisfies the flow radial equilibrium in the fan duct ahead of the bypass splitter will be deter-

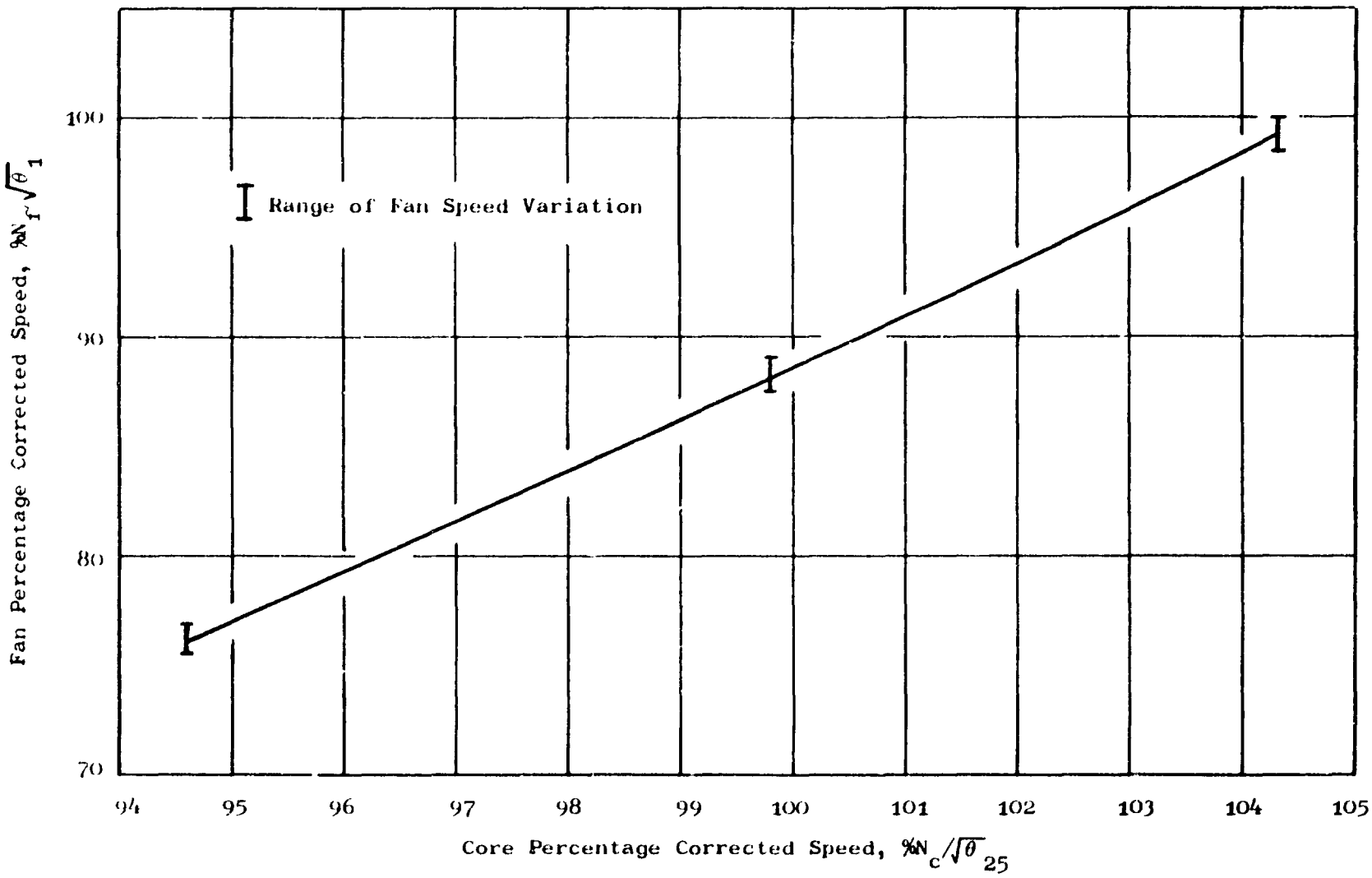

Figure 19. TF-34 Fan Speed/Core Speed Relationship.

mined. The validation of the model will be based on the comparison of the bypass ratio with the steady-state value obtained from the cycle deck data.

The results that will be presented in the following paragraphs are given for some of the fan duct volumes. Figure 20 illustrates the nomenclature used for the volumes and the axial stations of the fan duct. Blade-free volumes are indicated by the capital letter "F", while the fan rotor and stator are indicated by the capital letters "R" and "S", respectively. The axial stations are denoted by the numbers 1 to 13; 1 to 5 for the duct upstream of the fan rotor, 6 to 9 for the interaxial gap between the rotor and the stator, and 10 to 13 for the duct behind the fan and ahead of the bypass splitter.

4.4.1 Clean Inlet Steady-State Flow

Time-relaxed steady-state calculations were conducted for two cases. The data for the first case are 104.3% core corrected speed, 99.1% fan corrected speed, 136.08 Kg/sec (300 lb/sec) inlet mass flow rate, and an initially assumed value of 5.302 for the flow bypass ratio. The data for the second case are 99.8% core corrected speed, 88.3% fan corrected speed, 116.35 Kg/sec (256.5 lb/sec) inlet mass flow rate, and an initially assumed flow bypass ratio of 5.316. For these cases, the initial value of the flow bypass ratio was obtained from the cycle deck data.

The steady-state solution was obtained by relaxing in time the initial flow distribution until radial equilibrium was achieved. Convergence was assumed when the variation of the volume averaged axial flow rate between two consecutive time steps was less than 0.0001 percent for each volume. Figures 21 through 30 show the flow variable changes during the relaxation process.

Figures 21 and 22 represent the relaxation of the fan hub and tip volume-averaged axial flow rates as functions of time. These results are for 99.1% fan corrected speed and similar results for 88.3% fan corrected speed are shown in Figures 23 and 24. It should be mentioned that the calculated results are plotted at intervals of 400 time steps. By examining these results, the convergence of solution occurs after approximately 4000 time steps. All the volumes of the hub region, initially started with the same volume-averaged axial flow rates, but after convergence they ended up with different axial flow rates. The same is true for the tip volumes although the hub and tip axial flow rates are different. This is due to the fact that the assumed stream-surface, that separates the flow in the fan hub and tip regions of the fan, does not coincide with the actual stream-surface that separates the core and bypass flows.

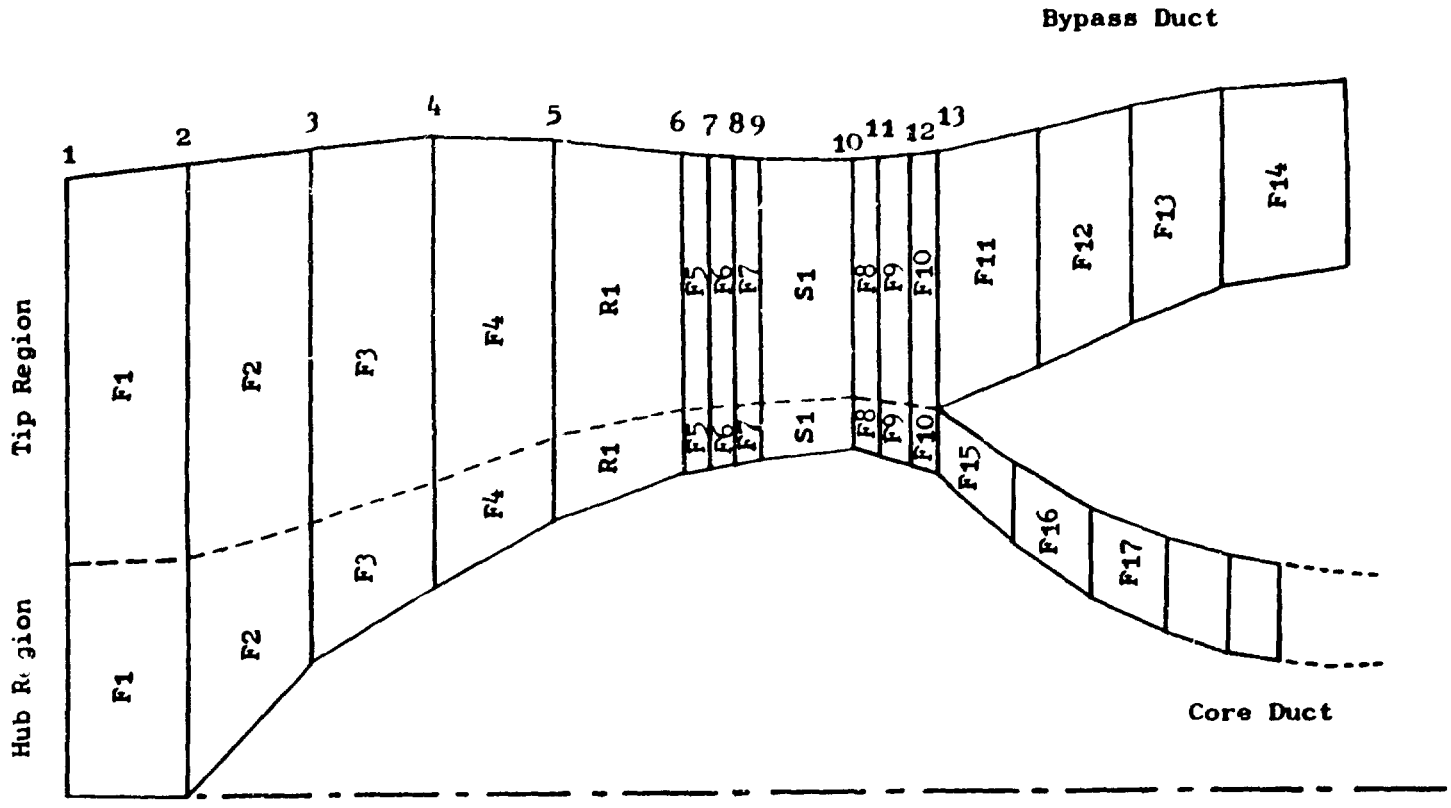

Figure 20. Stations and Volumes Nomencla ire.

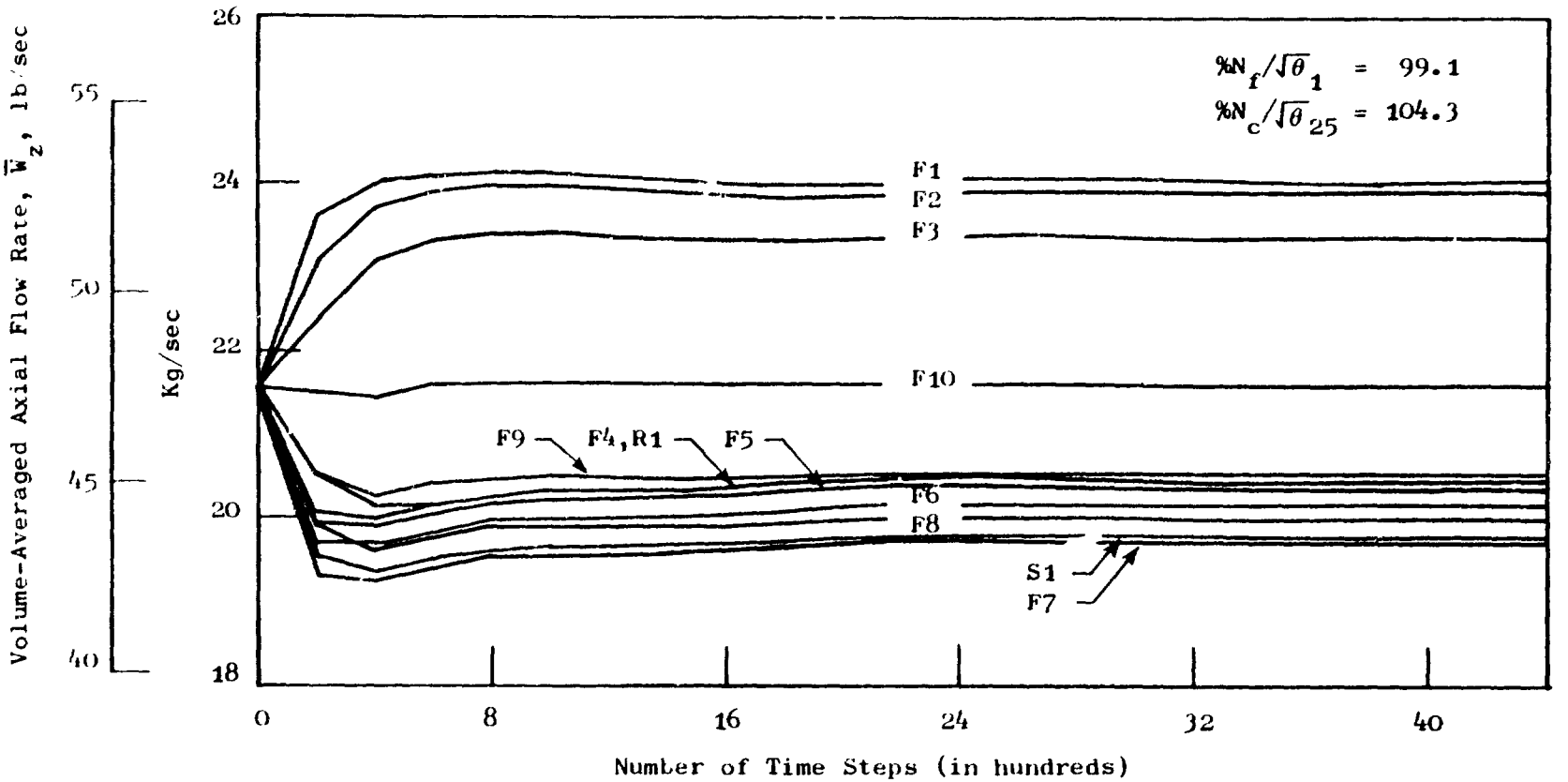

Figure 21. Relaxation of Volume-Averaged Axial Flow Rate as Function of Time (Fan Hub Region).

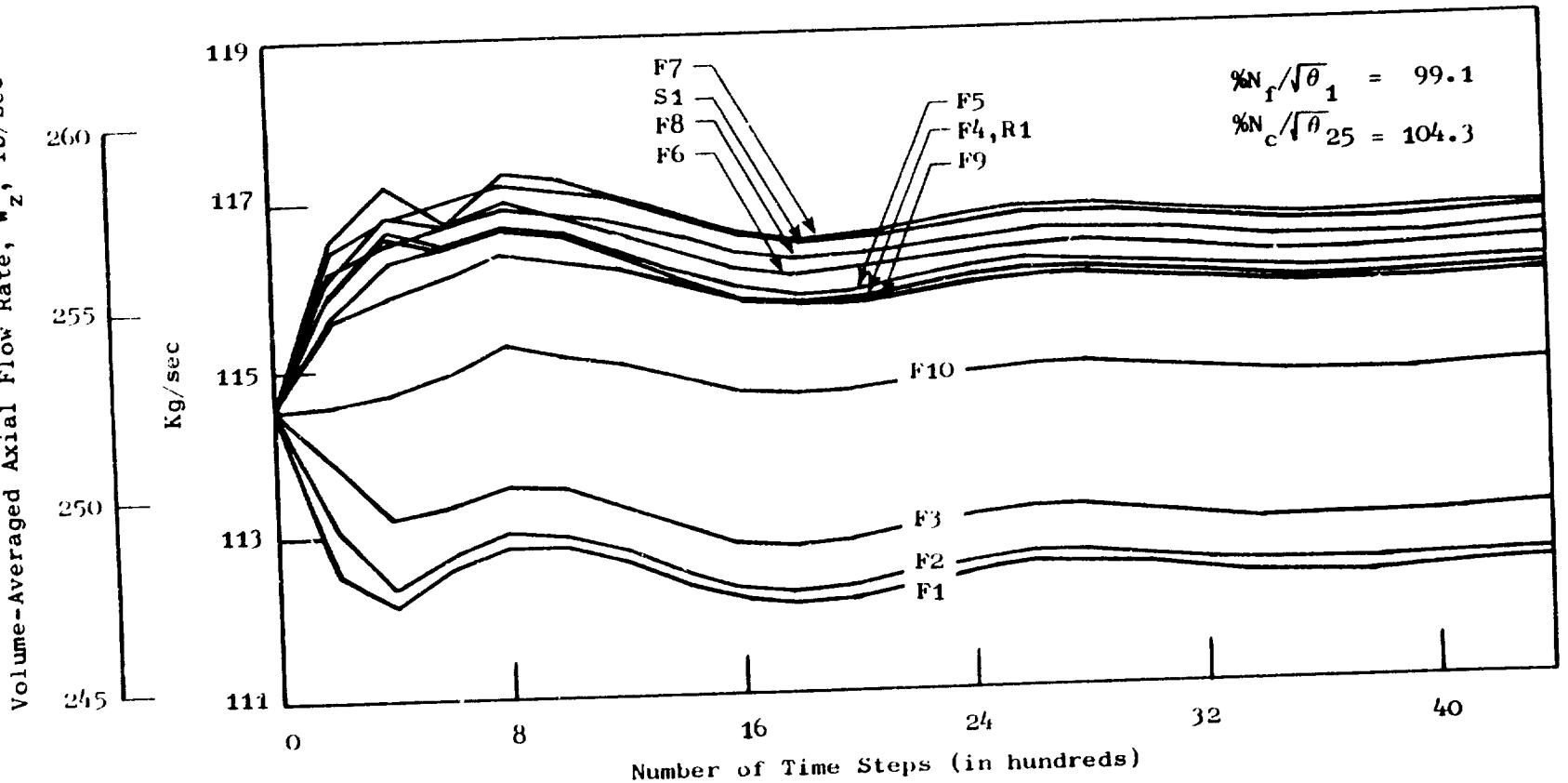

Figure 22. Relaxation of Volume-Averaged Axial Flow Rate as Function of Time (Fan Tip Region).

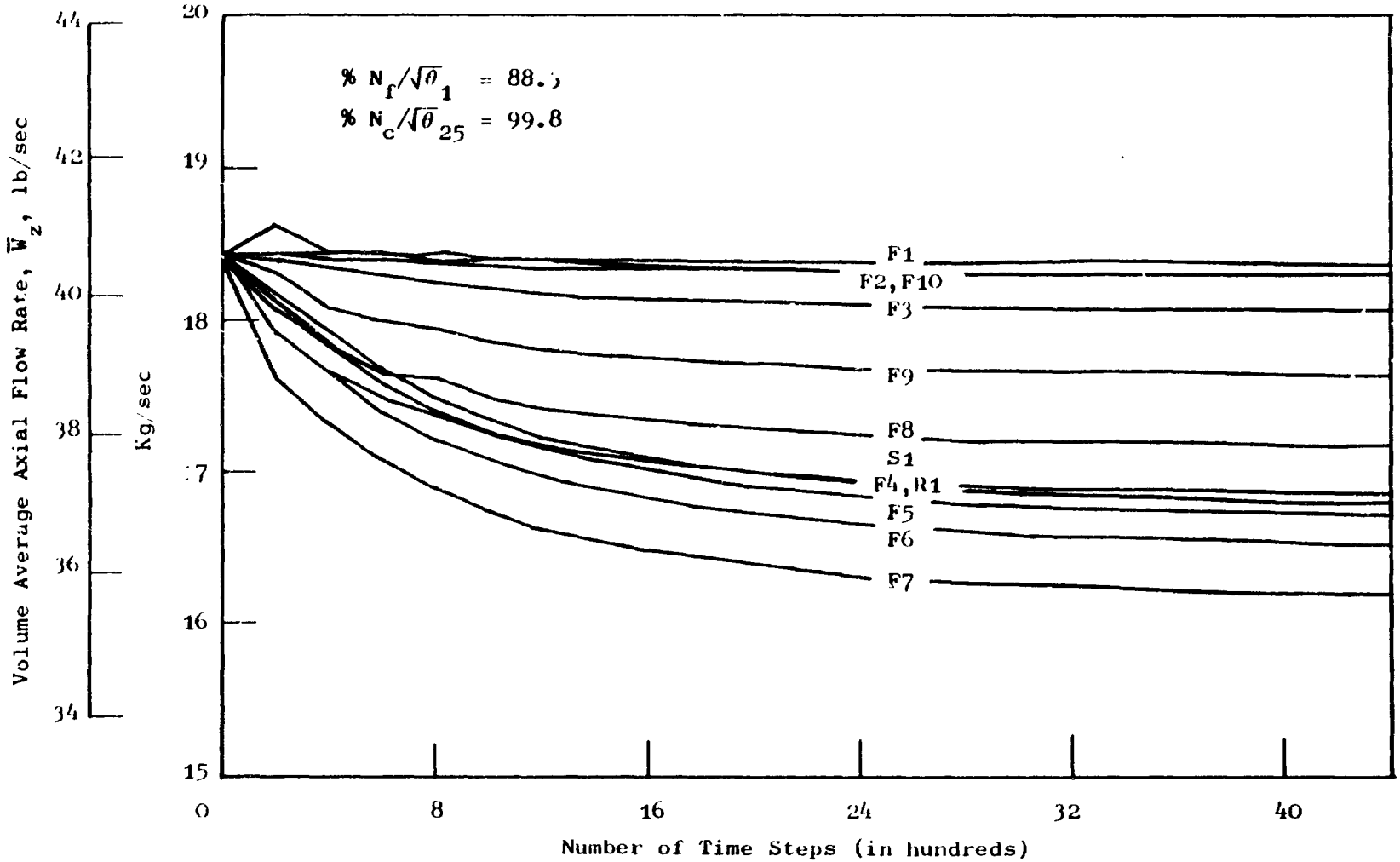

Figure 23. Relaxation of Volume-Averaged Axial Flow Rate as Function of Time (Fan Hub Region).

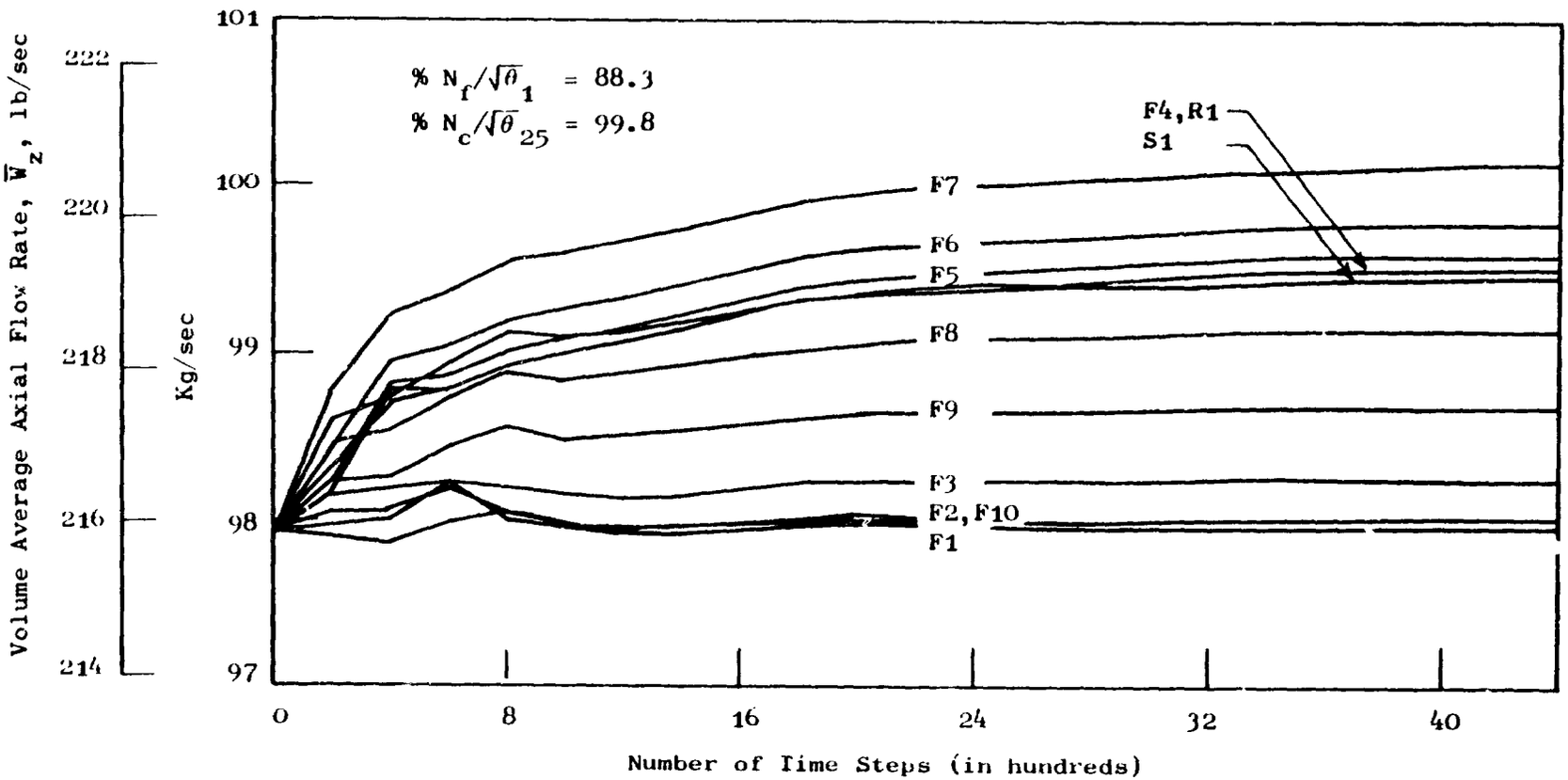

Figure 24. Relaxation of Volume-Averaged Axial Flow Rate as Function of Time (Fan Tip Region).

The time relaxation of the hub-to-tip radial flow for the different fan volumes is shown in Figures 25 and 26. Positive values indicate radial flow across the split stream-surace from the hub to the tip region and vice versa, negative values indicate radial flow from the tip to the hub region. The results show that the flow adjusts itself both behind and ahead of the fan during the relaxation process. The large radial flow rate value for volume F4 in comparison with that for volume F10 should not be misjudged. Actually, if the difference in the axial lengths between the two volumes is considered, it is found that the radial flow flux (flow rate per unit area) at volume F10, ahead of the bypass splitter, is larger than that at volume F4, ahead of the rotor.

The time relaxation of static pressure at the stator inlet and at the splitter leading edge are shown in Figures 27 through 30. Tip and hub average pressure values are presented for both 99.1% and 88.3% fan corrected speeds. It is clear that the steady-state pressure levels in all cases were achieved in less than 20 milliseconds. After that time very small adjustments in the pressures are needed to allow other flow variables to adjust to their steady-state values.

The difference between the hub and tip averaged pressures indicate the level of the radial force acting on the fluid due to the radial pressure gradient. During the steady-state time relaxation, the radial force changes until radial equilibrium is achieved thereafter it maintains a constant level.

Figures 31 and 32 show the distribution of the volume averaged axial flow rate at 99.1% fan corrected speed for the hub and tip regions, respectively. Figures 33 and 34 show similar plots for the 88.3% fan corrected speed case. The distributions of the axial flow rate are given as a function of time and their shape depends largely on the geometry of the split stream-surface.

The distribution of the radial flow rate at 99.1% and 88.3% fan corrected speeds are shown in Figures 35 and 36, respectively. The results indicate radial flow ahead as well as behind the fan rotor.

Figure 37 shows the distribution of the hub and tip average static pressure at 99.1% fan corrected speed. Both the initial and the steady-state values are given.

4.4.2 Fan Bypass Duct Flow Throttling

Clean inlet bypass duct quasi-static throttling was conducted for 99.1% and 88.3% fan corrected speeds. Figures 38 and 39 show the throttling locii on the performance maps for the fan tip and hub, respectively. The hub and

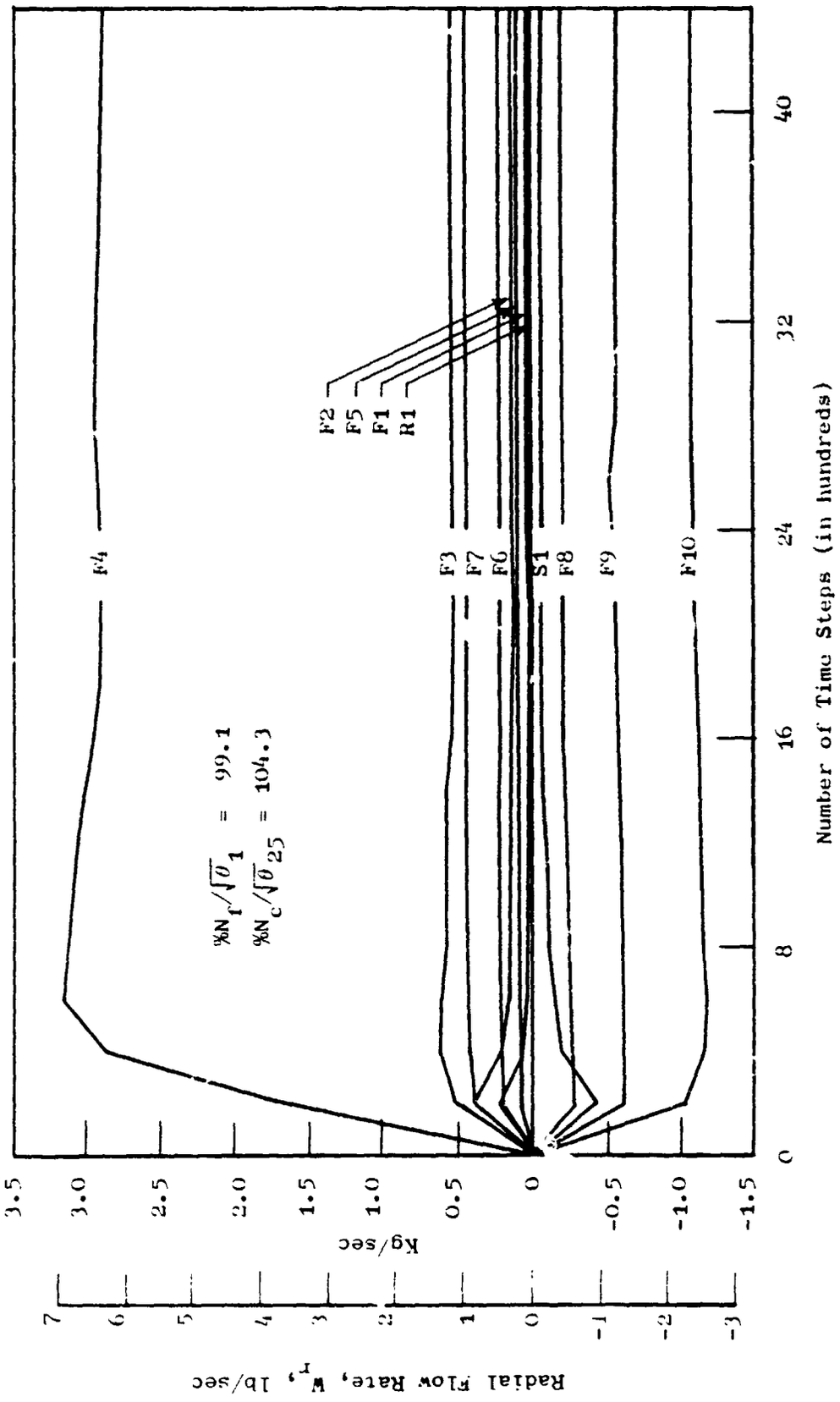

Figure 25. Relaxation of Hub to Tip Radial Flow Rate as Function of Time.

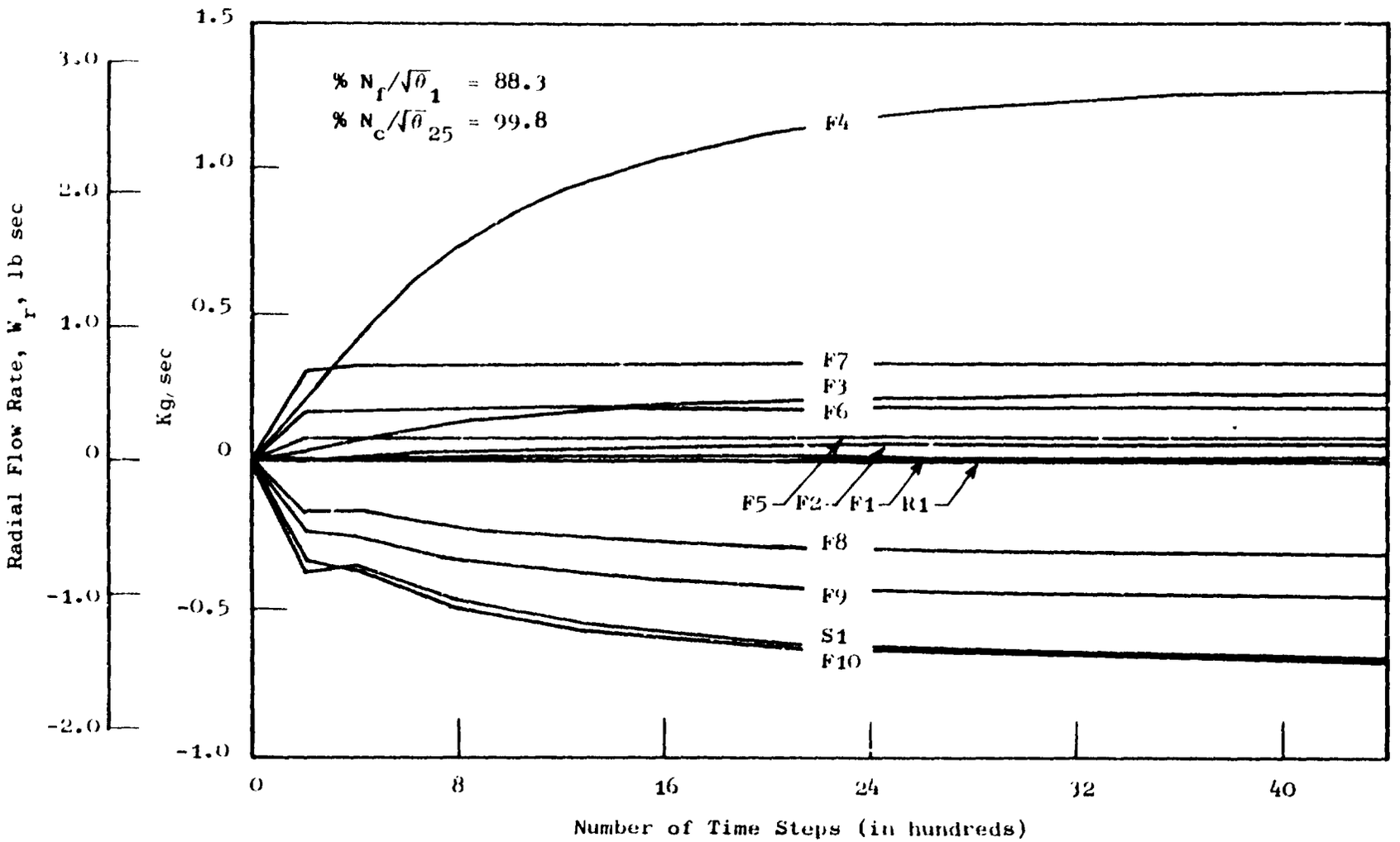

Figure 26. Relaxation of Hub to Tip Radial Flow Rate as Function of Time.

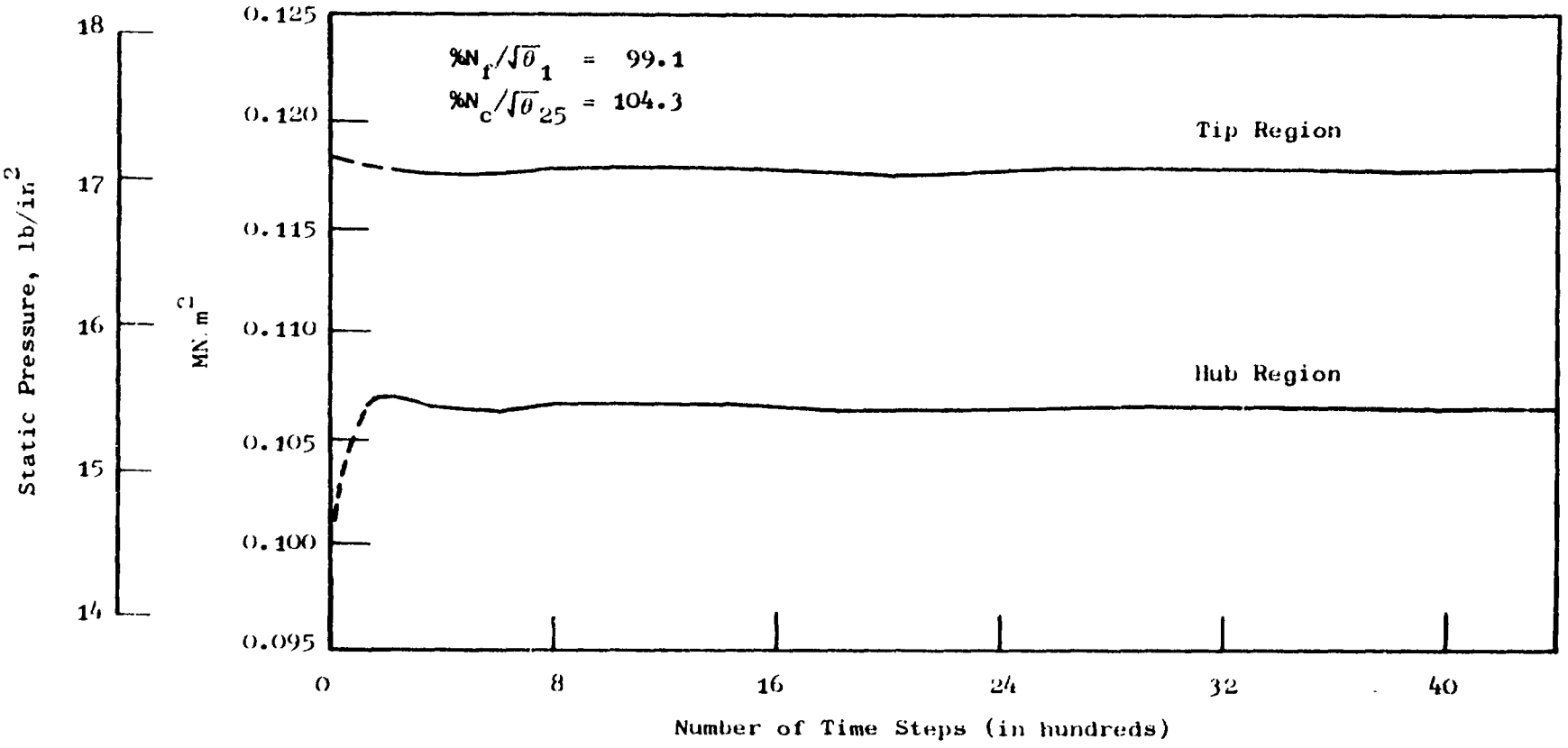

Figure 27. Average Static Pressure at Stator Inlet Plane.

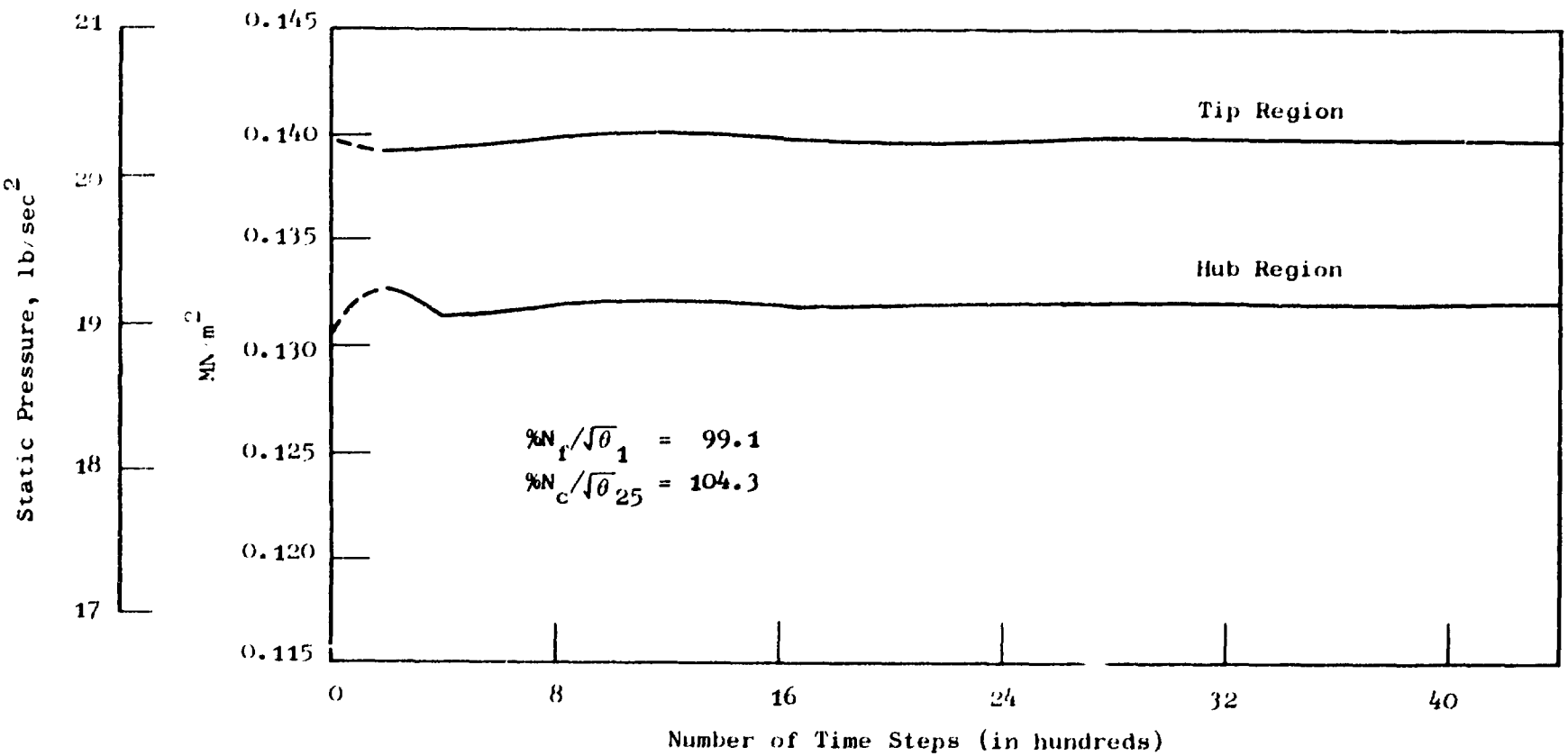

Figure 28. Average Static Pressure at Splitter Leading Edge Plane.

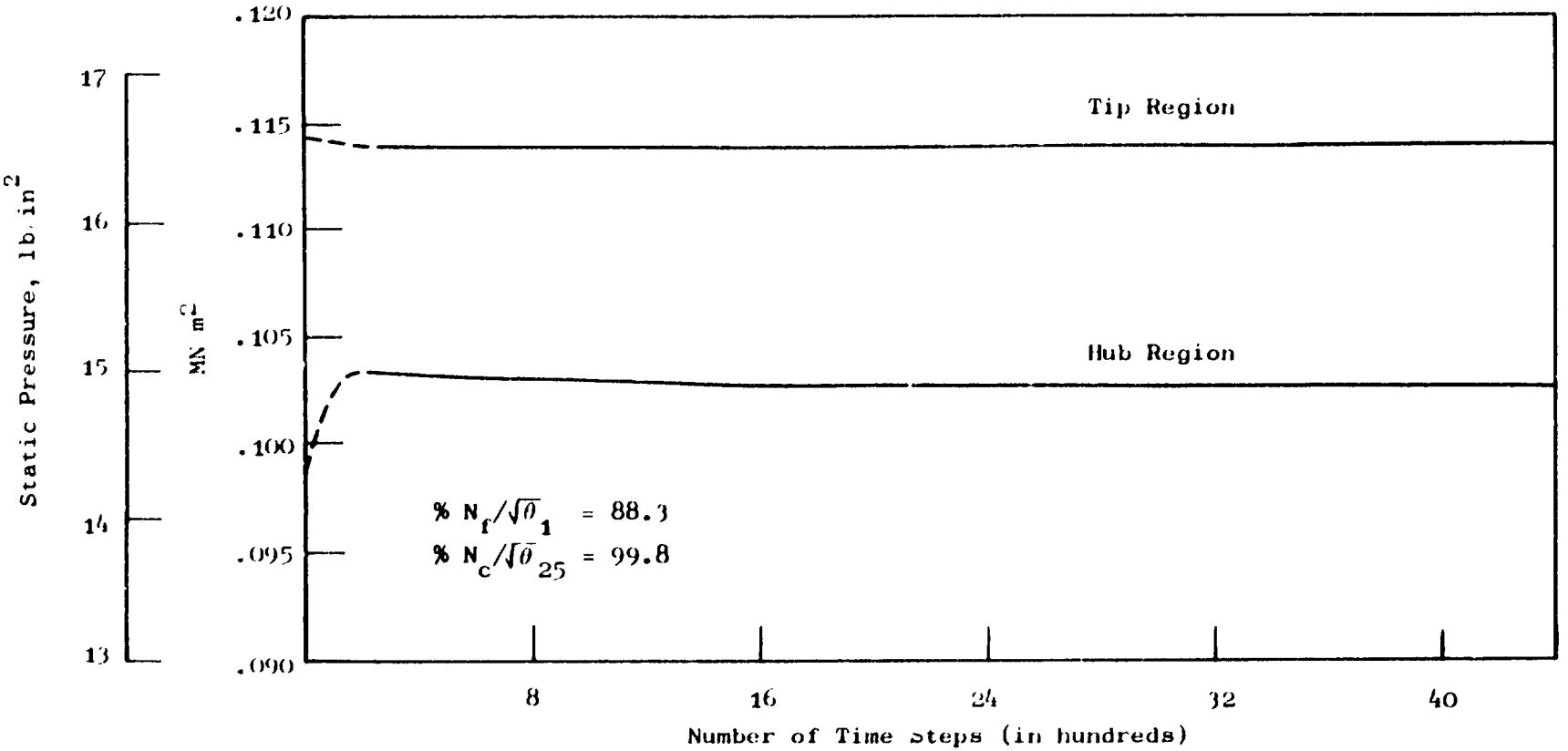

Figure 29. Average Static Pressure at Stator Inlet Plane.

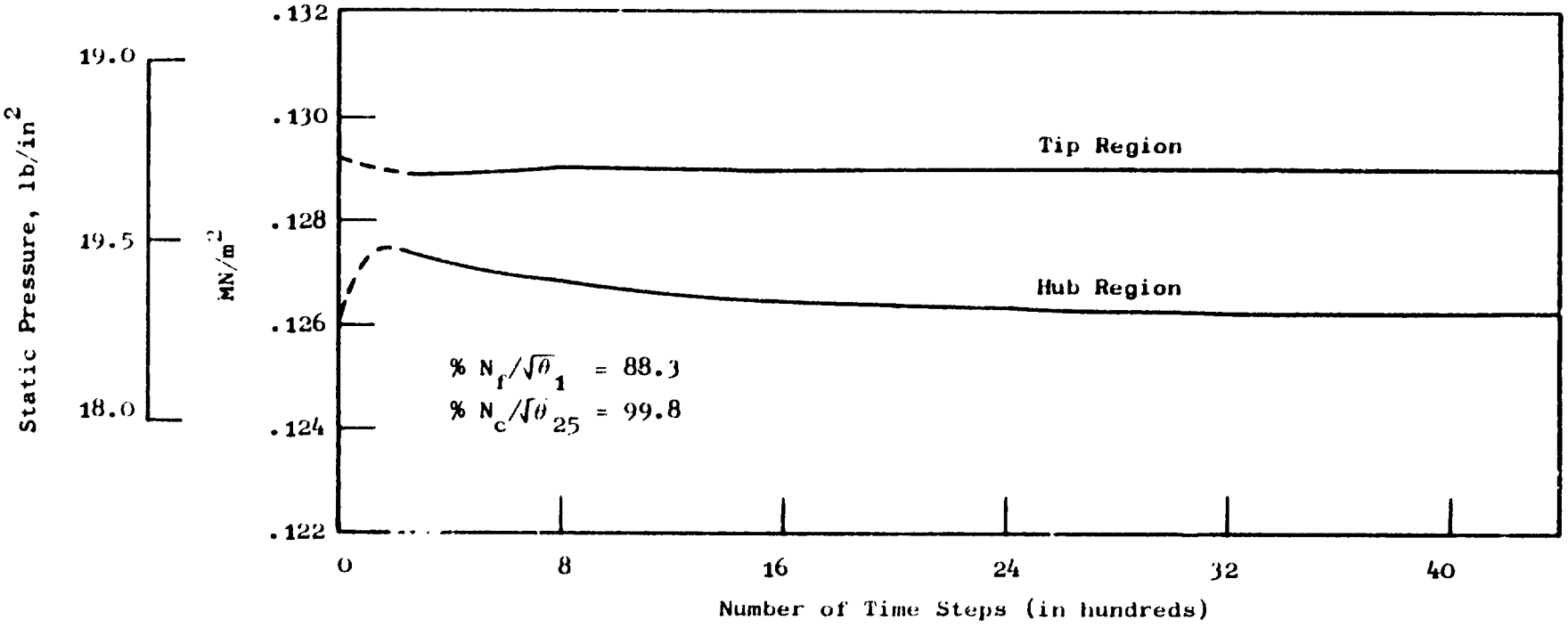

Figure 30. Average Static Pressure at Splitter Leading Edge Plane.

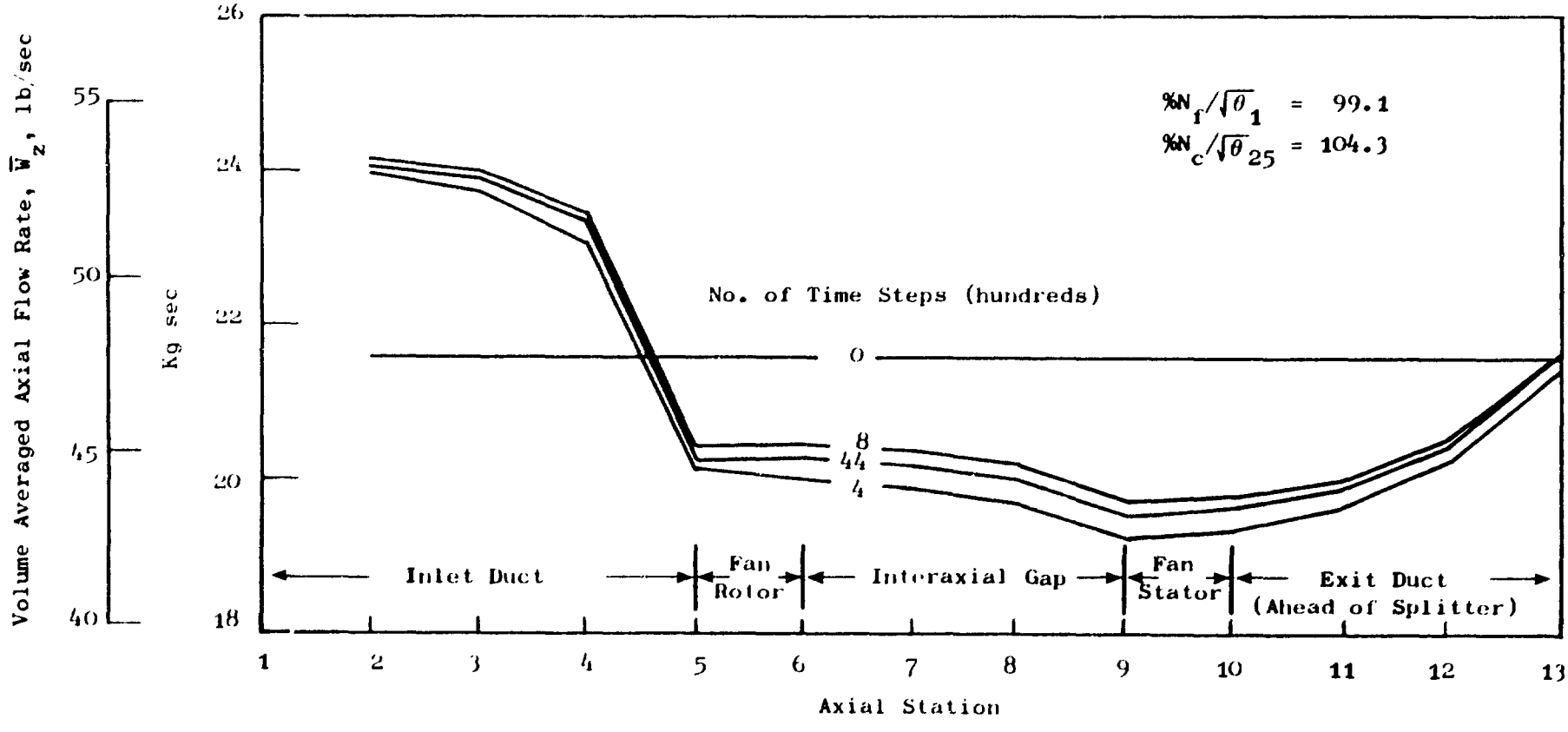

Figure 31. Distribution of Volume-Averaged Axial Flow Rate along the Fan Hub Region.

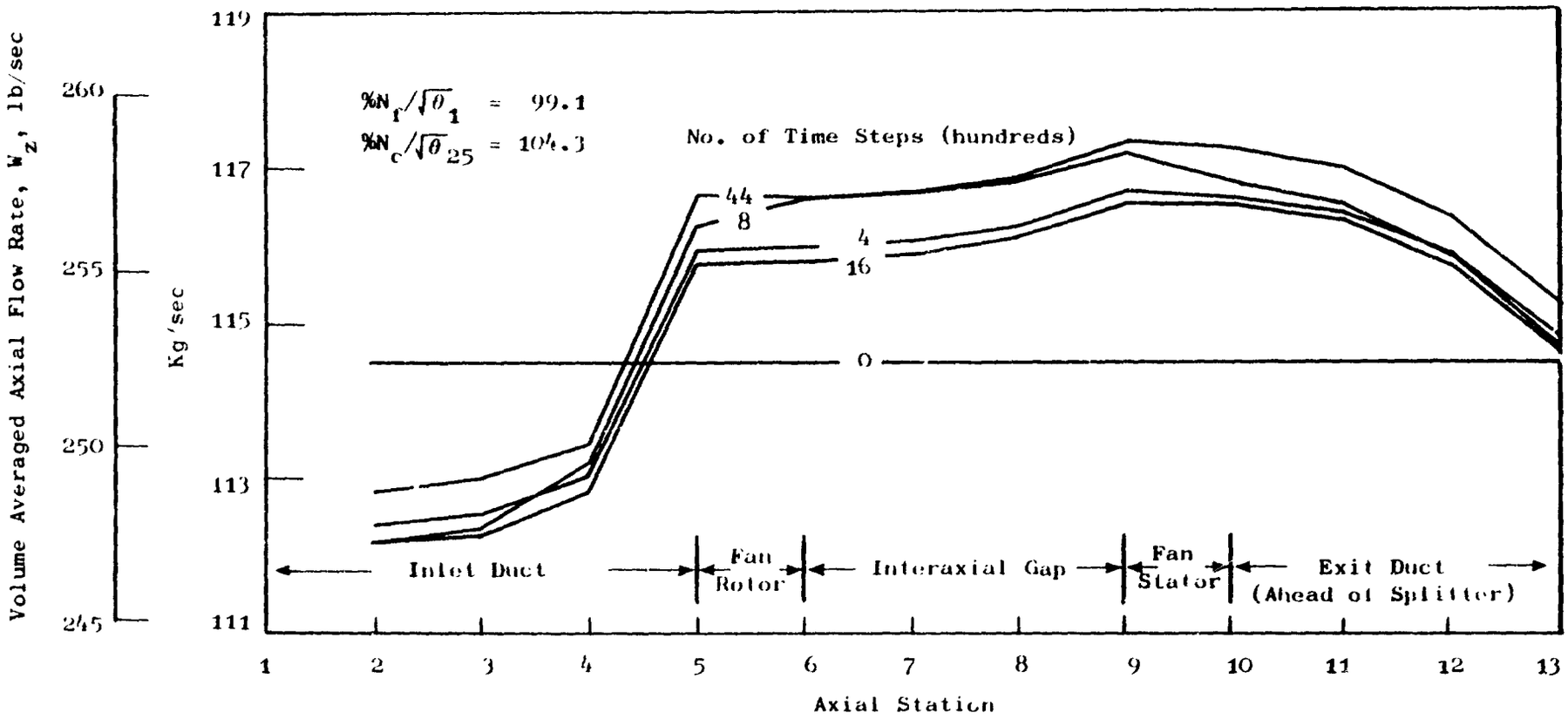

Figure 32. Distribution of Volume Averaged Axial Flow Rate along the Fan Tip Region.

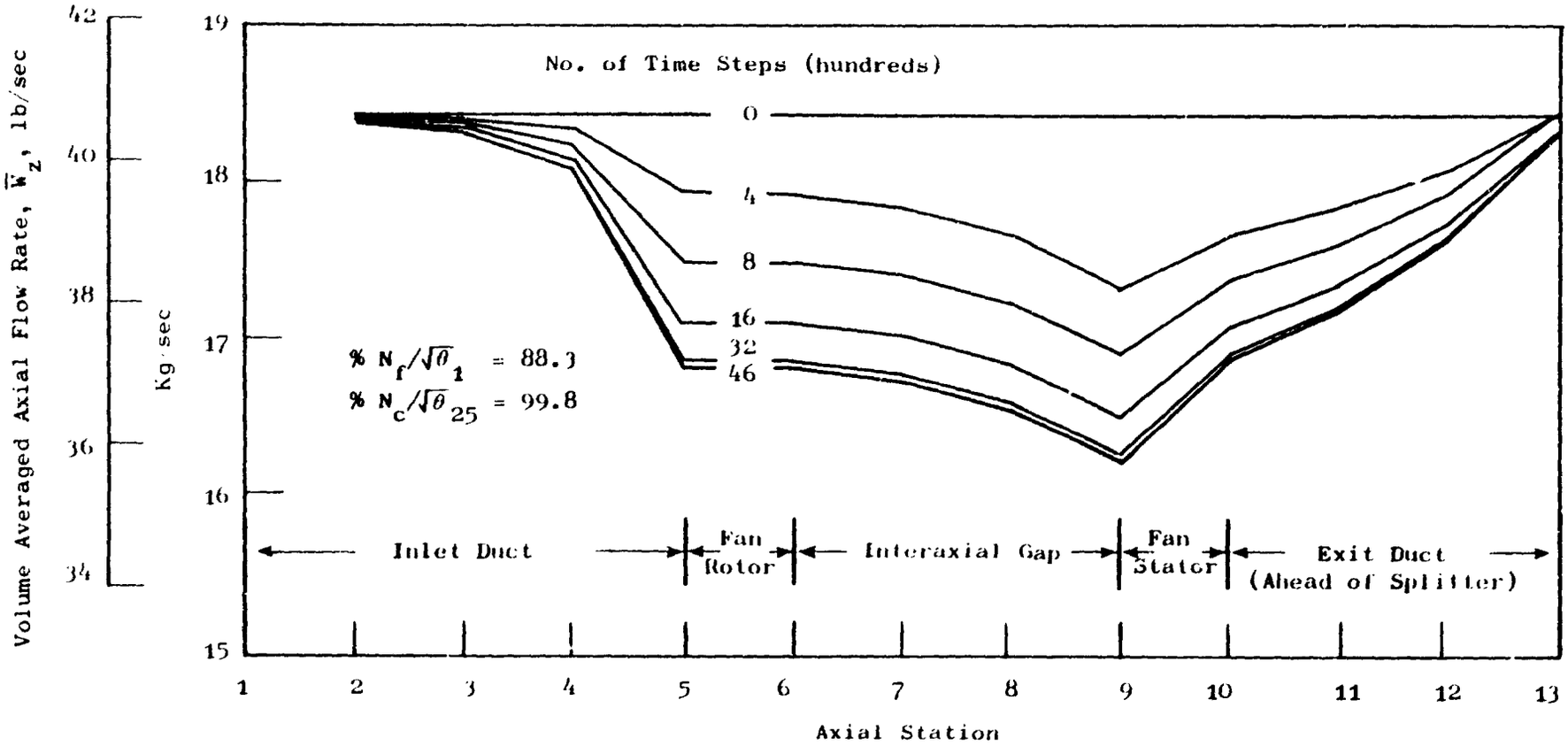

Figure 33. Distribution of Volume-Averaged Axial Flow Rate along the Fan Hub Region.

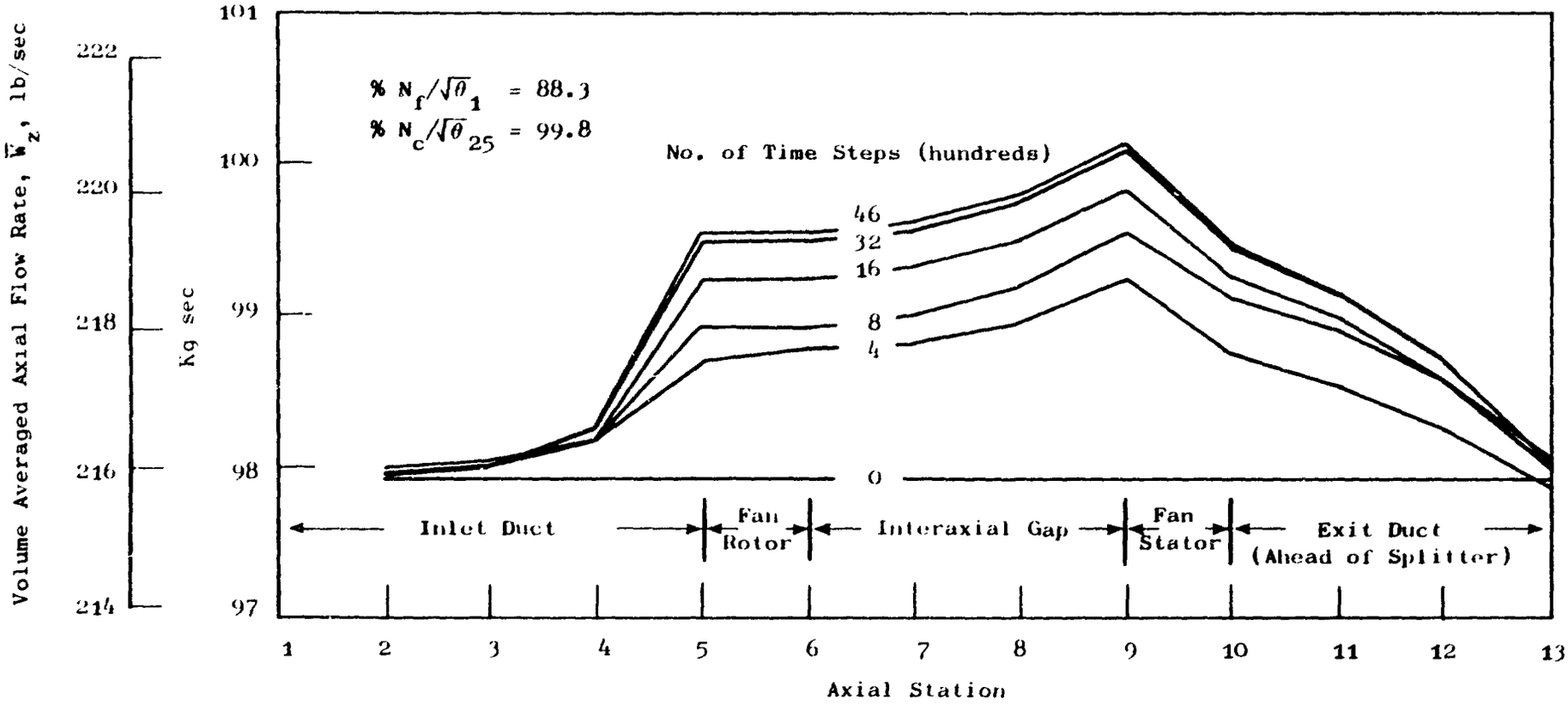

Figure 34. Distribution of Volume-Averaged Axial Flow Rate along the Fan Tip Region.

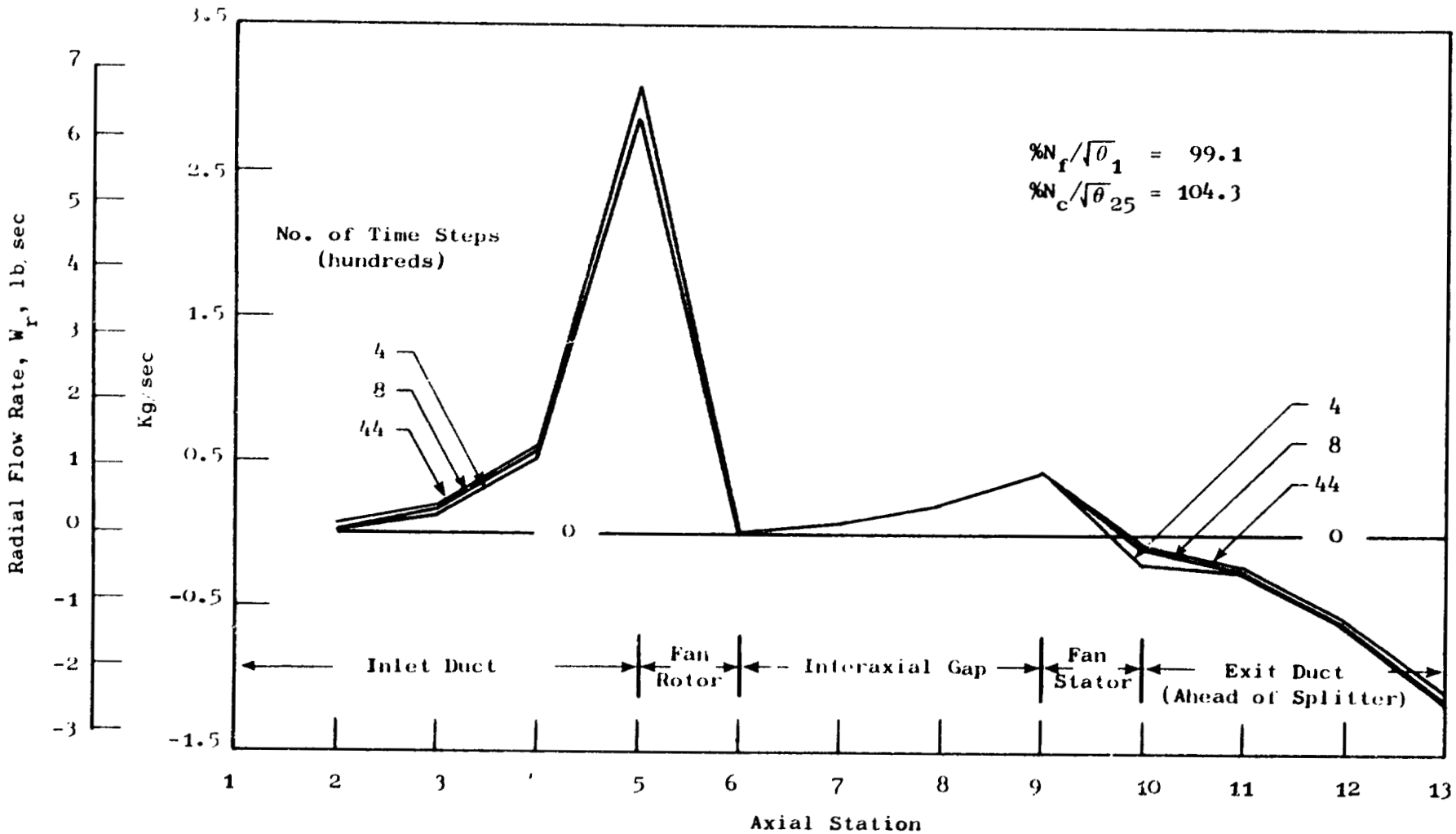

Figure 35. Distribution of Hub to Tip Radial Flow Rate.

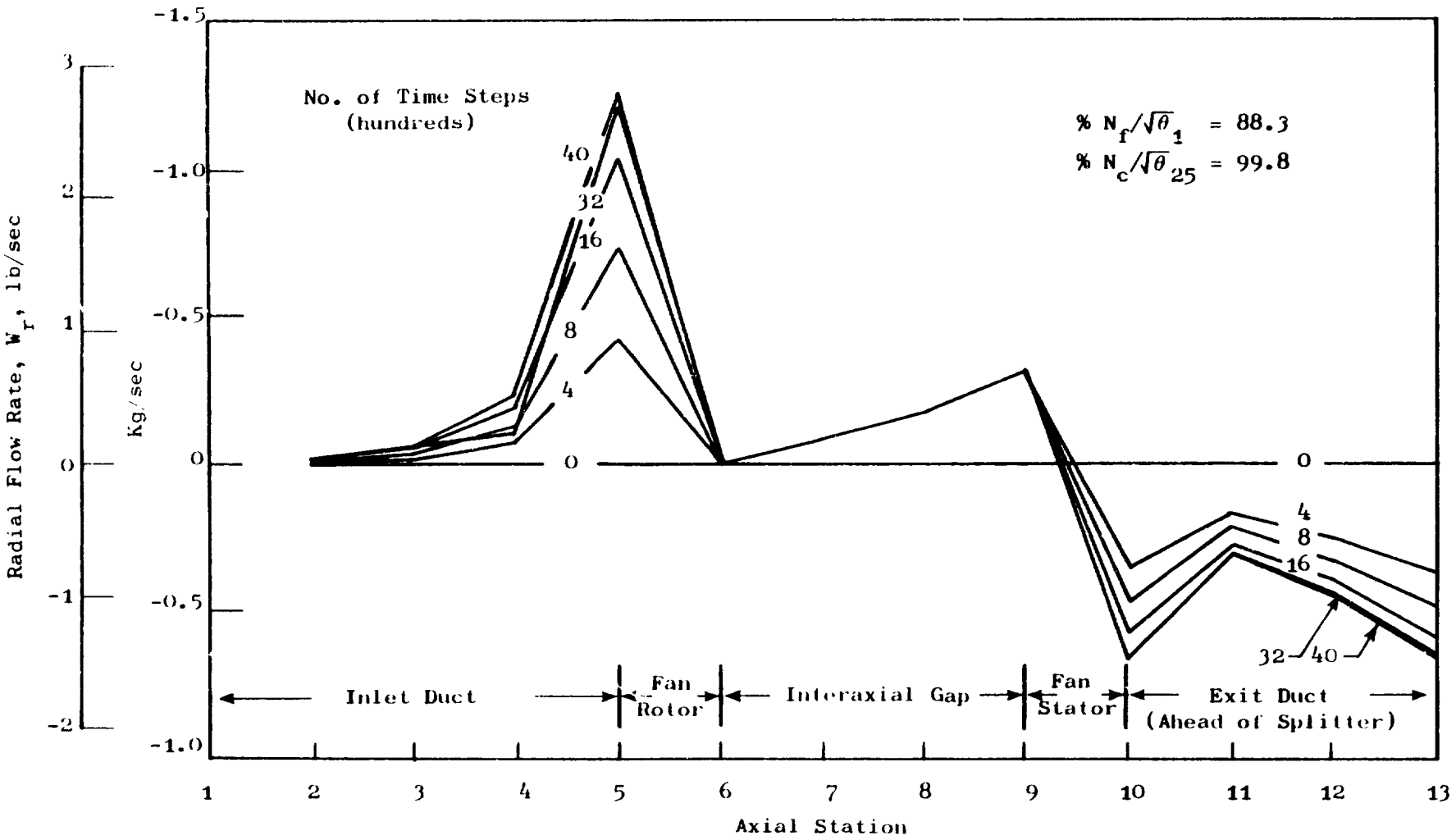

Figure 36. Distribution of Hub to Tip Radial Flow Rate.

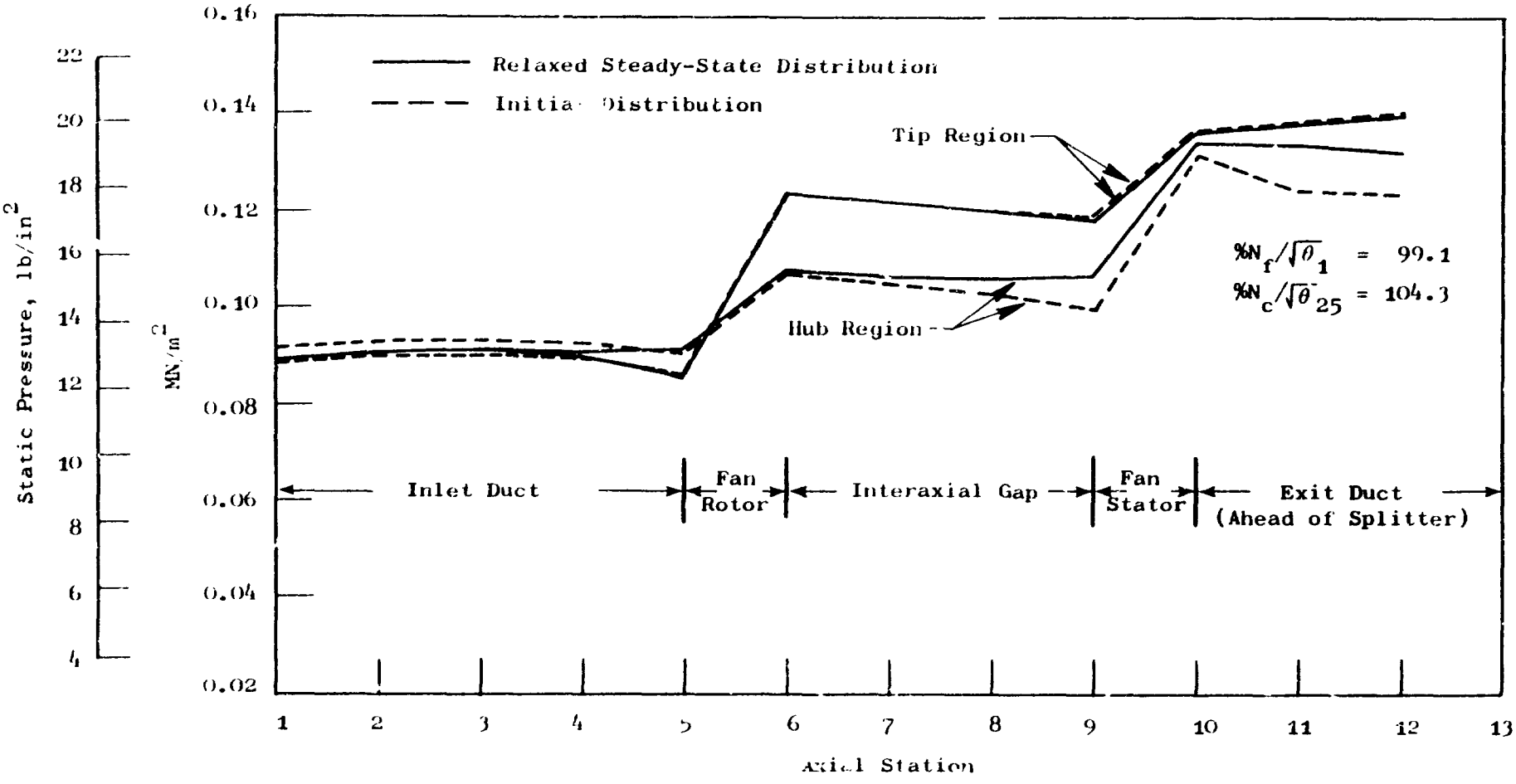

Figure 37. Average Static Pressure Distribution.

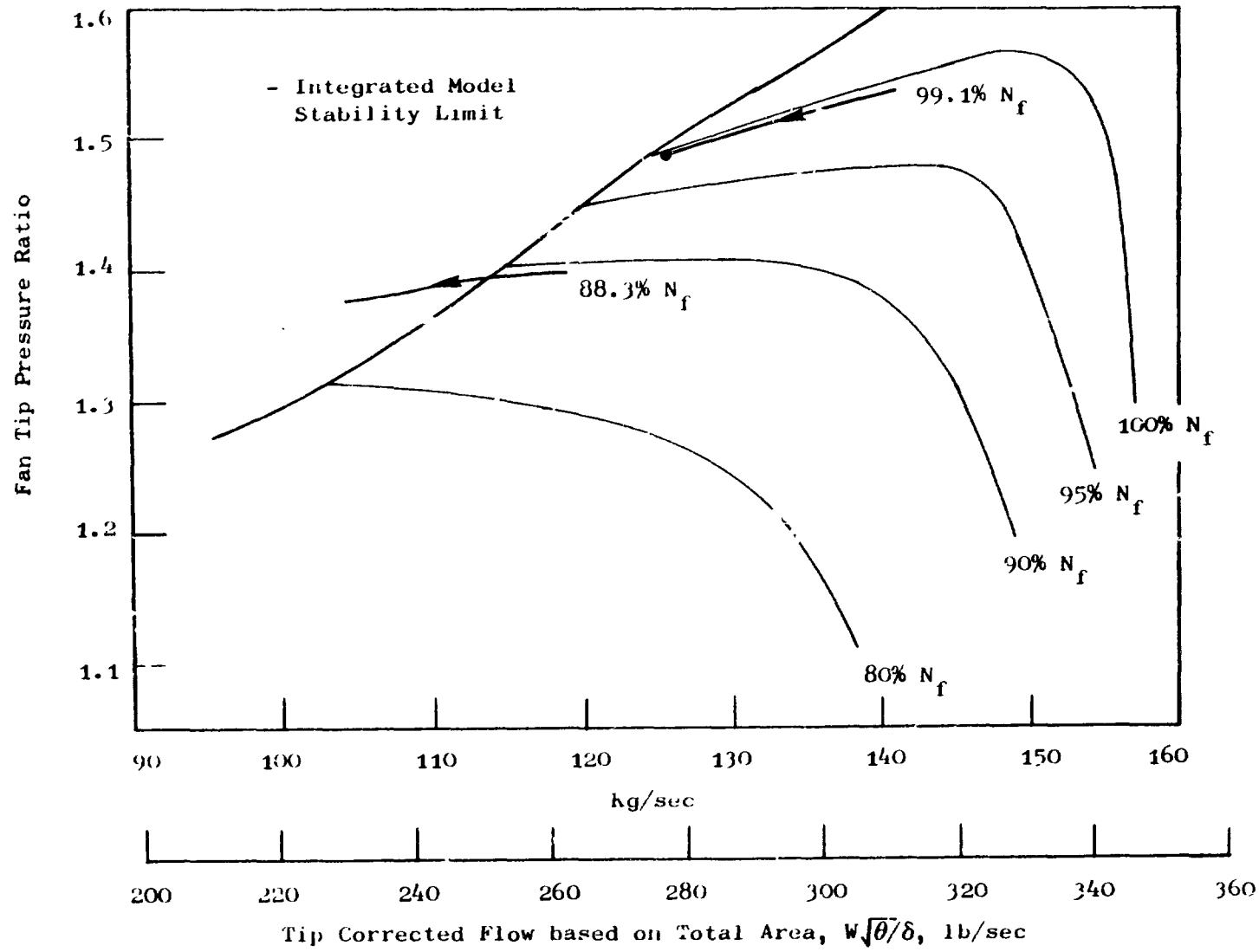

Figure 38. Fan Bypass Duct Throttling - Fan Tip Performance.

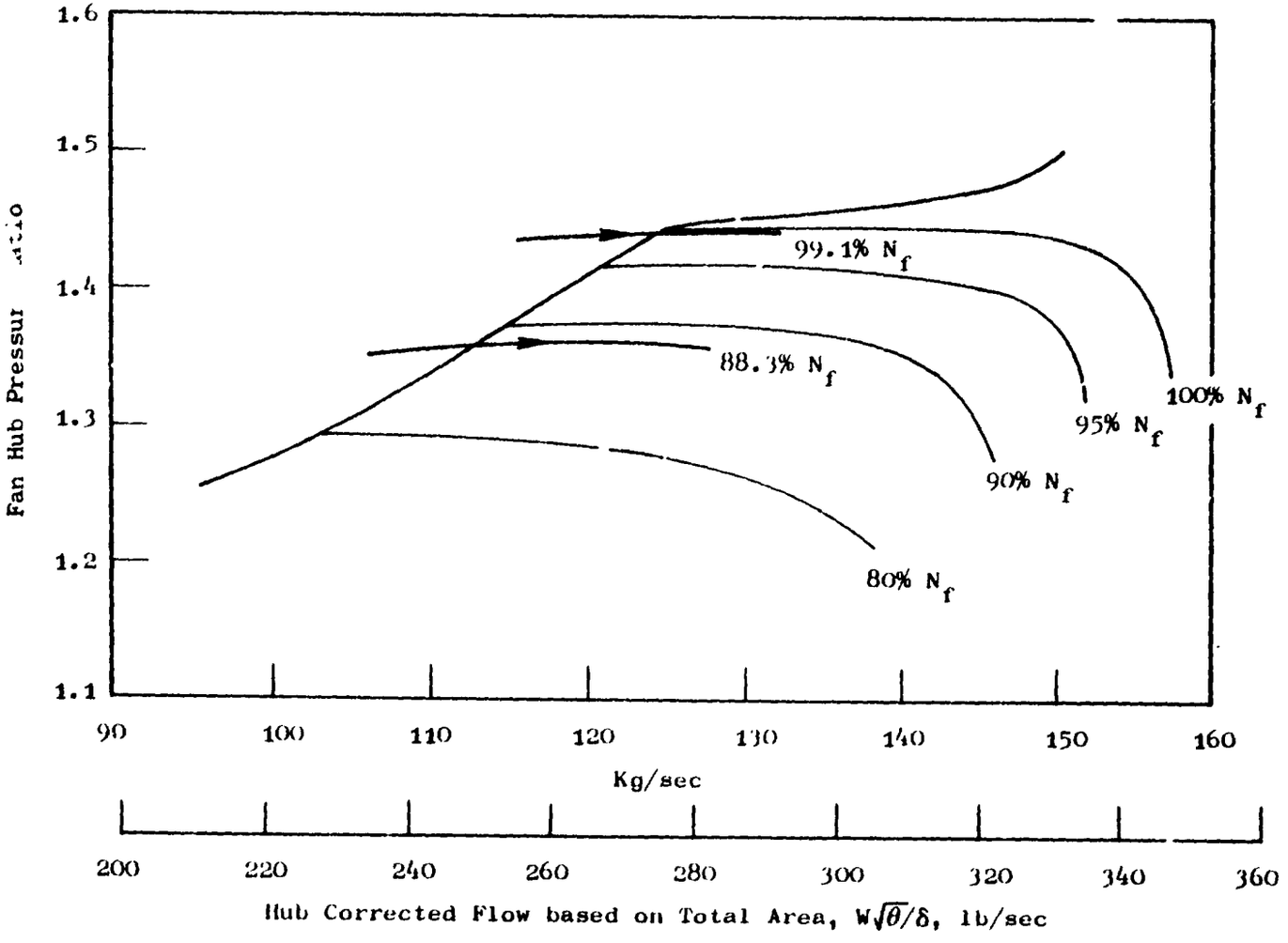

Figure 39. Fan Bypass Duct Throttling - Fan Hub Performance.

tip corrected flow rates are based on the duct total area and are calculated using the rotor hub and tip inlet flow rates, total temperatures and total pressures. Examination of these figures indicates that the fan tip corrected flow rate decreases during the throttling procedure while the fan hub corrected flow increases.

Further investigation was conducted to examine the effects of the bypass throttling on the distribution of flow variables. Figures 40 through 42 show the results plotted at different time steps for the 99.1% fan corrected speed case. Curves at time t = 0 give the steady-state distribution of flow variables. Curves at time t = 140 milliseconds give the distribution of the flow variables at the fan stability limit.

Examination of Figure 40 indicates that the axial flow rate in the tip region decreases with time for all the fan stations. The results shown in the same figure also indicate that at time t = 0 an increase in the axial flow rates occurs between stations 4 and 5. On the other hand, a decrease is observed between the same stations as the fan is throttled toward instability. This indicates that a spatial deceleration of flow occurs in front of the rotor tip as the model nears the instability region.

Figure 41 shows the distribution of the axial flow rate in the hub region. Since the flow rate at station 13 is the amount of flow entering the core, the results indicate that the core flow does not vary significantly during the bypass duct throttling. This is consistent with the constant pumping requirements of the core compressor. However, it should be observed that the flow entering the rotor, in the hub region, increases during the bypass duct throttling in order to satisfy the radial equilibrium in the regions ahead and behind the fan rotor.

The radial flow distribution during the bypass throttling is shown in Figure 42. It is noted that there is no significant adjustment in the radial flow at the interstage gap, between station 6 and 9. Furthermore, a major part of the radial redistribution takes place ahead of the fan rotor.

The flow bypass ratio, defined by the ratio of fan duct flow to core flow, was calculated at several points during the throttling procedure, for both 99.1% and 88.3% fan corrected speeds. Figures 43 and 44 show a comparison between these results with those obtained from the cycle deck data. A very good agreement is indicated and as a matter of fact, the average difference is less than 1%. This demonstrates the validity of the present model and its capability of handling compression systems with bypass ducts.

To investigate the model capability to predict the stability of the integrated compression system, a detailed throttling study was conducted along

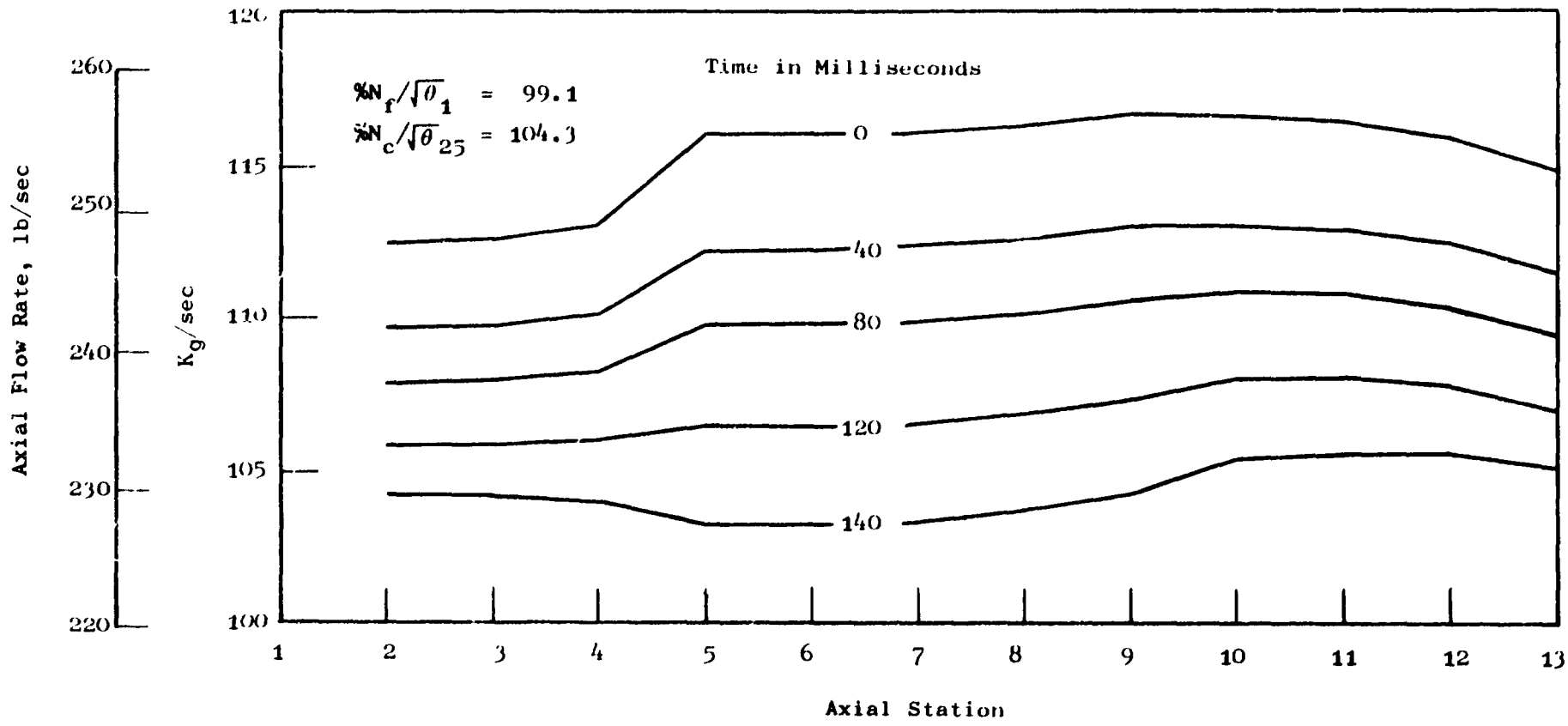

Figure 40. Effect of Bypass Duct Throttling on the Distribution of the Axial Flow along the Fan Tip Region.

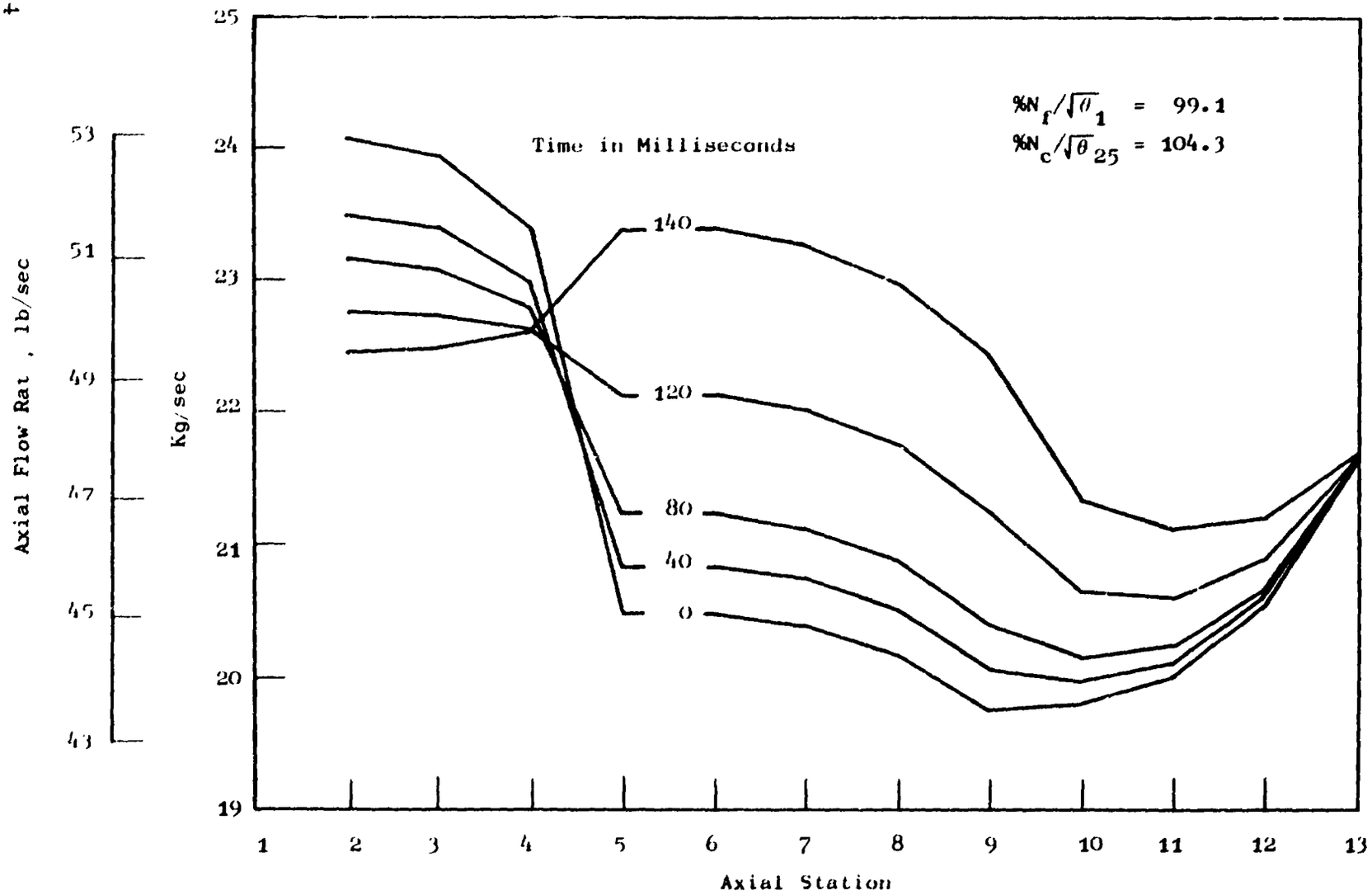

Figure 41. Effect of Bypass Duct Throttling on the Distribution of the Axial Flow along the Fan Hub Region.

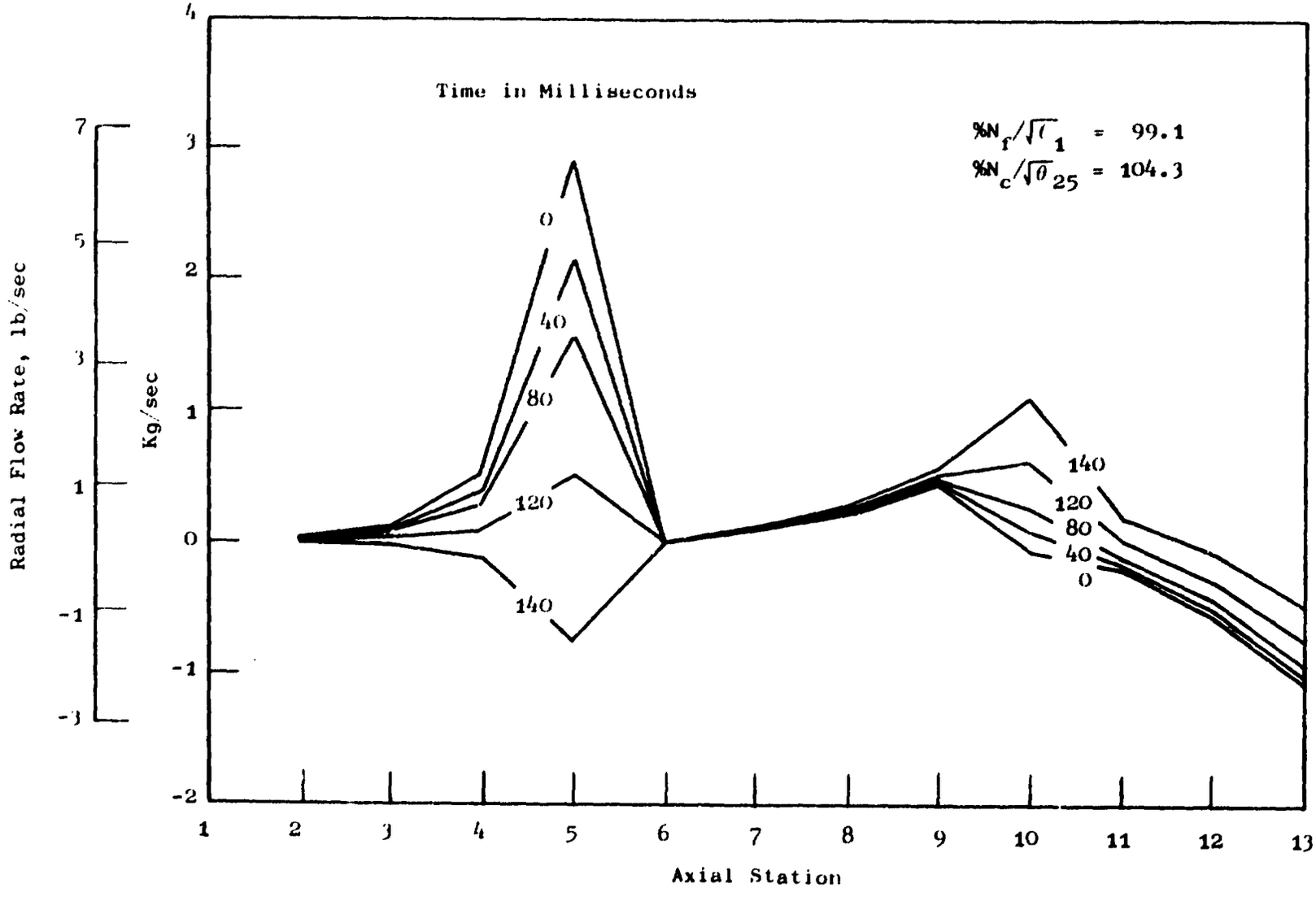

Figure 42. Effect of Bypass Duct Throttling on the Distribution of the Hub to Tip Radial Flow.

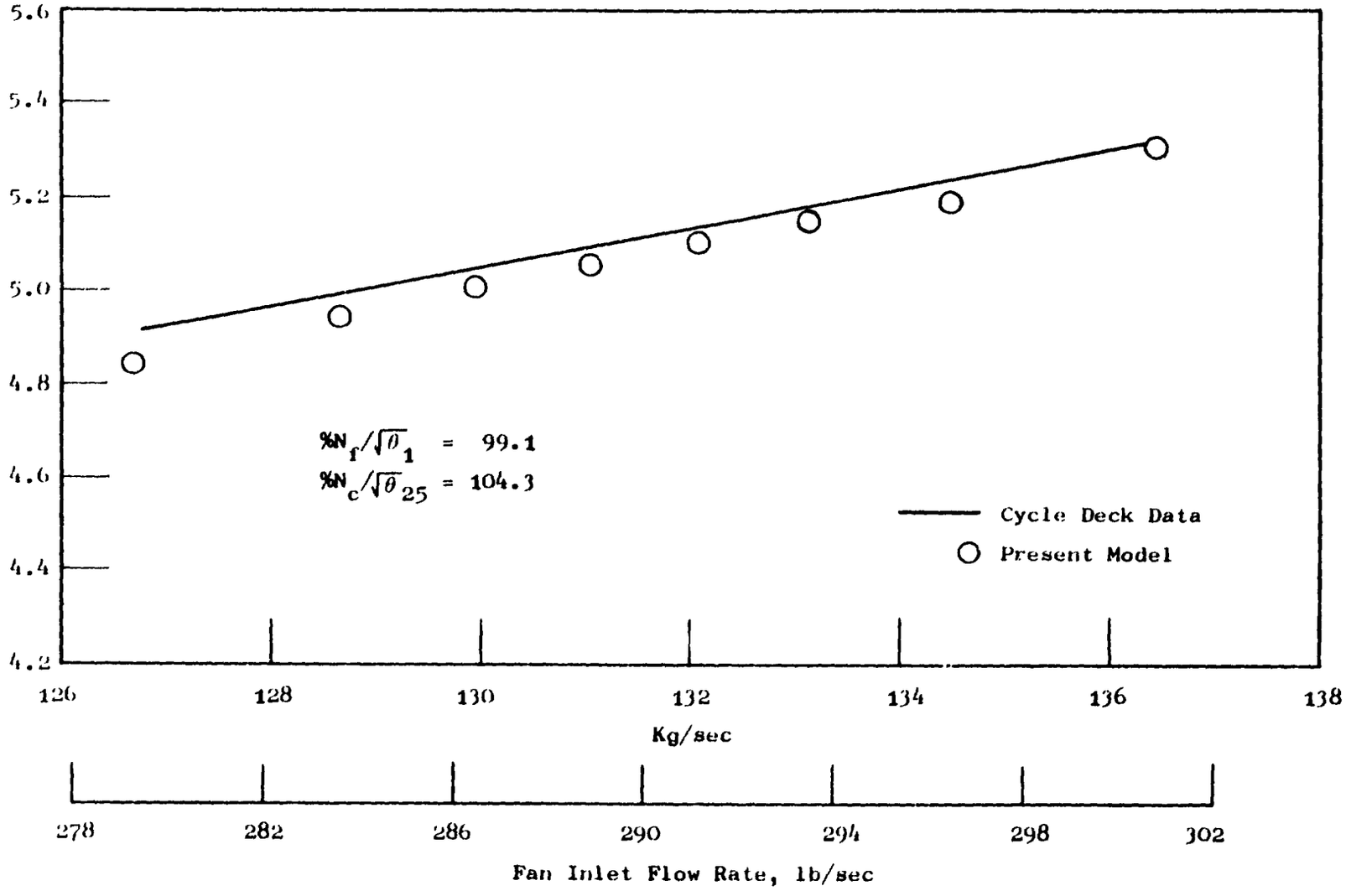

Figure 43. Variation of Bypass Flow Ratio during the Bypass Duct Throttling.

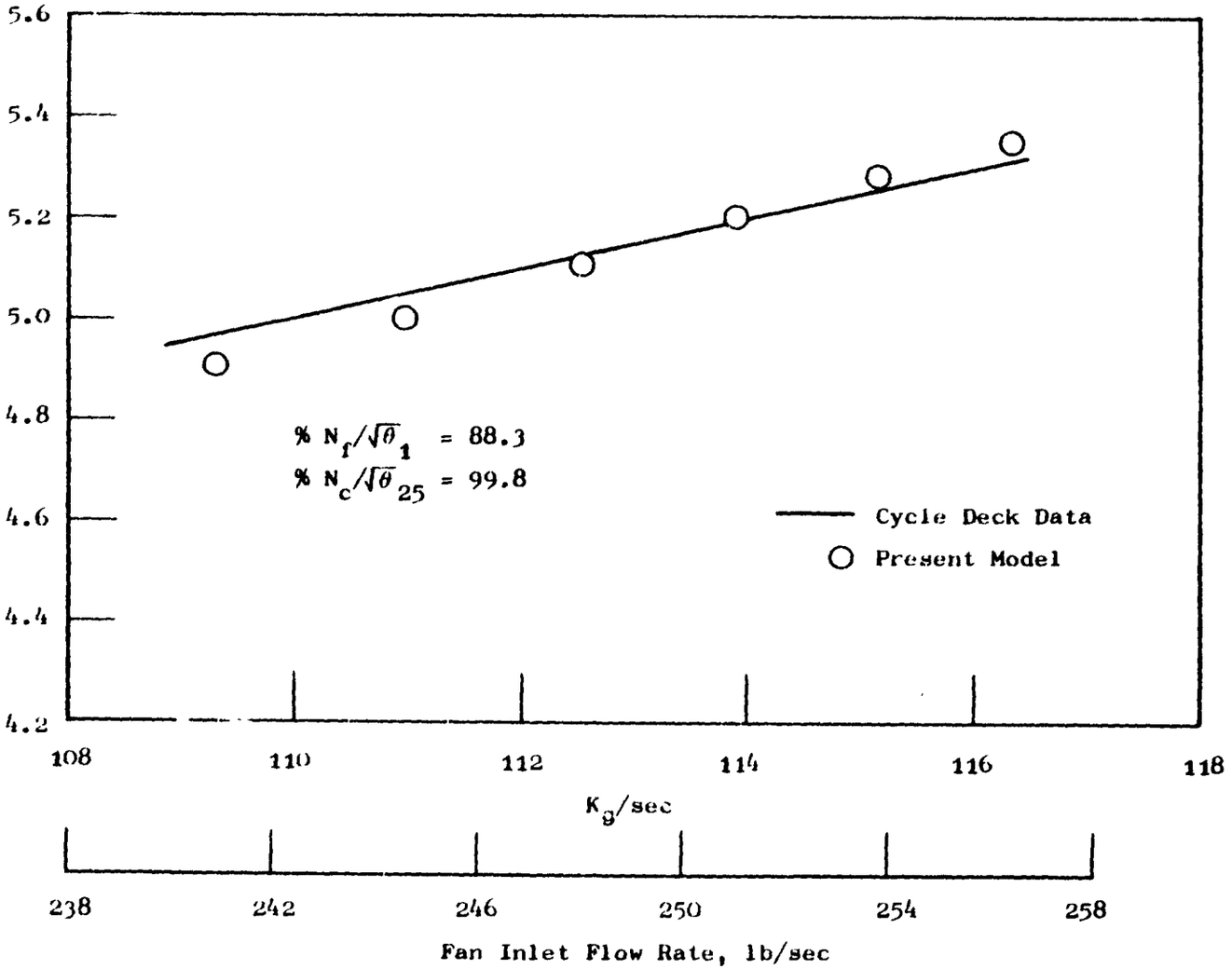

Figure 44. Variation of Bypass Flow Ratio during Bypass Duct Throttling.

the 99.1% fan speed line. The time variation of the fan tip and hub corrected mass flow rates are shown in Figures 45 and 46, respectively. It is noted that up to time t = 140 milliseconds, the change in the flow is gradual and well behaved (except for a few converging oscillations at the initial stages of throttling). However, further throttling beyond the experimentally determined stability line showed tendency toward rapid change in flow rates and finally solution failure.

In an effort to establish stability criteria similar to that of Reference 1, the fan tip amplification function (ratio of the rotor-volume-flow time derivative to the bypass duct exit-volume-flow time derivative) was investigated for irregular behavior during the throttling simulation. Figure 47 represents the time history response of the fan tip amplification factor. As the bypass duct is throttled, the parameter exhibits a rapid increase in the region of flow instability. Since the level of the exit flow derivative is constrained by the imposed exit boundary condition, the behavior of the flow derivative ratio indicates that internal perturbations in the fan rotor tip volume are amplified significantly as the model nears the stability limit. Once the derivative ratio had reached a level greater than 2 in the rotor volume, the solution was unstable and termination of the throttling process would not prevent the solution from failing. Therefore, this stability criteria was adopted for use in the model.

Figure 48 presents the ratio of the exit axial flow to inlet axial flow of the fan rotor tip and hub volumes at a fan corrected speed of 99.1%. As the fan is throttled toward instability, the data illustrates that the tip exhibits rapid mass storage and the hub exhibits rapid mass evacuation. This means that more fluid enters the rotor in the tip regions than leaves. Since flow instability is usually associated with flow blockage, this finding indicates that the flow instability is encountered in the tip region of the fan.

Bypass duct throttling at a fan corrected speed of 88.3% is illustrated in Figure 49. The well behaved corrected flow variation with time indicates that the flow for this speed line is stable. A detailed view of the throttling is shown in Figure 50. It is noted that the throttling has continued beyond the experimental stress limit and beyond the fan component stability limit obtained in Section 3.1 of this report. To further check the absence of instability, throttling was discontinued and the time calculations were continued further at the two points indicated by 16000 and 20000 time steps. No erratic behavior was indicated and actually the solution settled at the point where the throttling was terminated. These results indicate that even if the fan component is unstable by itself, it can be stable in the integrated system.

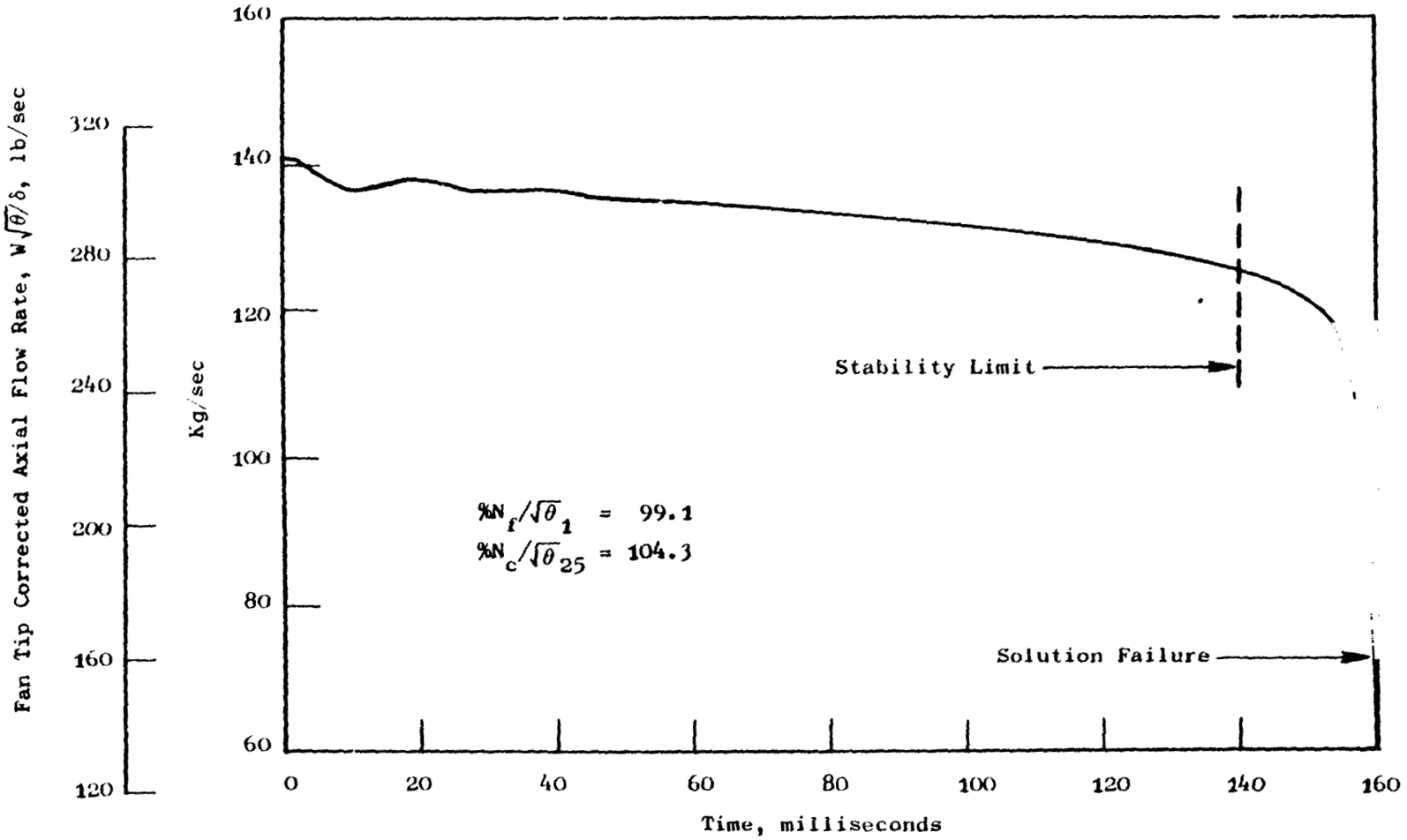

Figure 45. Variation of Fan Tip Corrected Mass Flow Rate during Bypass Duct Throttling.

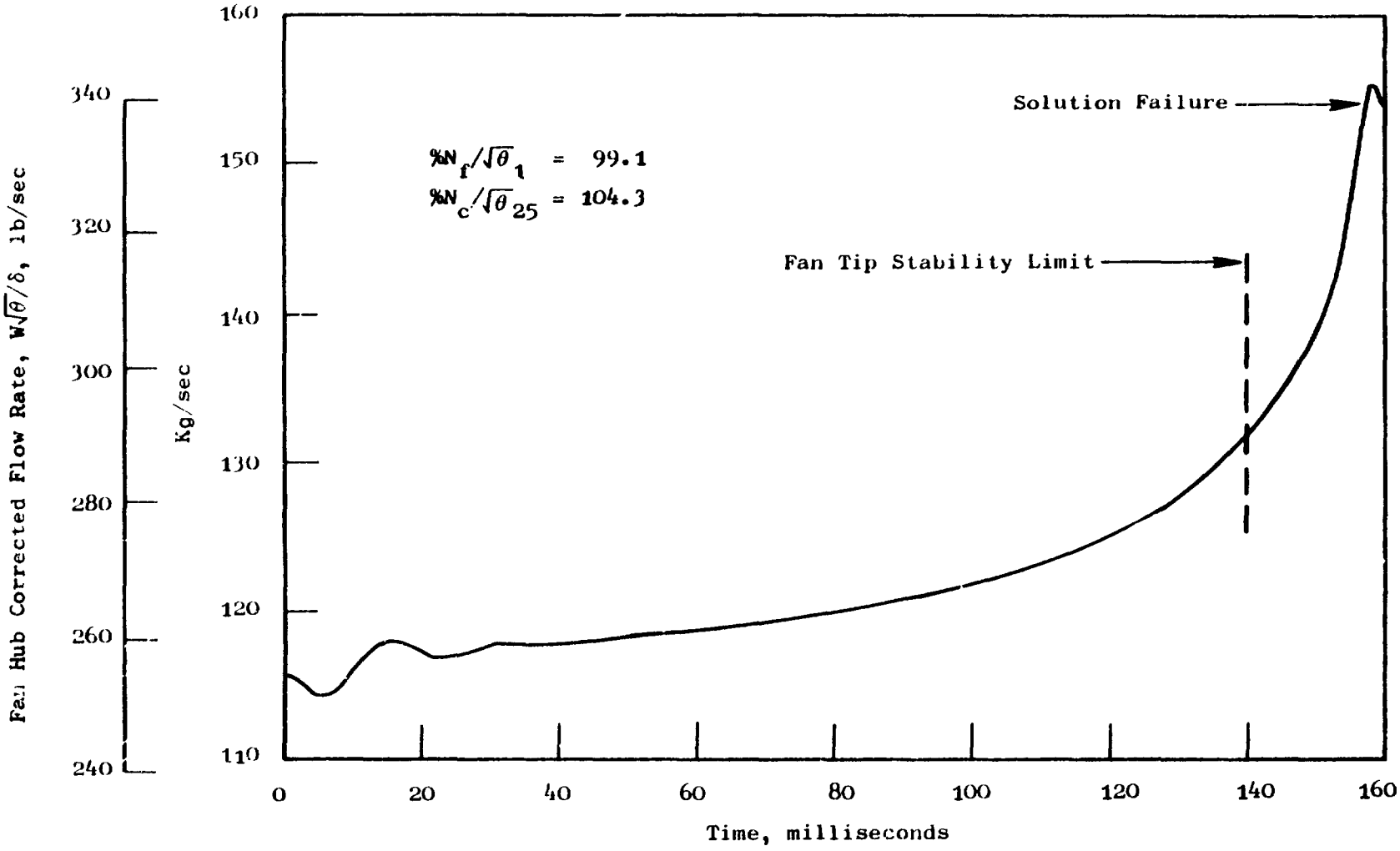

Figure 46. Variation of Fan Hub Corrected Mass Flow Rate during Bypass Duct Throttling.

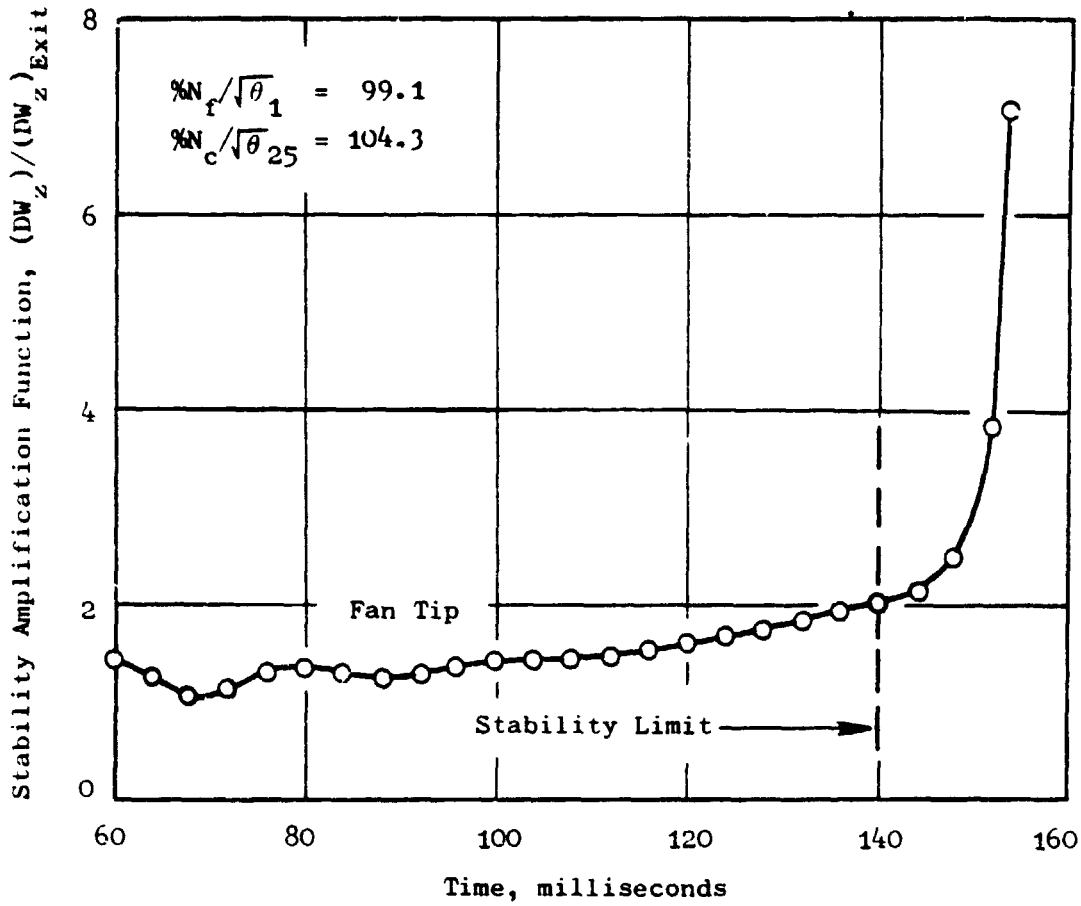

Figure 47. Stability Amplification Function Versus Time-Bypass Duct Throttling during Bypass Duct Throttling.

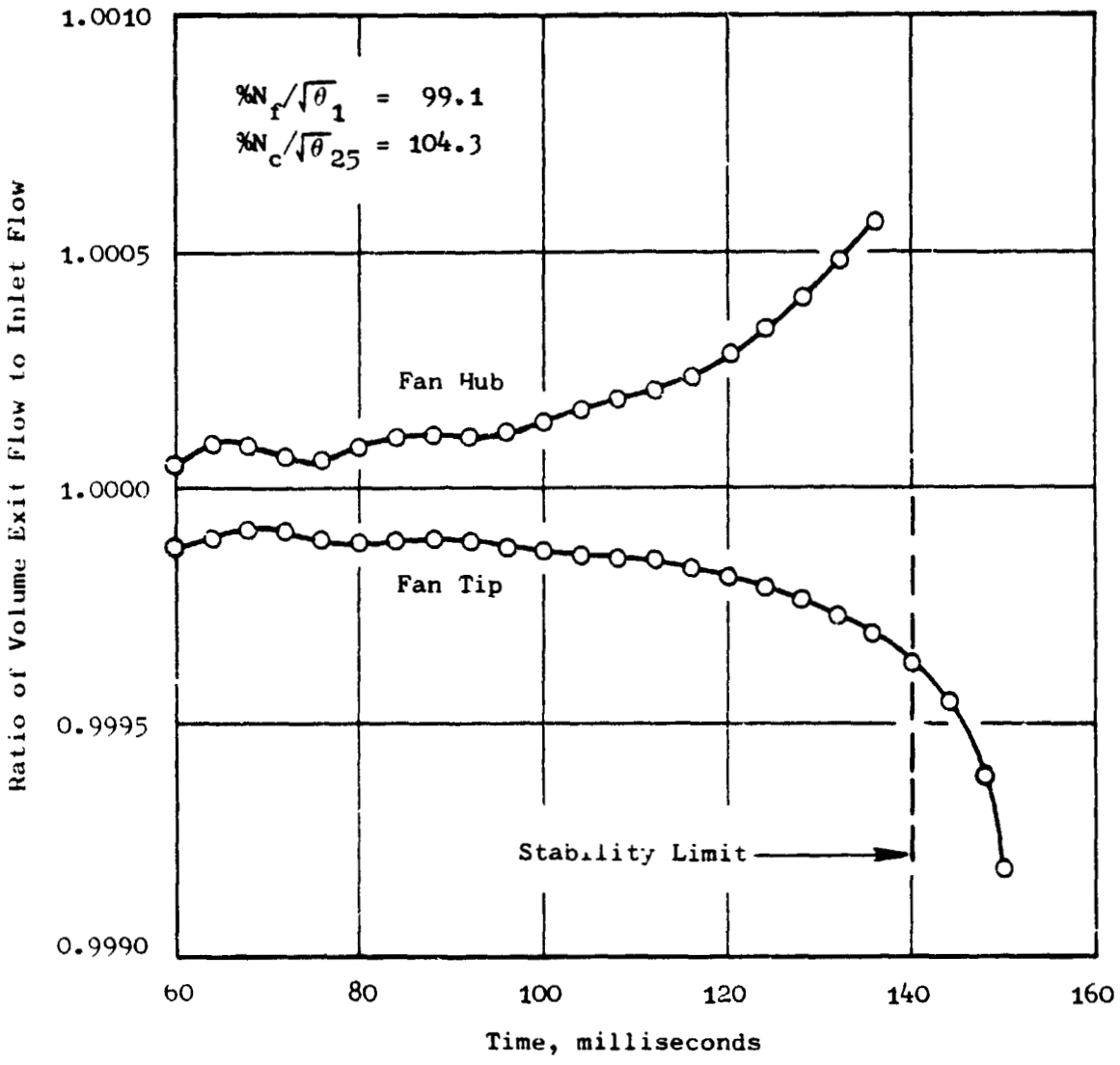

Figure 48. Ratio of Volume Exit Axial Flow to Inlet Axial Flow during Bypass Duct Throttling.

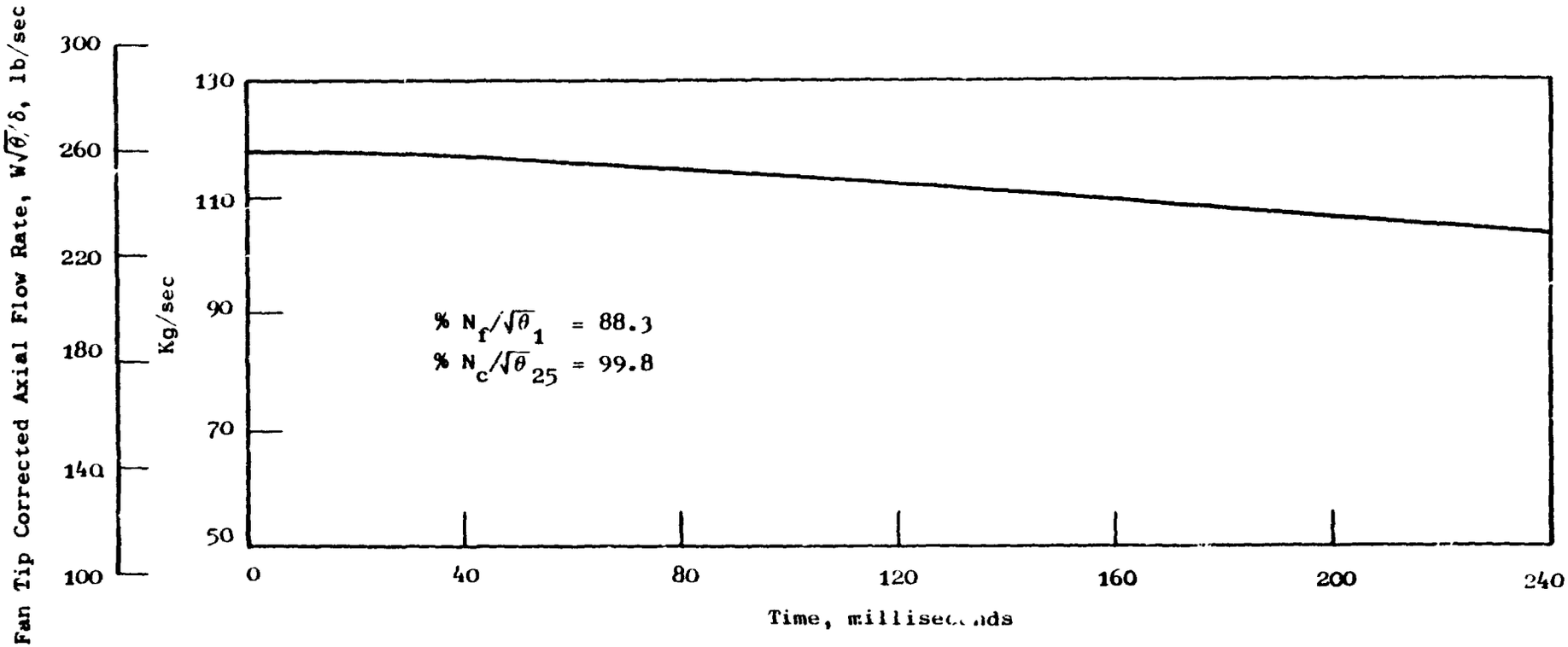

Figure 49. Variation of Fan Tip Corrected Mass Flow Rate during Bypass Duct Throttling.

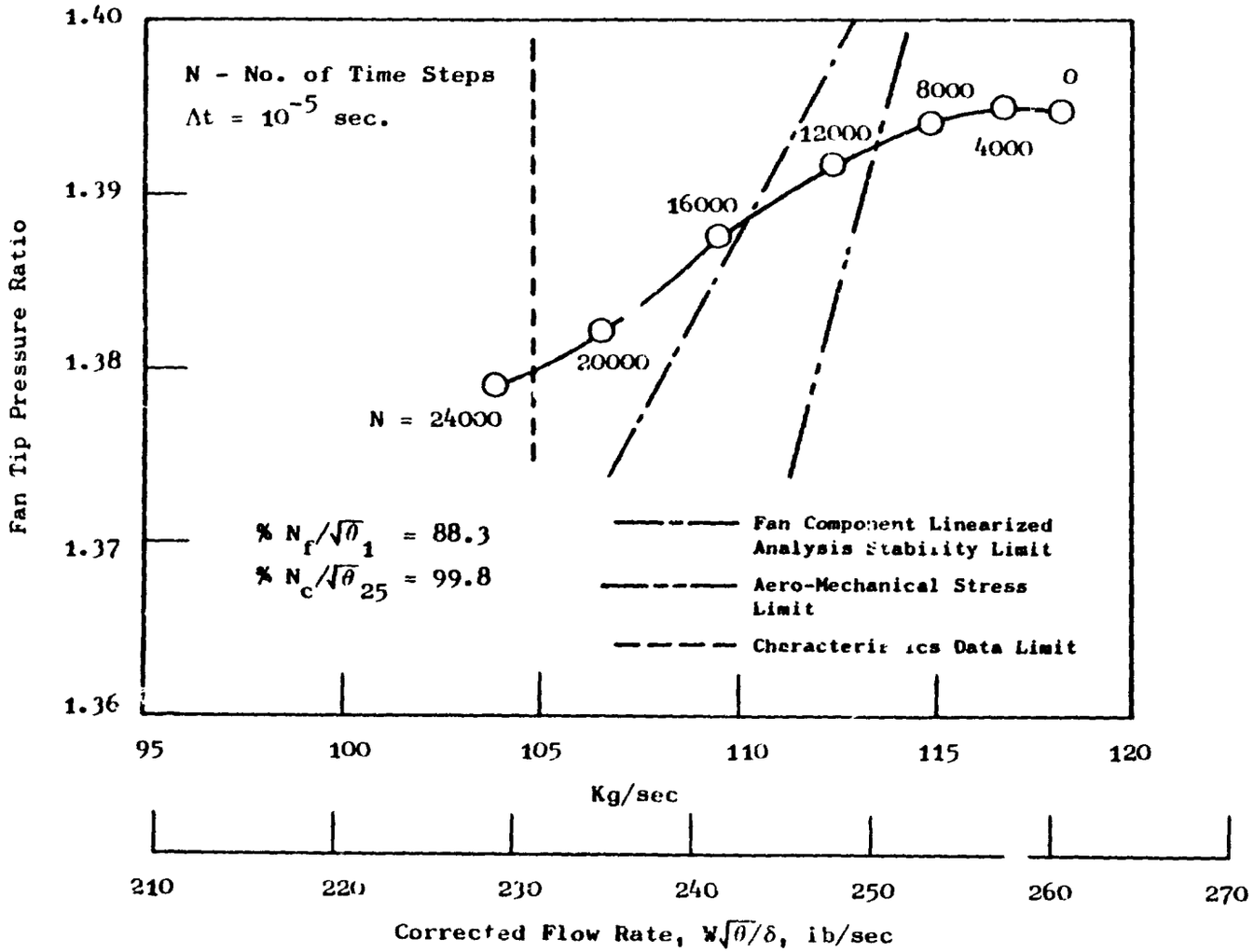

Figure 50. Details of Fan Tip 88.3% Speed Line (Bypass Duct Throttling)

4.4.3 Core Compressor Flow Throttling

Core throttling simulation of the TF34 integrated compression system was conducted for 104.3% and 99.8% core compressor corrected speeds. Figure 51 shows the throttling locii on the compressor performance map. The throttling line at the 99.8% corrected speed matches closely the compressor component demonstrated performance, while that at the 104.3% corrected speed deviates slightly from the demonstrated performance. In general, these results show a good agreement with the compressor component performance. However, it should be mentioned that in the present model, the specific heat ratio has been taken equal to 1.4 for all the cases. This condition attributed to the slight deviation observed at the 104.3%.

The compressor stability limit at 104.3% and 99.8% corrected speeds, as predicted by the present integrated system model, are shown by the solid circles in Figure 51. The results indicate a good agreement with those obtained by the compressor component model of Section 3.2 and shown by the open circles in Figure 51.

The change in fan performance during core throttling of a turbofan engine depends mainly on the level of the bypass ratio. For a high bypass ratio, the core flow rate is small in comparison to the total flow rate. In addition, throttling along a constant core speed line usually involves small variation in the core flow. Therefore, for the above two reasons it was expected that core throttling would not affect significantly the flow in the fan duct. Actually, in the present model of the TF34 high bypass ratio turbofan engine, it was observed that the adjustment of the flow occurs just ahead of the splitter. Moreover, it was also noticed that the decrease in the total flow rate due to the core throttling is averaged out at the front face of the rotor resulting in insignificant changes in the performance of the fan hub and tip regions. In other words, the core throttling of the TF34 integrated compression system does not change significantly the performance point of the fan.

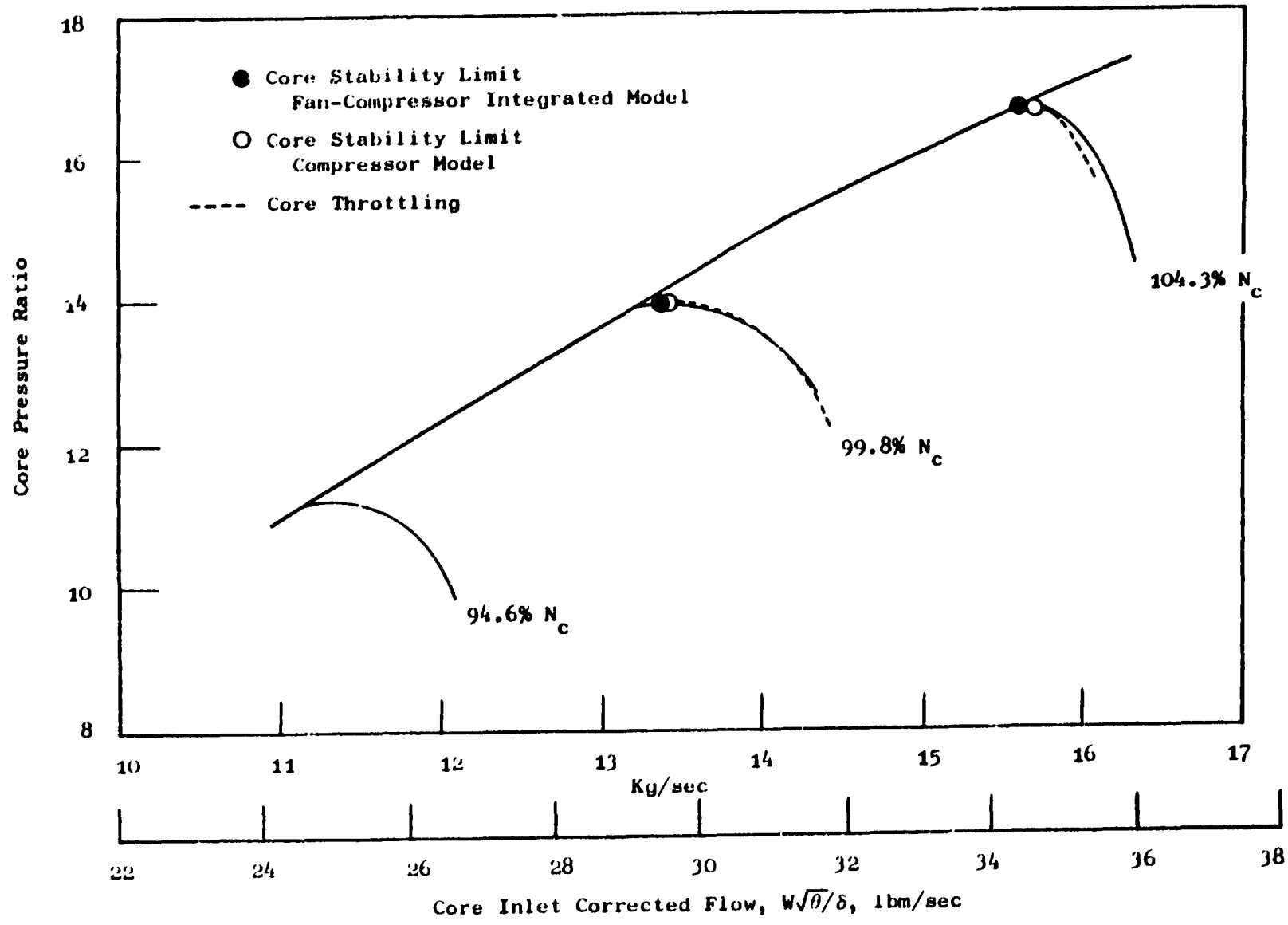

Figure 51. Core Throttling of the Integrated Compression System Model Core.

5.0 CONCLUSIONS AND RECOMMENDATIONS

The overall objective of the present effort was to conduct a computer study on the stability of the TF34 compression system. The study was performed in two steps. In the first step, the stability of the fan and the compressor components was examined using the linearized and the time-dependent one-dimensional stability techniques. In the second step, the stability of the fan-core integrated compression system was investigated using a two-dimensional stability technique developed to account for the radial equilibrium of the flow ahead of the bypass splitter.

During the component study effort, the fan tip, the fan hub, and the core compressor were individually modelled and the clean-inlet flow map of each was accurately reproduced. Fan corrected speeds of 80%, 90%, 95%, and 100%, and core compressor corrected speeds of 94.6%, 99.8%, and 104.3% were simulated. The stability limits of each component were predicted and the results matched the test data to an acceptable degree. Furthermore, these studies have indicated that the fan instability originated at the tip and that the core instability initiated in both the front and back stages. These findings agreed well with the experimental data and in the case of the core agreed with the fact that rotating stall occurred in the front stages at approximately the same time as surge initiated in the rear stages.

During the integrated system study effort, the dynamic model for the stability studies was developed. The model was based on solving the governing equations in time to describe flow unsteadiness in the compression system. The governing equations were first derived in a three-dimensional form and were then reduced to a two-dimensional form that included the radial equilibrium equation. Based upon the time-relaxed steady-state results and the throttling results, it was concluded that this time-dependent model correctly simulated the flow interaction between the core and the fan and showed the manner in which the flow adjusts radially ahead of the bypass splitter in order to account for the bypass ratio variation.

The time-relaxed steady-state solution was obtained for 99.1% and 88.3% fan corrected speeds with corresponding core speeds of 104.3% and 99.8%, respectively. Even though the fan was only divided into two regions - hub and tip - the flow distribution results indicated a reasonably good representation of the flow field. Further, the results indicated radial flow and radial pressure gradients behind as well as in front of the fan rotor. The radial pressure gradients showed strong dependency on the flow bypass ratio in addition to the dependency on the fan tip and the fan hub stage characteristics.

Fan and core throttling options were included in the integrated model for stability study purposes. With the use of both options, stability limits were predicted for fan corrected speed lines of 88.3% and 99.1%, and core corrected speed lines of 99.8% and 104.3%. Predicted stability limits in all cases, except at 88.3% fan corrected speed, compared well with those obtained by the component study and those observed during component testing. At a corrected fan speed of 88.3%, the fan duct throttling of the integrated system indicated that the flow through the fan was stable throughout whole speed line data range. This result indicates that the fan at certain conditions can be stable in a fan-compressor integrated compression system when it would be unstable as a component under the same conditions.

When the fan stability limit is reached, the flow instability was observed to occur in the fan tip region. Near the stall limit, a spatial deceleration of flow was noticed in front of the rotor tip. This flow deceleration subsequently caused the fan instability.

In addition to the stability studies, flow distributions in both the fan hub and the fan tip regions during the throttling process were examined. It was observed that fan bypass duct throttling affected both the fan hub and the fan tip flows. On the other hand, the core throttling showed very small effect on the flow distribution in the fan. This is attributed to the fact that the TF34 engine is a high bypass turbofan engine, and the changes in the core flow at constant core speed will not have significant effect on the fan total flow rate.

It was also observed that the radial flow in the fan interstage gap was not affected during the fan throttling. This was expected since the fan rotor/stator gap is small and most of the flow adjustments take place either ahead the rotor or downstream of the stator and in front of the bypass splitter.

A comparison was made between the model bypass ratio obtained during the model throttling process and the results obtained from the steady-state cycle deck. The comparison indicated close agreement for both fan corrected speed cases that were investigated.

Based upon the aforementioned results, it was concluded that the present integrated compression system model successfully simulated the flow interactions in the fan-core integrated compression system. Further, it is concluded that the present model offers a unique method for the studying the stability of a turbofan compression system.

The capability of the present model can be enhanced to increase further its value. The results of the analysis discussed in the previous paragraphs

indicate that it is possible to calculate some of the characteristics of the flow radial redistribution ahead of the bypass splitter by dividing the fan flow into only hub and tip regions. However, if one is interested in more details of the flow field, it is recommended that the flow field be divided into multiple radial sections in the region of the fan. Also, the capability of this model can be extended to handle three-dimensional flows by combining it with the circumferential redistribution of Reference 2. These modifications and extensions allow the model to simulate more complex geometry engines, such as the variable cycle engine with inner and outer bypass duct, and to handle flows with general inlet distortions.

APPENDIX A

RADIAL EQUILIBRIUM EQUATION

Upon writing the radial momentum balance based on Equation 5 for the elemental control volume shown in Figure 17C, one obtains:

$$\frac{1}{g_o}\frac{\partial}{\partial t}\int(\rho C_r dV) = \frac{1}{g_o}\left(\delta W_r^k C_r^k - \delta W_r^{k+1} C_r^{k+1}\right) + \left(\delta W_z^i C_r^i - \delta W_z^{i+1} C_r^{i+1}\right) + \left(W_{\theta_1} C_{r_1} - W_{\theta_2} C_{r_2}\right) + \left(W_{\theta_1} C_{u_1}\frac{\Delta\theta}{2} + W_{\theta_2} C_{u_2}\frac{\Delta\theta}{2}\right) + \Sigma\,\delta F_r \qquad (A1)$$

The radial momentum inside this elemental control volume can be written as

$$\int \rho C_r dV = \overline{\rho C_r}\,\delta V = \overline{\rho C_r(\delta A_r)}\;L_r$$

$$\text{i.e.}\int \rho C_r dV = \delta \bar{W}_r L_r \qquad (A2)$$

where the bar indicates averaged quantity and L_r is the control volume characteristic length in the radial direction.

The fourth term enclosed in brackets on the right hand side can be expressed in the following form:

$$W_{\theta_1} C_{u_1}\frac{\Delta\theta}{2} + W_{\theta_2} C_{u_2}\frac{\Delta\theta}{2} = \overline{W}_\theta\,\overline{C}_u\,\Delta\theta \qquad (A3)$$

where $\overline{W}_\theta$ and $\overline{C}_u$ are the averaged value of the circumferential flow rate and velocity. It should be noted that this term represents the centrifugal force acting on the control volume.

If we neglect all radial forces other than pressure forces, then $\Sigma \delta F_r$ can be written using Figure 17a as:

$$\Sigma \delta F_r = (L_z r^k \Delta\theta P^k - L_z r^{k+1} \Delta\theta P^{k+1})$$

$$+ (L_r L_z P_1 \frac{\Delta\theta}{2} + L_r L_z P_2 \frac{\Delta\theta}{2})$$

$$= (r^k P^k - r^{k+1} P^{k+1}) L_z \Delta\theta$$

$$+ \frac{1}{2} (P_1 + P_2) L_r L_z \Delta\theta$$

If we write the average pressure as

$$\frac{1}{2} (P_1 + P_2) = \frac{1}{2} (P^k + P^{k+1})$$

and

$$L_r = r^{k+1} - r^k$$

then the pressure force can be written as

$$\Sigma \delta F_r = \frac{1}{2} (P^k - P^{k+1}) (r^{k+1} + r^k) L_z \Delta\theta \qquad (A4)$$

Upon substitution of Equations A2, A3, A4 into A1, the following equation can be obtained for the elemental volume of Figure 17.

$$\frac{\partial (\delta \bar{W}_r)}{\partial t} = \frac{1}{L_r} \Big[(\delta W_r^k C_r^k - \delta W_r^{k+1} C_r^{k+1})$$

$$+ (\delta W_z^i C_r^i - \delta W_z^{i+1} C_r^{i+1})$$

$$+ (W_{\theta_1} C_{r_1} - W_{\theta_2} C_{r_2}) + (\bar{W}_\theta \bar{C}_u \Delta\theta)$$

$$+ \frac{g_o}{2} (P^k - P^{k+1}) (r^{k+1} + r^k) L_z \Delta\theta \Big] \qquad (A5)$$

Similar equations can be written for all the elemental control volumes of the control volume bounded by the planes j and j+1, and shown in Figure 17a. Upon summation of all these equations, the following equation is obtained.

$$\frac{\partial \bar{W}_r}{\partial t} = \frac{1}{L_r} \left[(W_r^k C_r^k - W_r^{k+1} C_r^{k+1}) \right.$$

$$+ (W_z^i C_r^i - W_z^{i+1} C_r^{i+1})$$

$$+ (W_\theta^j C_r^j - W_\theta^{j+1} C_r^{j+1})$$

$$+ \Theta \bar{W}_\theta \bar{C}_u$$

$$\left. + \frac{g_o}{2} (P^k - P^{k+1}) (r^{k+1} + r^k) L_z \Theta \right] \qquad \text{(A6)}$$

where Θ is the angular extent of the control volume.

REFERENCES

1. Tesch, W. A., and Steenken, W. G., "Blade Row Dynamic Digital Compressor Program, Vol. I, J85 Clean Inlet Flow and Parallel Compressor Models." National Aeronautics and Space Administration Contractor Report NASA, CR-134978, 1976.

2. Tesch, W. A., and Steenken, W. G., "Blade Row Dynamic Digital Compressor Program, Vol. II, J85 Circumferential Distortion Redistribution Model, Effect of Stator Characteristics, and Stage Characteristics Sensitivity Study," National Aeronautics and Space Administration Contractor Report NASA CR-134953, 1978.

3. Tesch, W. A., Mozzee, R. H., and Steenken, W. G., "Linearized Blade Row Compression Component Model, Stability and Frequency Response Analysis of a J85-13 Compressor," National Aeronautics and Space Administration Contractor Report NASA CR-135162, 1976.

4. Reynolds, G. G., and Steenken, W. G., "Dynamic Digital Blade Row Compression Component Stability Model, Model Validation and Analysis of Planar Pressure Pulse Generator and Two-Stage Fan Test Data," Air Force Aero Propulsion Laboratory Report AFAPL-TR-76-76, 1976.